Regulation and patterning of cell differentiation and pluripotency

Yue Zhang

Submitted in partial fulfillment of the

Requirements for the degree

of Doctor of Philosophy

in the Graduate School of Arts and Sciences

COLUMBIA UNIVERSITY

2011

ABSTRACT

Regulation and patterning of cell differentiation and pluripotency

Yue Zhang

The development of a multicellular organism from an embryo is one of the nature's most remarkable phenomena. Deciphering how this transformation occurs is a fundamental challenge in biology with profound biomedical implications. Insights into the molecular signals guiding developmental patterning may provide design strategies to promote multicellular structure formation in applications such as tissue engineering and regenerative medicine. In this thesis, we explored the applications of controllable gene expression techniques in combination with engineering strategies in regulation and patterning of cell differentiation and pluripotency, by pursuing three related research projects:

1. Reversible immortalization of cardiomyocytes to enable their proliferation necessary for obtaining large cell numbers
2. Patterning of the delivery of Doxycycline (Dox), the expression modulator of inducible BMP-2 expression vector, to mesenchymal stem cells cultured in a microfluidic device

3. Patterning of the Nanog gene expression in embryonic stem cells, using a microfluidic device, to establish differentiation – pluripotency boundaries that mimic the developmental processes *in vivo*.

In the first project, we developed a novel strategy for controlled expansion of non-proliferating primary neonatal rat cardiomyocytes by lentivector-mediated cell immortalization, and then the reversal of the phenotype of expanded cells back to the cardiomyocytes state. Primary rat cardiomyocytes were transduced with simian virus 40 large T antigen (TAg), or with Bmi-1 followed by the human telomerase reverse transcriptase (hTERT) gene; the cells were expanded; and the transduced genes were removed by adenoviral vector expressing Cre recombinase. The TAg gene was more efficient in cell transduction than the Bmi-1/hTERT gene, based on the rate of cell proliferation. Immortalized cells exhibited the morphological features of dedifferentiation (increased vimentin expression, and reduced expression of troponin I and Nkx2.5) along with the continued expression of cardiac markers (α-actin, connexin-43, and calcium transients). After the immortalization was reversed, cells returned to their differentiated state, as evidenced by molecular and functional properties inherent to terminally differentiated cardiomyocytes. This strategy for controlled expansion of primary cardiomyocytes by reversible gene transfer could provide large amounts of a patient's own cardiomyocytes for cell therapy, and enable controlled *in vitro* study of cardiogenesis.

In the second project, we developed a novel patterning strategy by using inducible gene expression systems in conjunction with simple multi-laminar fluidic techniques, which can directly pattern the expression of particular gene at transcriptional level. Using osteogenic differentiation of human mesenchymal stem cells as a model, we describe a novel approach to spatially regulate the expression and secretion of bone morphogenetic protein (BMP-2) in a two-dimensional field of cultured cells, by flow patterning the modulators of inducible BMP-2 gene expression. We first demonstrated a control of gene expression, and control of osteogenic differentiation of the cell line with inducible expression of BMP-2. Then we designed laminar flow systems, with patterned delivery of Doxycycline (Dox), the expression modulator of inducible BMP-2 expression vector. The patterned concentration profiles were verified by computational simulation and dye separation experiments. Experiments conducted in the flow systems for a period of three weeks showed the Dox concentration dependent osteogenic differentiation, as evidenced by mineral deposition. This strategy combining inducible gene expression with laminar flow technologies provides an innovative way to engineer tissue interfaces.

In the third project, we further developed the patterning strategy for gene expression to form boundaries of different gene expression domains in cultures of mouse embryonic stem cells. Using Nanog safeguarded embryonic pluripotency as a model; we demonstrated controlled Nanog expression, which lead to controlled early differentiation under the exposure or withdrawal of varied

small molecules, as evidenced by alkaline phosphatase (AP) staining, immunofluorescent staining, and gene expression analysis. By patterning Nanog gene expression, as well as soluble factors in the laminar fluidic system, we successfully developed varied differentiation – pluripotency boundaries between Nanog expressing pluripotency zones and Nanog suppressed early differentiation zones from the same population of cells, which mimic the development process *in vivo*. Mechanistic insights can be gained on dissecting the signaling pathways that drive multicellular patterning during the natural processes of embryonic and adult development.

In summary, we demonstrated that controlled expansion of non-proliferating primary cells can achieved by reversible genetic manipulation, and that varied continuous, graded pluripotency – differentiation boundaries can established by patterning the expression of target genes via a simple laminar fluidic system. Taken together, these approaches provide innovative models to modulate cell function at the transcriptional level.

Additional cooperative research was conducted during my graduate training. The manuscript of this study “Micropatterned Mammalian Cells Exhibit Phenotype-Specific Left-Right Asymmetry” was submitted to *Proc Natl Acad Sci U S A.*, and it is currently under review. We attached this manuscript in appendix.

Table of Contents

List of Charts, Graphs, Illustrations

Acknowledgements

First, I like to thank my advisor Gordana Vunjak-Novakovic for supporting me throughout this work and for her constant advice and encouragement. She is such a great inspiration to any student who is interested in Biomedical Engineering research. I treasure my learning experience under her invaluable guidance. I also like to thank Professor Kam Leong, Professor Clark Hung, Professor Sam Sia and Professor Jeremy Mao for serving on my thesis committee. Particularly I thank Professor Leong for his guidance and academic advice back in Singapore, which helped to shape me into who I am today.

Thanks to Leo Q Wan, Supansa Yodmuang, Danny Freytes, Yi Duan, Keith Yeager, Wei Leong and everyone else in the lab, for their help and support in various projects, encouragements and encouragement during my graduate work.

Thanks to Dr. Edam Nuglozeh, Dr. Fatoma Touré, Professor Ann Marie Schmidt, Professor Stephen Goff, Dr. Susana T. Valente, and Dr. Ettaly K. Franke for their collaboration in my first Ph.D. project, “Reversible immortalization of cardiomyocytes”. Thanks to Professor Dan Gazit, Professor Zulma Gazit and Dr. Pelled Gardy for their great support in my second Ph.D. project, “Patterned osteogenesis”. Thanks to Dr. Ana Sevilla, and Professor Ihor Lemischka for their great input in my third project, “Patterning pluripotency”.

Thanks to all my friends who have made my life in Columbia University so enjoyable and memorable. Special thanks to Sherry Lim, Chunmei Qiu, Cathy

Yang, Yanan Du, Xueyu Pang, Zheyuan Chen for being such wonderful friends during my study.

Last but not less, I like to thank Mom, Dad, and my husband, Xiaoxin for their endless love, patience, support, and encouragements. Most of all, thank you for sharing this journey and believing in me.

Dedication

I dedicate my thesis to my husband Xiaoxin Xia.

Chapter 1 Introduction

1.1 Temporal and spatial regulation of gene expression and the related cell function during in vivo development

The transformation of a single pluripotent cell into a multi-cellular organism *in vivo* involves a multitude of interrelated and orchestrated intercellular and intracellular processes that guide tissue morphogenesis. The most critical phenomenon in tissue morphogenesis is the spatial-temporal organization of cell differentiation from which the proper tissue functions arise.

1.1.1 Controlled expression of morphogens

Over the past few decades, evidences accumulated to support the existence of morphogen gradients acting as graded positional cues to control cell fate specification in developing tissue (Gurdon and Bourillot 2001; Tabata and Takei, 2004). It is generally proposed that a signal produced from a defined localized source forms a concentration gradient as it spreads through surrounding tissue. The graded signal then acts directly on cells, in a concentration-dependent manner, to specify gene expression changes and cell fate selection. The first molecular demonstration of the gradients specifying distinct cell fates is transcription factor Bicoid in the *Drosophila* syncytium (Driever and Nüsslein-Volhard, 1988a, 1988b), shown to be distributed along a gradient expanding from the anterior pole to more than one-half of the embryo and to regulate the expression of downstream gap genes. Afterwards, other signaling proteins such

as Dpp, Wingless, Spitz, Hedgehog, Activin and Nodal have been described as morphogens in a wide variety of organisms (Martinez Arias, 2003; Tabata and Takei, 2004; Schier and Talbot, 2005; Affolter and Basler, 2007). *Drosophila* embryo was used as a development model, to determine how the distribution of morphogens through a tissue establishes and maintains a gradient of activity, and how the signal is perceived and interpreted in a graded manner by the receiving cells (Ashe and Briscoe, 2006) (**Figure 1.1**).

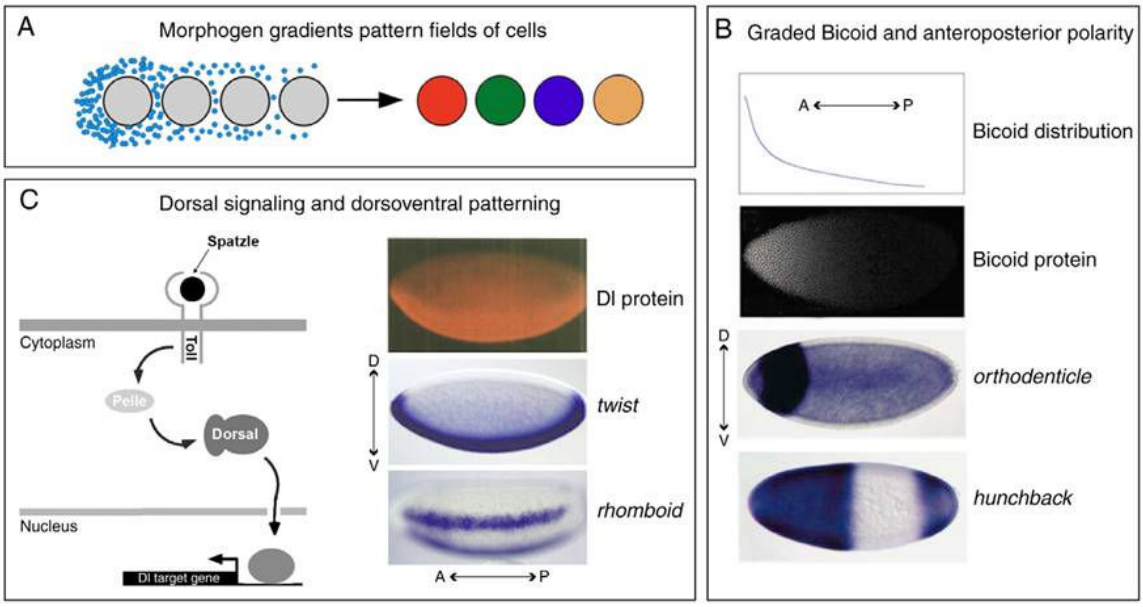

Figure 1.1 Patterns of morphogen gradients in developing tissues (A) A gradient of a signaling molecule (blue) within tissue (grey cells) provides positional information, instructing cells to adopt distinct cell fates (colored cells), according to the concentration of signal to which they are exposed. **(B)** The graded distribution of the transcription factor Bicoid establishes anteroposterior polarity in the developing *Drosophila* embryo. Immunostaining reveals the gradient of Bicoid distribution in the embryo. Expression of *orthodenticle* and *hunchback* genes is induced by high and low levels of Bicoid, respectively. **(C)** The dorsoventral (DV) axis of the early *Drosophila* embryo is patterned by graded Dorsal (Dl) activity (left). The ligand Spatzle binding to its transmembrane (TM) receptor Toll initiates signal transduction that, through the action of the kinase Pelle, activates the NF-B-like transcription factor Dl. (Right) Graded distribution of Dl protein; *twist* and *rhomboid* are induced by high and low levels of Dl, respectively. (Ashe and Briscoe, 2006)

The common controlled signaling pathways associated simple topobiological transformations (**Figure 1.2**) are briefly described here illustrating the controlled gene expression in vertebrate development process.

Stratification: Stratification is a process that enables the epithelium to form a multilayered barrier, protecting the organism from its environment, and allows functional diversification. During stratification, the daughter cells remaining in the basal layer can still proliferate, while the other daughter cells, become postmitotic, and start to pile up, forming multiple layers. Controlled activation of the p63 pathway in early epidermal lineage when cells are still forming a single layer (Green et al., 2003; Koster et al., 2004) is required in the stratification process (Koster and Roop, 2004).

Convergent extension: Convergent extension allows a change of shape of epithelial sheets by cell rearrangements. Lateral and medial cells become polarized and then the lateral cells intercalate between the medial cells, causing an extension along the anteroposterior axis (Keller, 2002). It is a fundamental topobiological transformation process involved in multiple organ formations, for example the formation of the avian primitive streak (Wei and Mikawa, 2000), and shaping of the avian neural plate (Schoenwolf, 1991; Schoenwolf and Alvarez, 1989), with the involvement of noncanonical Wnt signaling (Keller, 2002).

Invagination: Invagination of epithelial tissues is seen in the organization of the neuroepithelium in Xenopus (Schoenwolf and Alvarez, 1989). It also plays a

critical role in tooth formation (Jernvall and Thesleff, 2000). The activation of Wnt/β-catenin and the suppression of BMP by noggin lead to invagination of the epithelial placode to initiate hair follicle formation (Jamora et al., 2003).

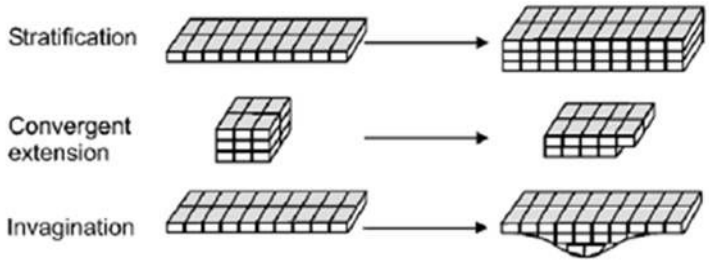

Figure 1.2 Topobiological transformation events during epithelial organ formation. These events are meaningful only at the level of cell groups (epithelial sheet, mesenchymal condensations), not at the single cell level.

1.1.2 Gene regulatory networks

Although the paradigm of morphogen patterning is widely accepted, recent developmental studies, in particularly of the relative sizes and positions of target gene domains and of the dynamic activation of morphogen target genes during development, added complexity into the model of morphogen activity.

Gene regulatory networks (GRNs) have been developed to study the spatial-temporal dynamics of controlled development process at the most fundamental level. The gene regulatory networks contain two complementary components. One component is the regulatory gene itself, such as a transcription factor or a signaling molecule. Transcription factors bind to specific sequences in the DNA and activate or repress the transcription of a gene or a group of genes. Signaling molecules carry out the communication between the cells and initiate the

activation of certain transcription factors in the cells that receive the signal. The complementary part of the regulatory apparatus is the regulatory genome. Every gene contains regulatory sequences that control when and where it is expressed.

Specification is the process by which cells acquire identities or fates that they and their progeny will adopt. To reach a given specification state the cells go through various regulatory states and one leads to the next. An initial set of transcription factors together with signaling cues from the neighboring cells activates a number of regulatory modules, which turn on/off the expression of regulatory genes that construct the next regulatory state of the cell until specification and differentiation are achieved. These inter-regulating genes form a regulatory network that is essentially the genomic program for development.

Here we use the gene regulatory network that governs endomesoderm specification in the sea urchin embryo to demonstrate the sophisticated spatial-temporal regulation of gene expression in development process. Early specification of endomesodermal territories in the sea urchin embryo depends on a moving torus of regulatory gene expression. This dynamic patterning function is encoded in a gene regulatory network (GRN) subcircuit (**Figure 1.3**) that includes the *otx, wnt8*, and *blimp1* genes and other components: *blimp1,* the early isoform of the *blimp1* gene (Livi and Davidson, 2006); nb-TCF, complex of nuclear β-catenin and TCF transcription factor; GSK3, enzyme responsible for β-catenin clearance, the activity of which is inhibited due to reception of the Wnt8

signal ligand. In the absence of nuclearized β-catenin, a Groucho/TCF complex forms instead (Range et al. 2005) and acts as a dominant repressor at both the *wnt8* and *blimp1* loci (dark blue barred stems). nb-TCF is inhibited from forming by GSK3, the biochemical mechanism of which is symbolized by the solid circle. Positive inputs from Blimp1 and nb-TCF control *wnt8* transcription (Minokawa et al. 2005), whereas both nb-TCF and Otx are required for *blimp1* expression; *blimp1* is subject to autorepression via two Blimp1 target sites.

Previous studies (Smith et al., 2007) revealed that expression of the *blimp1* gene begins in the micromeres around 6 hours after fertilization and appears in the adjacent tier of mesodermal cells by 12 hours. Soon after, expression disappears from the micromeres. By 18 hours, expression of *blimp1* begins in the adjacent presumptive endoderm lineage and disappears from the mesodermal cells. Autorepression of *blimp1* accounts for progressive extinction of expression in the center of the torus, whereas its outward expansion follows reception of the Wnt8 ligand by adjacent cells. Thereby, the gene regulatory networks control both the static spatial assignments in development and dynamic regulatory patterning.

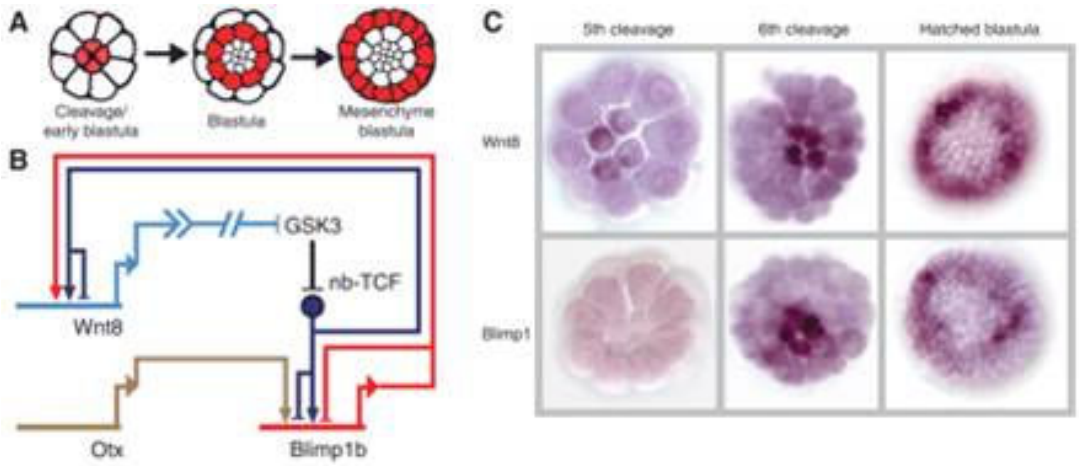

Figure 1.3 Moving-torus gene expression pattern (A) Expression pattern of *blimp1* or *wnt8* genes (red). The innermost cells are skeletogenic micromeres; the red ring in the second drawing shows mesoderm cells (prospective secondary mesenchyme); the outer ring is definitive endoderm. **(B)** GRN subcircuit including *otx, blimp1*, and *Wnt8* genes and other components. **(C)** Expression of *wnt8* and *blimp1*, visualized by Whole Mount In-Situ Hybridization (WMISH). By fifth cleavage, *wnt8* transcript is evident in the four micromeres at the vegetal pole. One cleavage later (sixth), *blimp1* transcripts are present in the micromeres. After this, *wnt8* and *blimp1* are expressed in the same territories.

1.1.3. Conclusion

In summary, the spatial and temporal regulation of genes expression drive the processes of cellular differentiation and morphogenesis, leading to the creation of different cell types in multicellular organisms where the different types of cells may possess different gene expression profiles though they all possess the same genome sequence. An important goal in cell and tissue engineering is to recapitulate this spatial and temporal pattern of genes expression, in order to engineer cells and tissue that reflect the function and structure derived from native development process. Integrative strategies are particularly needed to engineer spatial and dynamic distribution of genes / molecules along the tissue. These strategies can also provide platforms to study developmental process.

1.2 Biological strategies for regulating gene expression

As we discussed in the previous session, development of a multicellular organism requires the integration of multiple events occurring at specific times and locations during embryogenesis. Advances in methods for genetic engineering in mammals now enable researchers to explicitly examine the temporal and spatial role of genes expression during development *in vivo* and further engineer particular gene expression *in vitro*. Here we review two controlled gene expression systems: *reversible gene expression* and *inducible gene expression*, which have been used in engineering the dynamics of gene expression.

1.2.1 Reversible gene expression

Conventional genetic engineering uses viral vectors, such as retroviral or lentiviral vectors to introduce exogenous genes into cells. The genomic integration of viral vectors is of little concern for mechanistic studies of gene regulation, but their presence in the genome may result in cellular abnormalities in a potential therapeutic setting (Maherali and Hochedlinger 2008; Soldner et al., 2009). Although the use of transient factor delivery with vectors, which do not integrate into the genome, may overcome the problem, the systems suffer from very inefficient transduction. To this end, reversible gene expression strategies have been developed, which entails genomic integration of vectors, followed by their excision with highly specific enzymes (**Figure 1.4**).

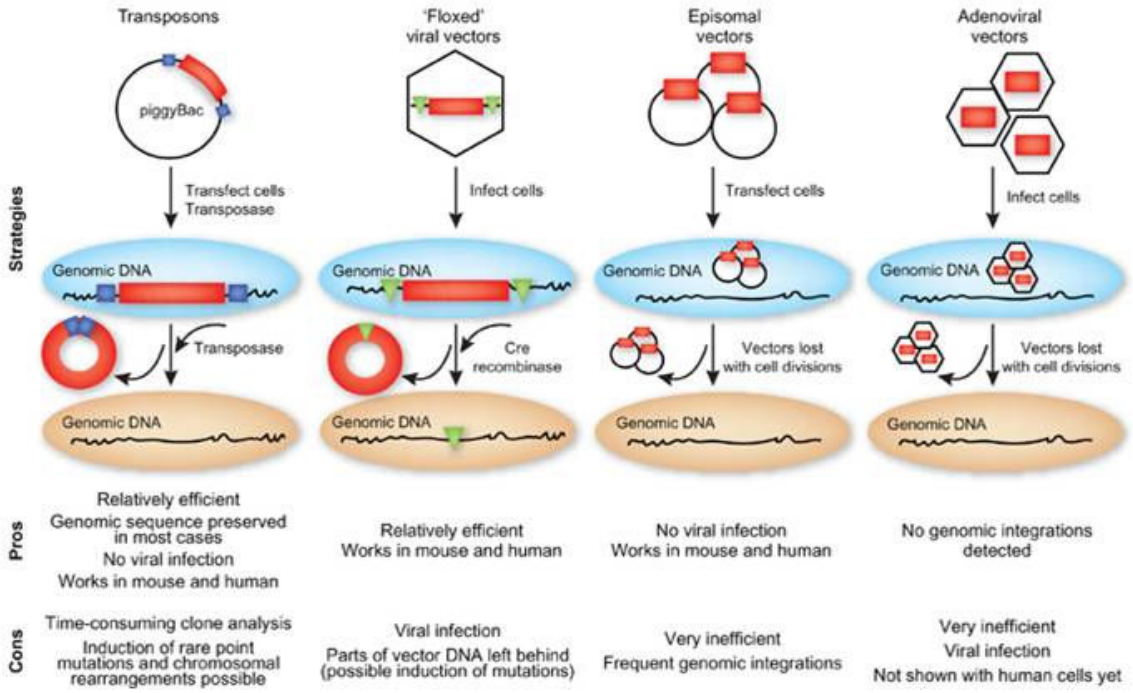

Figure 1.4 Reversible gene expression and transient gene expression systems Transposons and *loxP*-flanked vectors integrate into the host genome and can be excised using specific enzymes, whereas episomal vectors and adenoviruses are transiently introduced into cells and diluted by cell division. Red boxes, reprogramming factors; blue boxes: transposase recognition sites; green rectangles: *loxP* sites.

The classical expression-excision system uses site-specific recombinases derived from bacteriophages and yeast (Branda and Dymecki 2004; Joyner and Zervas 2006; Lewandoski 2001). The site-specific recombinases Cre and Flp bind to and recombine specific sequences of DNA termed *loxP* or *FRT* sites, respectively. By flanking essential exons with either *loxP* or *FRT* sites particular genes can be conditionally inactivated or activated, depending on the structure of the genes and exons targeted. In cells containing Cre or Flp and a gene with exons flanked by *loxP* or *FRT* sites, the gene will be permanently inactivated or activated in cells expressing Cre or Flp and their progeny. These techniques have been used as tools to conditionally inactivate or activate genes. The

temporal-spatial pattern of Cre or Flp expression could be determined by the gene into which Cre or Flp has been targeted. Particularly, the temporal control of Cre and Flp has been enabled by the development of ligand-regulated forms of Cre and Flp, such as tamoxifen-inducible $CreER^{T2}$ and tetracycline-responsive Cre lines (Feil et al., 1997; Indra et al., 1999) both systems allow the timing of Cre/Flp expression to be tightly regulated.

A potential limitation of this technique is that the Cre-mediated excision leaves *loxP* sites at random locations in the genome, which may disrupt the function and expression of endogenous genes. The novel approach has been developed based on the *piggyBac* transposon, a mobile genetic element from insects that efficiently integrates into the genome of mammalian cells (Wang et al., 2008). Notably, *piggyBac* transposons can be entirely removed when re-exposed to transposase, thereby, both integration and excision are catalyzed by the *piggyBac* transposase, which restores the correct genomic sequence in >90% of excision events (Wang et al., 2008). The major advantages of transposon mediated gene delivery are high reprogramming efficiency and evidently low incidence of genetic alterations. A potential limitation of *piggyBac*-mediated reprogramming is the possibility of 'transient' integration-excision events during the two rounds of transposase expression, which might lead to alterations in genomic sequences that cannot be easily detected (Geurts et al., 2006).

1.2.2 Inducible gene expression

The development of inducible gene expression system was largely inspired by Nature's regulatory mechanisms. Signaling proteins that mediate hormonal responses were first adopted as tools for transcriptional control, as it was found that the ligand-binding domains of the glucocorticoid, estrogen, and ecdysone receptors (GR, ER, and EcR) can be fused to heterologous proteins to modulate their function (Christopherson et al., 1992; Eilers et al., 1989; Green and Chambon, 1987). Coupling these ligand-binding domains to DNA-binding and transactivating polypeptides therefore enables the small-molecule-dependent transcription of genes driven by the corresponding response elements. Since their introduction during the late 1980s, chimeric hormone receptors have been widely used to regulate gene expression in cultured cells and embryos (Kolm and Sive, 1995; de Graaf et al., 1998, Esengil et al., 2007).

A simple method of transgene regulation was subsequently developed that equip the transgene with a known promoter sensitive to a small molecule drug, such that gene expression is controlled pharmacologically by administering a small molecule drug. The Tet system was the first one described, and has since became well established as a research tool. Bacterial resistance to this antibiotic involves the expression of a transmembrane efflux pump (TetA), which is regulated by a transcriptional repressor (TetR). In the absence of tetracycline, or its synthetic derivative doxycycline, TetR binds to operator sequences (*tetO*) in the *tetA* regulatory domain; the binding of tetracycline to TetR, however,

promotes its dissociation from *tetO*, enabling *tetA* transcription and antibiotic clearance from the bacteria.

Based on this system, Gossen and Bujard established two ligand-inducible gene transcription strategies that can be applied in mammals. In the “Tet-Off” system, the DNA- and ligand-binding domains of TetR are fused with the VP16 activation domain to form a constitutive transcriptional activator (tTA) that is inhibited by tetracycline (Gossen and Bujard, 1992). The “Tet-On” system utilizes a “reverse” form of tTA (rtTA) that actually requires tetracycline for *tetO* binding (Gossen et al., 1995). Using these complementary methods, transgene expression can be inhibited or activated in a ligand-dependent manner.

In summary, inducible gene expression strategies have provided an extra level of conditionality in engineering the spatial - temporal dynamics of genes expression.

1.2.3 Application: Regulation of cell proliferation and pluripotency

The developmental process from totipotent cells to specific tissues is controlled by dynamic mechanisms. Here we review the applications of genetic engineering strategies for cell reprogramming towards altering the patterns of gene expression and cell fate, with focus on engineering the cell proliferating capacity and pluripotency.

There has been considerable interest in developing strategies for optimizing culture conditions for cell survival and proliferation. Primary cells are of great interest for research and for drug discovery and regenerative therapy. However, the cell sources, and cell proliferation capacity are limited. One way to overcome this problem is cellular immortalization, which can be seen as a bypass of cellular senescence. The molecular mechanisms of cellular immortalization have been defined (Lundberg et al., 2000; Shay et al., 1991).

Two immortalization agents have been widely used: the Simian virus 40 large T-antigen (TAg) and the catalytic subunit of telomerase (human hTERT or mouse mTERT). TAg is a typical tool used for cellular immortalization (Forest et al., 1983). As a DNA tumor virus in the papovavirus family, TAg is expressed as a human cell-specific oncogene, thus serving to inactivate a p53 gene and Rb protein (Lane 1984). TAg can avoid senescence in the first stage (M1 phase) and facilitate immortalization, but does not maintain the telomere length, and it cannot be guaranteed that SV40T alone can immortalize cells completely. On the other hand, hTERT gene can activate telomerase within cells and maintain the telomere length. Therefore, by transducing a hTERT gene in combination of TAg, cells can overcome the M1 phase, and maintain immortalization (Bodnar et al., 1998; Okitsu et al., 2004; Zhu et al., 1999).

In addition, Cre/loxP site-specific recombination was applied to enable the reversibility of cell immortalization, creating reversibly immortalized human cell

lines that can remove the introduced immortalizing gene later by coding the genes between a pair of loxP sequences. Therefore, once cells are immortalized by introduction of loxP-flanked immortalizing genes, they grow unlimited in tissue culture. After the immortalized cells proliferate to sufficient numbers, by "cutting out" the immortalizing gene at that stage a large amount of reverted form of cells with original preimmortalized status can be obtained. So far, reversible immortalization had been successfully applied to primary fibroblasts (Westerman and Leboulch 1996), human muscle satellite cells (Cudré-Mauroux *et al.*, 2003), human insulin secreting beta cells (Narushima *et al.*, 2005), and other types of cells (Kobayashi *et al.*, 2001; Noguchi *et al.*, 2002; Kowolik *et al.*, 2004; Hashimoto *et al.*, 2006).

The development of pluripotent iPS cells represented a great application of genetic engineering in exploring new cell sources for tissue engineering and potentially regeneration therapy. In 2006, the Yamanaka group derived induced pluripotent stem cells (iPS) by the introduction of four transcription factors (Oct3/4, Sox2, Klf4, and c-Myc) into adult cells (Takahashi and Yamanaka, 2006; Takahashi et al., 2007), which may offer a source of autologous functional cells. One significant concern regarding the therapeutic value of iPS cells is the presence of proviral integrations harboring known oncogenes, particularly c-Myc, as well as Oct4 and Klf4. The effects of the randomly integrated retroviral vectors used for reprogramming represents a more fundamental defect in the developmental potency of iPS cells.

In certain ways, reversible immortalization shares similarities with studies of reprogrammed (iPS) cells (Takahashi and Yamanaka, 2006; Takahashi et al., 2007). Both strategies use lentivirus-based gene transduction to induce adult primary cells into dedifferentiated proliferating status, and apply growth factors to re-differentiate the expanded cells into specific lineages. Notably, when reversible immortalization is used, the expanded cells are depleted of the inserted genes via *loxP*–Cre recombination. As a result of complete gene splicing, cell proliferation was completely arrested, enabling the elimination of potential tumorigenic problems in transplantation practice.

The iPS research also suggested various strategies of gene transfer for deriving fully functional, mature cell phenotypes. The TAg gene interacts with cell cycling-related factors, such as p53 (Schultz *et al.*, 2000), which induces cell proliferation, but is also involved in the control of DNA repair and recombination. In iPS studies, differentiated cell phenotypes are derived through a series of steps starting with early cell differentiation. In studies of reversible immortalization, the process is being shortened by picking the most promising clones that express specific key phenotypes and by regaining the lost cell phenotypes by proper stimulation after gene splicing. This “shortcut” strategy worked well with many cell types, such as human insulin-secreting beta cells (Narushima *et al.*, 2005). If, however, the full phenotypic characteristics of certain cells, for example, cardiomyocytes are not restored, in particular, the contractile function (Zhang et al., 2009).

Recently, two groups used reversible gene expression system, piggyBac, to develop a new generation of iPS cells. The strategy which combined the merits of reversible immortalization and traditional iPS studies, delivering four reprogramming factors within a single expression cassette in piggyBac, transforming the cells into iPS cells and then being able to remove the inserted gene cassette (Yusa et al., 2009, Woltjen et al., 2009) . After introducing this construct together with transposase into mouse embryonic fibroblasts, Yusa *et al*. recovered iPS colonies at frequencies of 0.1–1%, similar to those obtained with integrating viral vectors. Both groups confirmed absence of transgenic sequences in the genome by sequencing the previously identified integration sites and assessed pluripotency of integration-free iPS by analyzing teratoma and chimera formation.

1.2.4 Conclusion

In summary, major progress has been made in developing varied controlled gene expression systems, which offer variety of choices in managing gene expression in a dynamic fashion. An idea reversible gene expression system should be able to remove the inserted gene without a trace. While an idea inducible regulation system should have several key features. Basal expression should be very low, and be inducible to high level over a wide enough dose range to provide useful dose-responsive control, for example the system should resemble a rheostat rather than an on/off switch. Induction should be a positive effect (adding rather than removing a drug), and use an orally active small molecule that has no

pleiotropic effects in mammalian cells. The regulatory protein(s) should also have no effects on endogenous gene expression, and ideally should be human in origin to minimize potential immunogenicity.

These examples of reversible and inducible gene expression demonstrate that temporal control of embryonic transcription could be achieved through small-molecule ligands and synthetic receptors. In principle, engineering methods could achieve more sophisticated spatial and temporal control of gene expression, a result not achieved thus far.

1.3 The engineering strategies in patterning cell function

Spatial and temporal regulation of gene expression drives embryonic development, whereas gradients in cellular–extracellular architecture exist throughout the human body, to satisfy spatially diverse functional needs. In order to engineer complex tissues, patterning strategies have been developed and incorporated into tissue engineering. Here we review patterning strategies, which includes patterning biological environment and biological factors in engineering heterogeneous tissues and tissue interfaces.

1.3.1 Patterning the biological environments (biomaterials)

Tissues consist of cells and extracellular matrix (ECM), and differ with each other in type, content, and organization of the constituent cells and ECM components. In this section, we review the strategies that have been applied for patterning

material based gradients, and the possible applications of these patterned gradients from a tissue engineering perspective.

1.3.1.1 Patterning pore size and porosity

Among several scaffold design parameters, pore size and porosity bear prime importance. Pore size is known to affect cellular affinity and viability by influencing cellular movement, binding and spreading, intracellular signaling, and transport of nutrients and metabolites (Oh et al., 2007) Porosity governs the maximum possible accommodation of cell mass in the scaffold and potential vascularization *in vivo* (Yang et al., 2001). An interconnected pore network is desired to minimize dead volume, and tortuosity of the network affects mass transport (Malda et al., 2004). Pore shapes may also critically affect the cellular organization in the scaffolds (Zmora et al., 2004).

Because of the importance of scaffold architecture in tissue engineering, new techniques have been developed to produce anisotropic “biomimetic” scaffolds to mimic the organization of the cells or microenvironment of specific tissue with highly zonal architecture, and interfacial tissues. These new techniques include centrifugation–heat-sintering method (Oh et al., 2007), combination of melt pressing and porogen leaching (Schwarz et al., 1998), centrifugation–freeze drying method (Harley et al., 2006) and phase separation–freeze drying method (Vlierberghe et al., 2007; Dubruel et al., 2007). Using a three-dimensional (3D) printing technique in combination with porogen leaching, scaffolds having

gradients in porosity with near-uniform pore sizes were created (Sherwood et al., 2002). A novel 3D fiber deposition technique was utilized in creating scaffolds that contained a gradient in pore size with a uniform porosity (Woodfield et al., 2005). Based on these techniques, a prototype of graded bone implant with spatially varying pore size and porosity was created (Schwarz et al., 1998) and an anisotropic gradient-based pore architecture has been developed to engineer native zonal organization of the cartilage (Woodfield et al., 2005)..

1.3.1.2 Patterning substrate stiffness

Substrate stiffness affects cellular adhesion, spreading, motility, survival, and differentiation (Discher et al*.,* 2005; Li et al*.,* 2005). Research with fibroblasts, epithelial cells and smooth muscle cells has demonstrated the importance of substrate stiffness as a physical signal for cells. Generally cell contact with the substrate diminishes on increasingly softer substrates (Pelham and Wang, 1997; Engler et al., 2004) and cells migrate from softer regions to stiffer regions when exposed to a gradient in substrate stiffness (Kidoaki and Matsuda, 2008; Lo et al., 2000), a phenomenon termed “durotaxis” or “mechanotaxis”.

An effective stiffness range, however, varies between cell types and leads to cell-specific responses. For example, fibroblasts placed on various soft polyacrylamide substrates (shear modulus: <1.6kPa (Yeung et al., 2005); Young's modulus [AFM]: 14 kPa (Lo et al., 2000) ~2.7kPa (Guo et al., 2006); Young's modulus [bulk]: 1.8 kPa, ~4.4 kPa (Guo et al., 2006) display a change in

their cytoskeletons with destabilized focal adhesions, and loss in actin filament or “stress fiber” expression, resulting in a rounded cellular morphology, compared to corresponding stiffer substrates (shear modulus: >3.6 kPa (Yeung et al., 2005); Young's modulus [AFM]: 30 kPa (Lo et al., 2000) ~7.7 kPa (Guo et al., 2006); Young's modulus [bulk]: 34 kPa, 12.4 kPa(Guo et al., 2006)), where these cells adapt a flat morphology. Neurons preferentially branch on soft substrates (50Pa) compared to stiff surfaces (550Pa), while the range of stiffness that is relevant to neurons may not affect fibroblasts (Flanagan et al., 2002).

To fabricate substrates with continuous stiffness gradients at macro- and microscales, controlled photopolymerization processes have been utilized in the past, where gradients were generated by controlled photoexposure, using a gradient photomask (Jacot et al., 2006) or by varying photoexposure time (Lin-Gibson et al., 2006), or by precisely altering the crosslinker concentration using a microfluidic device (Engler et al., 2004). In many of these early investigations, polyacrylamide gels served as tools to create step and continuous compliance substrates. Various other materials that have similarly been used to create substrates with continuous stiffness gradients include a two-component dimethacrylate blend (Lin-Gibson et al., 2006), styrenated gelatin (Kidoaki and Matsuda, 2008) and PEG-diacrylate (Burdick et al., 2004).

In summary, the utility of stiffness gradients has so far been realized in studying durotaxis phenomena, micro-patterning of cells, and high-throughput screening

of materials. Probing other possible cell–biomaterial combinations using continuous stiffness gradient surfaces may provide useful information to the tissue engineering community. Stiffness gradient constructs may also be useful in interfacial tissue regeneration; however, it will require a transition from 2D surfaces to 3D environments. The challenge lies in gathering further knowledge and combining it toward designing “active” optimal bioengineered constructs.

1.3.1.3 Application: patterning ligament to bone interface

Here in this section, we reviewed the application of above material based patterning strategies in generating functional tissue interface. Tissue-to-tissue interfaces such as those that connect soft tissue to bone are ubiquitous in the body, and they are essential for facilitating synchronized joint motion and musculoskeletal function. These critical junctions between distinct tissue types are, however, prone to injury and unfortunately not re-established following standard surgical repair methods. Failure to regenerate the intricate tissue-to-tissue interface has been reported to compromise graft stability and long-term clinical outcome (Friedman et al., 1985; Lu and Jiang, 2006), consequently, engineering soft tissue to bone interface remain a significant clinical challenge.

The detailed mechanisms that drive the development of the tendon-to-bone and ligament-to-bone interface are not fully understood. Published studies revealed that, at birth, the majority of proliferating cells at the interface were near the ligament region of the insertion site, forming a fibro-cartilaginous interface after

birth (Nawata et al., 2002), however this native interface is not spontaneously regenerated between soft tissue and bone, neither can be regenerated by surgery that surgically juxtaposed soft tissue and bone (Rodeo et al., 1993). In order to address this problem, bio-mimetic stratified scaffold has been developed, coupled with spatial control over the distribution of interface relevant cell populations, to engineer the formation of cell type and phase specific matrix heterogeneity *in vitro* and *in vivo*. In a recent study, Spalazzi *et al.* developed a stratified scaffold composed of poly-α-hydroxyester nanofibers and sintered microspheres (Spalazzi et al., 2008). The scaffold induced compression of tendon grafts, which resulted in significant matrix remodeling and the expression of fibrocartilage interface-related markers such as type II collagen, aggrecan, and transforming growth factor-β3 (TGF-β3) (**Figure 1.5**). These results suggest that the stratified scaffold can be used to induce the formation of an anatomic fibrocartilage interface directly on biologically derived ACL reconstruction grafts.

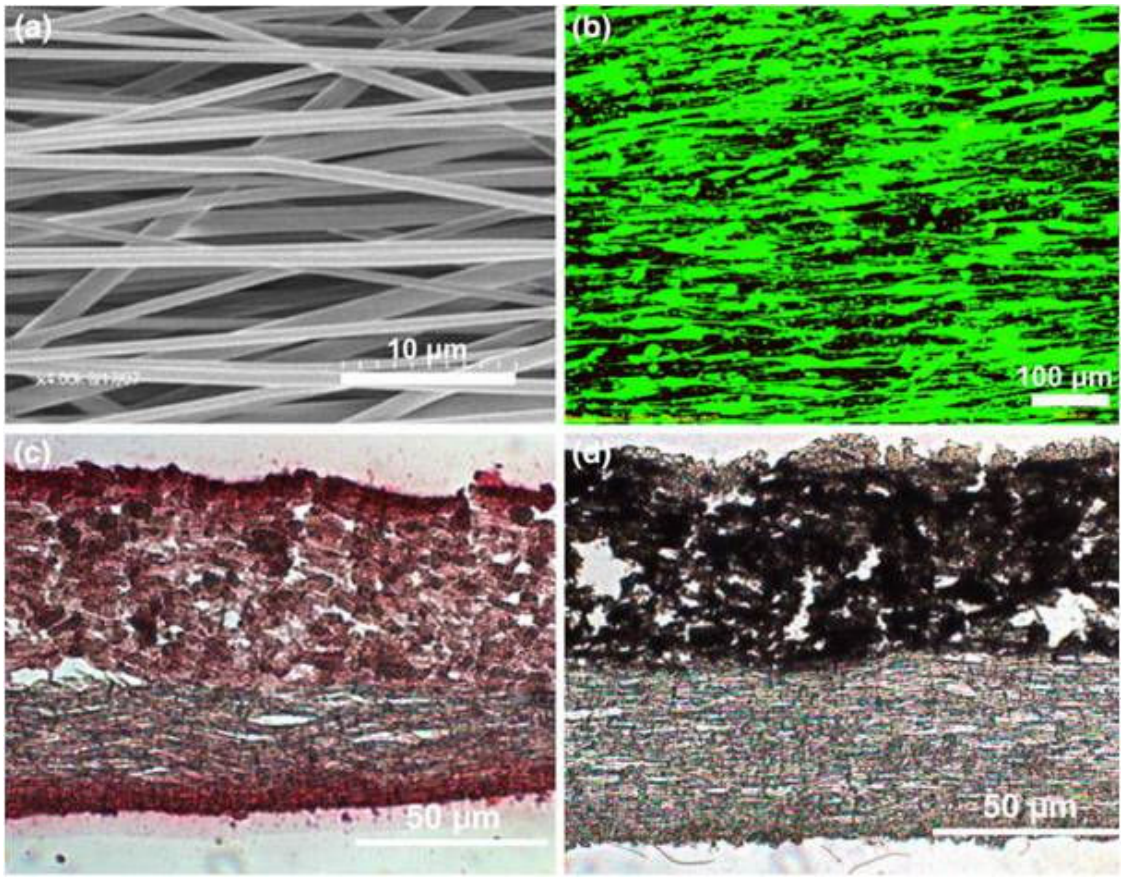

Figure 1.5 Nanofiber-based scaffold for tendon-to-bone integration (A) SEM micrograph depicting aligned fiber organization. **(B)** Fluorescence microscopy of human rotator cuff fibroblasts cultured on aligned nanofibers, cellular attachment and alignment is directed by the underlying substrate morphology. Histological analysis of a bi-phasic scaffold after 3 weeks of subcutaneous implantation, exhibiting **(C)** collagen matrix deposition and in-growth (picrosirius red) and **(D)** region-dependent distribution of mineral (von Kossa). (Moffat et al., 2009)

In summary, current strategies in material based patterning, not only validate the feasibility of engineering heterogeneous tissue or tissue interfaces, but also highlight the potential clinical application in regeneration therapy.

1.3.2 Patterning biological factors

Concentration gradients of bioactive signaling molecules, such as morphogens and growth factors, (hereafter, collectively referred to as biological factors) play a

crucial role in developmental, disease, healing and regeneration process. Several of these bioactive factors are well characterized for different tissue engineering applications, are known to induce concentration-dependent cell type–specific responses, and usually work in a synchronized manner with other similar factors during the development or repair of a natural tissue, and the spatial and temporal availability of these molecules is integral to their ability to regulate these processes and control the pattern of tissue formation (Chen and Mooney, 2003). While these factors are traditionally delivered homogeneously for *in vitro* or *in vivo* tissue engineering, both temporal and spatial control over the delivery of such factors is an understood requirement for biomimetic repair and regeneration. Thereby, spatial patterning of chemical signals is a field of growing interest for the tissue engineering community; many bio-mimetic strategies have been developed to engineer spatial and temporal aspects of exogenous delivery of such signals in tissue engineering (Vunjak-Novakovic and Kaplan, 2006; Ingber et al., 2006). The following sections of this review, we briefly discuss the two general categories of strategies adopted in patterning biological factors: patterned immobilization and patterned fluidic delivery.

1.3.2.1 Patterning immobilized biological factors

The general techniques to immobilize biological factors onto the biomaterial surface include adsorption of the molecule on the desired surface, covalent linking of the peptides/proteins via peptide bond formation through carboxylic acid (−COOH) or primary amine ($-NH_2$) moieties present on the original or

modified surface (for example, using carbodiimide chemistry), or by derivatizing with photoreactive moieties (such as azidophenyl, benzophenone, acryloyl, or aryl azide groups), all more or less governed by the chemistry of the substrate/scaffold. General methods that have been utilized to create immobilized chemical signal gradients in two dimensions and three dimensions include single- or dual-source/chamber approaches (Dodla and Bellamkonda, 2006 & 2008; Vepari and Kaplan, 2006), pump- or gravity-driven flow of factor solution (Burdick et al., 2004; Dertinger et al., 2002; Moore et al., 2006; DeLong et al., 2005), capillary-driven flow of factor solution (Caelen et al., 2000), automated printing (Ilkhanizadeh et al., 2007) and adsorption or covalent linking of proteins utilizing polymer-grafted/micropatterned substrates (Li et al., 2005; Harris et al., 2006; Mei et al., 2006). Microfluidics, photopolymerization, ATRP, and/or protein conjugation chemistry are also adopted in engineering immobilized protein gradients.

In a recent study, Hermanson's group patterned extrinsic factors onto a hydrogel matrix to direct the state and fate of neural stem cells (NSCs) (Ilkhanizadeh et al., 2007). In this study, they used an inkjet printer to print biologically active macromolecules on poly-acrylamide-based hydrogels, which were subsequently seeded with primary fetal NSCs. The advantage of using a hydrogel as a printing substrate is that, due to its high water content, it allows proteins to be hydrated throughout the printing procedure, protecting them against denaturation. Further, the extracellular matrices that surround many tissues are natural hydrogels that

serve as bioimimetic extrinsic factor reservoirs as well as supporting scaffolds (Lutolf and Hubbell, 2005). NSCs cultured on areas printed with fibroblast growth factor-2 (FGF2) remained undifferentiated, consistent with the effects of FGF2 when administered in solution. NSCs cultured in parallel on the same hydrogels but in areas printed with ciliary neurotrophic factor (CNTF) or fetal bovine serum (FBS) displayed a rapid induction of markers for astrocytic (glial fibrillary acidic protein, GFAP) or smooth muscle (smooth muscle actin, SMA) differentiation, respectively (**Figure 1.6**). These results are consistent with known actions of CNTF and FBS on NSCs. NSCs cultured on a printed gradient of increasing levels of CNTF showed a linear increase in numbers of cells expressing GFAP, demonstrating functional gradients of biologically active macromolecules can be achieved, in steering cell fate decisions and induce specific cell differentiation.

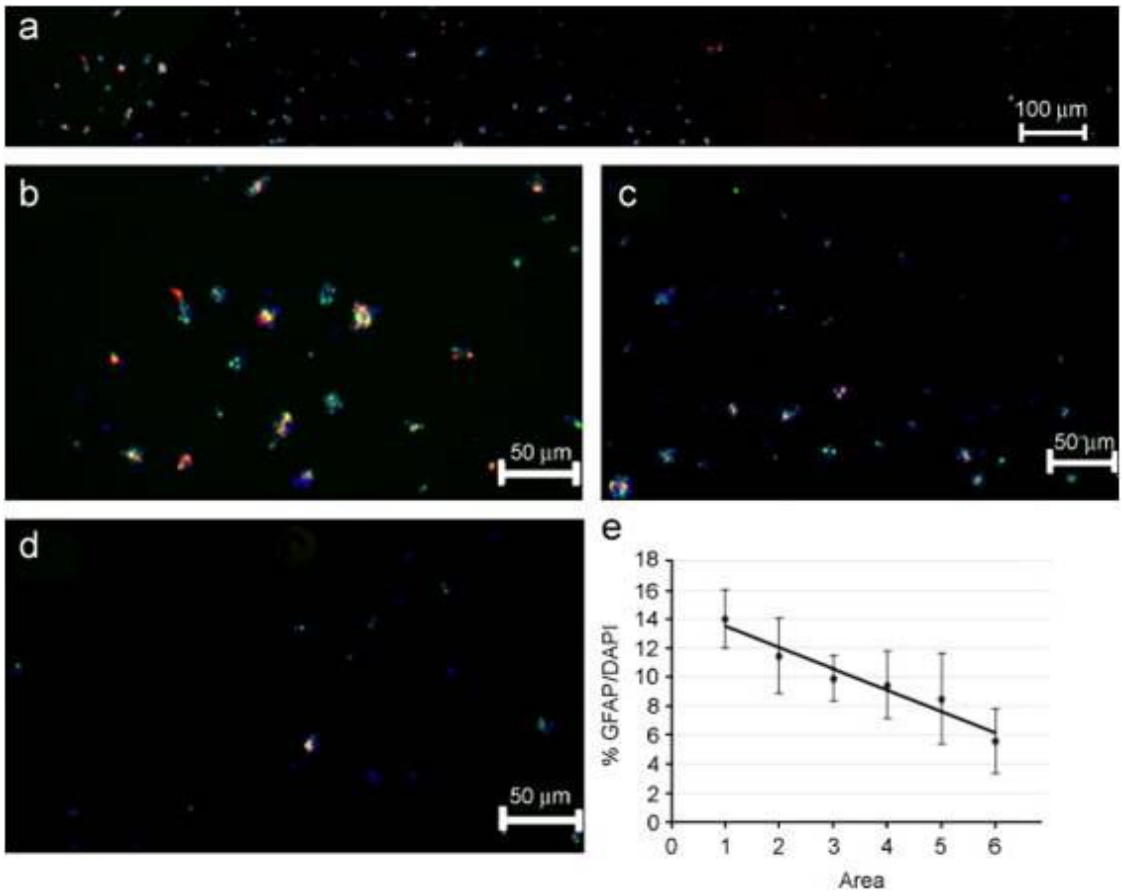

Figure 1.6 Patterned neural stem cells (NSCs) with a ciliary neurotrophic factor (CNTF) gradient. (A) The gradient of GFAP-positive cells reflects the underlying gradient of printed CNTF. Individual images of areas with high **(B)**, medium **(C)** or low **(D)** percentages of GFAP-positive cells (GFAP-red, nestin-green, DAPI-blue). **(E)** Quantification of the percentages of GFAP-positive cells present on six consecutive images acquired along the direction of the CNTF gradient, starting at the highest levels. This quantification was repeated on six separate slides. The percentage of cells expressing the GFAP ranged between 16% and 4%. (Ilkhanizadeh et al., 2007)

1.3.2.2 Patterning soluble biological factors

In the past 10 years, engineering tools have been increasingly used to develop experimental platforms that can generate gradients of soluble biological factors to allow quantitative characterization of cellular response to gradients. To control the cell–soluble factor interaction, conventional gradient-generators have been previously developed, such as the Boyden chamber (Boyden, 1962), the

Zigmond chamber (Zigmond, 1977), and micropipette-based assay (Zheng et al., 1994; Segall, 1993). Although the conventional gradient-generators have been used for studying chemotaxis and axon guidance, there are still many limitations, including the inability to maintain stable tempo-spatial gradients and the lack of the cell monitoring in a real-time manner.

To overcome limitations imposed by conventional gradient-generators, PDMS microfluidic-based gradient devices have been recently developed (Li Jeon et al., 2002; Abhyankar et al., 2006; Mao et al., 2003; Tourovskaia et al., 2008). Microfluidic devices fabricated by photo and soft lithography techniques enable the manipulation of fluid flow, the generation of stable concentration gradient profiles, and real-time monitoring of the cells (Keenan and Folch, 2008; Whitesides, 2006). Given these unique characteristics, microfluidic devices have been widely used for cell biology applications (Whitesides et al., 2001). In this section, we review the recent development of gradient-generating microfluidic platforms (*i.e.* flow-based and diffusion-based gradient device).

Microfluidic platforms enable control of concentration gradients using laminar flow and diffusion transport (**Figure 1.7**). These devices consist of the serpentine-based microchannel and a cell culture area. In general, two or three solutions are mixed and spitted in a microchannel, resulting in generating stable concentration gradients in perpendicular to the flow direction. As compared to conventional well-plate culture methods that have used uniform concentrations of

chemicals, various gradient profiles (*i.e.* single, overlapping, and dynamic switch gradient profile) can be rapidly generated in a single microfluidic device.

Various profiles and steepness of concentration gradients can be generated in a single microfluidic device and the cocktail mixtures of soluble factors can be precisely delivered into each microchannel, resulting in performing high-throughput experiments. In particular, we can investigate the effect of autocrine and paracrine signaling on cell growth and differentiation in a flow-based microfluidic gradient device. Furthermore, the microfabrication process to create flow-based microfluidic devices is relatively straightforward. The flow-based microfluidic devices also have some limitations, such as the inability to maintain secreted molecules (*i.e.* autocrine, paracrine signaling), the lack of minimizing the shear stress, the inability to generate gradient profiles in a 3-D scaffold, and the lack of creating chaotic mixing (Walker et al., 2005; Gunawan et al., 2006).

Recently, a flow-based rapid generation of long-range concentration gradients in a portable microfluidic device has been reported (Du et al., 2009). Portable microfluidic-based gradient devices can be generated by surface tension (Meyvantsson et al., 2008). The difference in the surface tension between larger and smaller reservoirs as well as the evaporation has been employed to deliver the solution into the microchannel without external syringe pumps. Briefly, the forward and backward flow derived from a passive pump and evaporation in a microfluidic device enables the generation of centimeter-long concentration

gradients in a simple and rapid manner. Furthermore, a multi-purpose microfluidic system has been developed to create the combinatorial gradient profiles controlled by a binary multiplexer (Cooksey et al., 2009). Various flow-based gradient patterns were generated by selecting combinations of 16 inlet multiplexer controlled by a programmable Labview system. In addition, multi-component protein gradients have been generated by using the depletion effects in a flow-based microfluidic device (Fosser and Nuzzo, 2003).

Another approach for creating concentration gradients in a microfluidic device is to use pure diffusion through the membrane or hydrogel for generating diffusion-based gradients (**Figure 1.7**). As compared with the gradient-generating microfluidic device, diffusion-based microfluidic devices have several advantages, such as shear stress is negligible, the presence of secreted molecule is maintained, and gradients can be generated in a 3-D scaffold. Still, the diffusion-based microfluidic devices cannot generate rapid and dynamic gradient profiles.

Previous diffusion-based systems have generated simple gradients on a 2D surface. To create complex gradients in a 3-D environment, the diffusion-based gradient has been recently generated in a multi-layer microfluidic device containing hydrogels (Wu et al., 2006). The molecules in two reservoirs were diffused through the hydrogel in the middle layer and molecular gradients containing complex shapes (*i.e.* W-shaped, steplike, and parabolic shape) were generated in a fluidic microchannel of the bottom PDMS layer.

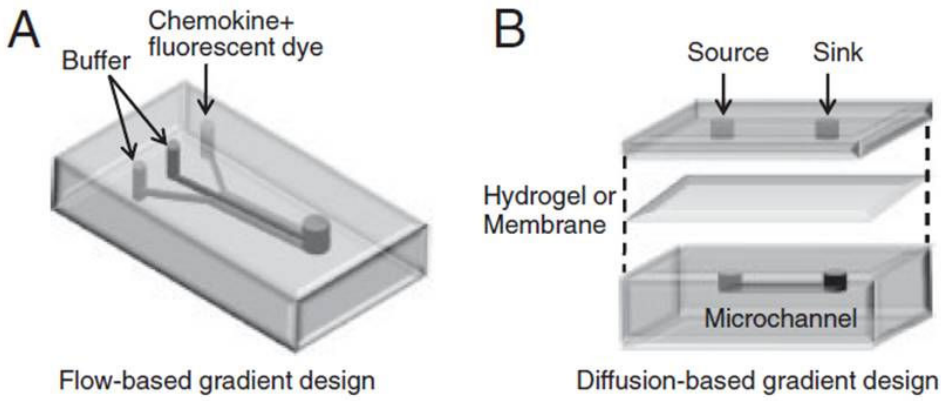

Figure 1.7 The schematic designs of flow-based and diffusion-based microfluidic gradient devices (A) Flow-based microfluidic platforms enable the control of concentration gradients using laminar flow and diffusive mixing. **(B)** Diffusion–based microfluidic platforms generate concentration gradients using pure diffusion through the membrane or hydrogel.

1.3.2.3 Application: Patterned stem cell differentiation

Stem cell is a promising cell type for regenerative medicine and cell-based therapy, because it can differentiate into specific cell lineages (Vazin and Schaffer, 2010; Bhattacharya et al., 2009; Azarin and Palecek, 2010). Embryonic stem cells are derived from the blastocyst (*i.e.* inner cell mass), adult stem cells are obtained from the tissue-specific environment (*i.e.* bone marrow, muscle) (Lutolf et al., 2009). Although the potential of stem cells for treating degenerative diseases and human disorders, major challenges to prevent widespread use for clinical cell-based therapeutic applications are remained, such as the inability to control the growth and differentiation of stem cells in a homogeneous or patterned manner (Vazin and Schaffer, 2010). Conventional culture methods cannot control the stem cell behavior in a well-defined microenvironment. To address these limitations, microfabricated gradient platforms have been recently

developed to mimic the embryonic development as well as to understand the regulatory mechanism to direct embryonic and adult stem cell fate.

For instance, the growth and differentiation of human neural stem cells have been investigated in a flow-based microfluidic device (Chung et al., 2005). Neural stem cells can self-renew and differentiate into three cell types, such as neuron, astrocyte, and oligodendrocyte. The concentration gradients of growth factor mixtures containing EGF, fibroblast growth factor 2 (FGF2), and platelet-derived growth factor were stably generated in a microfluidic device as conventional assays have not previously been possible. The quantitative analysis showed that the growth of human neural stem cells was directly proportional to growth factor concentrations, whereas their differentiation into astrocyte was inversely proportional to growth factor concentrations. Another similar study investigated the proliferation and differentiation of neural progenitor cells derived from human embryonic stem cells in an osmotic pump-based microfluidic device (Park et al., 2009). This device mimicked to generate sonic hedgehog (Shh), FGF8, and bone morphogenetic protein 4 (BMP4) gradients that could be created during early brain development. The quantitative analysis of overlapping exogenous cytokine gradients (Shh/FGF8 or Shh/BMP4) showed that TuJ1-positive neurons were more highly expressed in Shh/FGF8 gradients as compared with Shh/BMP4 gradients (**Figure 1.8**).

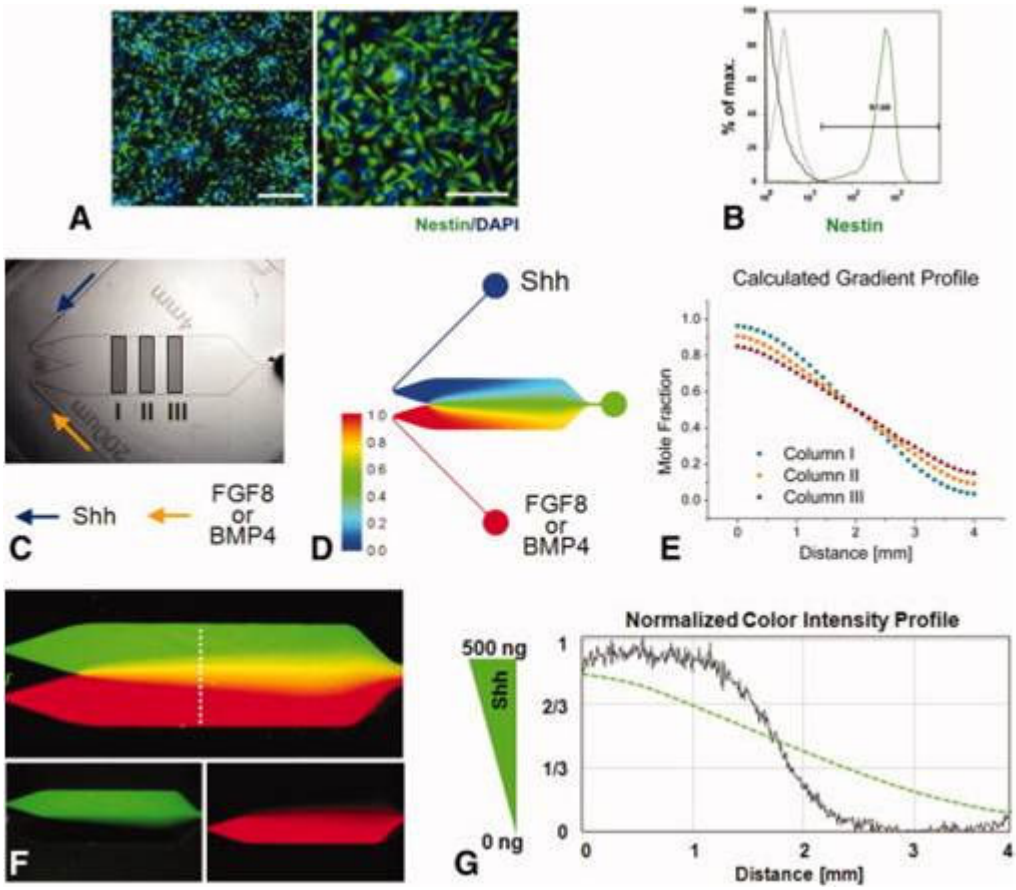

Figure 1.8 Differentiation of human embryonic stem cell (ESC) derived neural progenitor cells in the microfluidic gradient chip The purity of the input cell population was confirmed by immunostaining **(A)** and flow cytometry **(B)** using antibody against Nestin. Scale bars = 100 μm (A, left) and 50 μm (A, right). A flow cytometric plot **(B)** shows the no-stain control profile (black solid line), the isotype control IgG-staining profile (black dotted line), and the Nestin staining profile (green solid line). After seeding Nestin-positive neural progenitor cells into the gradient chip, two pairs of cytokines were added to the culture medium: Shh and FGF8; Shh and BMP4. **(C)** Two different cytokine flows (Shh vs. FGF8 or BMP4) in the main channel in which three observation window columns (I, II, III) were located. **(D–E)** Gradient profile estimated by the computational simulation. **(F)** Visualization of the concentration gradient of fluorescent-labeled proteins (cholera toxin subunit B conjugated with Alexa Fluor 488 and 594). **(G)** Normalized color intensity (green fluorescence) shows that the gradient profile covers about one third of the main channel, implying the cytokine gradient profiles will follow the green dotted line. (Park et al., 2009)

Another example is a diffusion-based gradient device used to culture human embryonic stem cells (Abhyankar and Beebe, 2007). The device developed by the multi-layer soft lithography technique was consisted of aperture template (top

layer), microwell reservoir embedding the porous membrane with 0.2 μm pore diameter (middle layer), and assay microchannel (bottom layer) that could generate molecular gradients. A small droplet with cell suspension on an aperture template enabled the generation of the spatial-temporal patterning in an assay microchannel through the microwell reservoir. Thus, human embryonic stem cells were patterned on a mouse embryonic fibroblast feeder layer. Furthermore, normal murine mammary gland (NMuMG) epithelial cells exposed to the gradient of the exogenous factor were patterned on an essay microchannel (**Figure 1.9**). Therefore, these microfluidic gradient platforms could be useful tools for controlling embryonic development and directing stem cell fate.

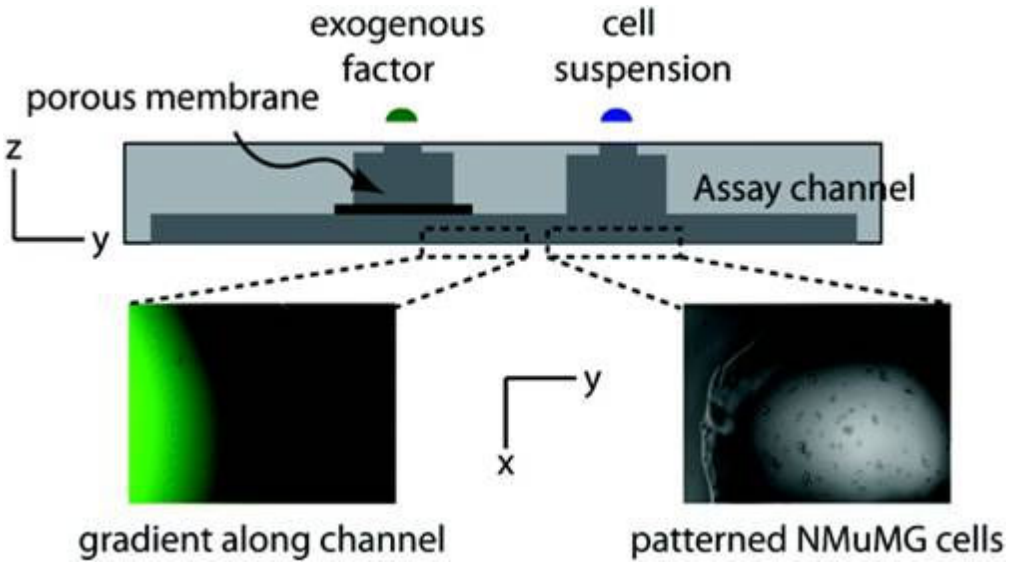

Figure 1.9 Spatial patterning of normal murine mammary gland (NMuMG) cells NMuMG cells are patterned in one corridor, and a gradient of the fluorophore Alexa 488 is created in the assay channel. A porous membrane is incorporated in the microwell to increase the fluidic resistance of the system, and the fluorophore is added to the microwell. The molecules diffuse through the membrane and create a gradient in the channel. (Abhyankar and Beebe, 2007)

1.3.3 Conclusion

Basic concepts for formulating multiple tissue systems (Mikos et al., 2006) rely on one or more forms of chemical or physical stimuli, which affect cell-specific movement, substrate affinity, or tissue formation (Singh et al., 2008). Techniques to create bioactive factor gradients vary in terms of scale, accuracy, flexibility, and stability of gradient profiles (Rosoff et al., 2005).

In summary, hydrogel-based approaches have provided many routes to generate soluble or immobilized bioactive factor gradients in both two dimensions and three dimensions, thereby has been widely used in studying the chemotaxis and haptotaxis. Surface modification, photopolymerization techniques and microfluidic strategies have been used to create gradients of surface-bound factors on polymeric surfaces. However, most two-dimensional (2D) gradients formed utilizing these techniques have been used for high-throughput screening, and have not necessarily been translated to 3D interfacial tissue applications. Even fewer attempts have been made to generate such gradients in degradable 3D macroporous scaffolds, a prototype that constitutes a significant percentage of commonly used tissue engineering scaffolds. In this regard, primary issues to be addressed appear to pertain to the translation of many 2D physicochemical gradient-generation techniques from two dimensions to three dimensions.

1.4 Combinational Strategy

In previous section, we reviewed the importance of spatial temporal regulation of gene expressions in development process, and current progress on in developing biological strategies in regulating gene expression and engineering strategies in patterning varied biological factors. By far, based on these strategies, we are able to regulate specific gene expression in a temporal manner, or pattern certain cell functions at topobiological level, cellular level and molecular level (mainly growth factor and signaling factors). However, few efforts have been made in combining the biological and engineering strategies, directly patterning gene expression at the transcriptional level, which may lead to varied and sophisticated control of downstream cellular functions,

Recently an alternate approach was developed in patterning localized gene transfection, leading to a novel strategy to pattern specific gene expression, the related cell function. One study patterned localized gene transduction in promoting local production of angiogenic molecules factor by the cells resident in the tissue (Ennett and Mooney, 2002). More recently, Phillips *et al.* presented a method for localizing continuous gradients onto interfacial constructs, and not relying on growth factor elution to induce cell differentiation (Phillips et al., 2008).

Using a time-dependent dipping procedure with a motorized dip coater, a gradient of retrovirus encoding runt-related transcription factor 2 (Runx2) was deposited on top of a gradient of poly(L-lysine). The gradient was oriented along

the length of the collagen scaffold. When seeded with fibroblasts, the construct was successful in creating a gradient of osteoblastic differentiation (osteoblasts and fibroblasts on one construct). *In vivo,* the mineral distribution appeared biphasic after just 2 weeks. *In vitro*, constructs maintained a continuous mineral gradient for 42 days (**Figure 1.10**). This behavior is reminiscent of an application for ligament–bone interface engineering and other cartilage–bone applications (Tampieri et al., 2008), where tissue generation patterns did not necessarily adhere to the initial scaffold design. In addition, Phillips *et al.*'s technique induced a functional gradient from a strictly biochemical surface gradient.

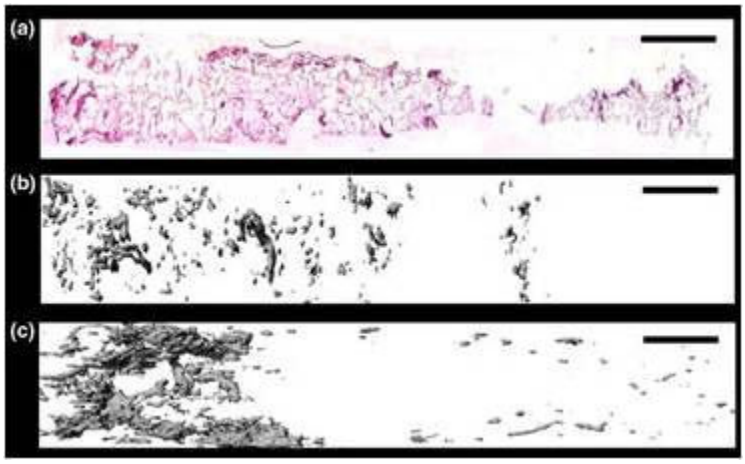

Figure 1.10 Continuously graded constructs for soft tissue—bone integration (A) Immunohistochemical staining for eGFP (pink) counterstained with hematoxylin (blue) revealed a gradient of Runx2—expressing cells. **(B)** Mineral deposition via *μ*CT after 42 days of *in vitro* culture. **(C)** Mineral deposition via *μ*CT after 2 weeks of ectopic *in vivo* implantation (Phillips et al., 2008).

Despite to the initial success, this local gene transfection mediated gene patterning may ultimately be limited in their success due to the short-term expression of the plasmid DNA or adenoviral vectors used in these efforts. One

approach to extend, in a controllable manner, the expression of the plasmid encoding the factor(s) of interest is to immobilize the plasmid in a polymer system that enables its sustained release. Incorporation of plasmid DNA into poly (lactide-*co*-glycolide) scaffolds can lead to a significant increase in the duration of expression (Shea et al., 1999) and condensation of the plasmid prior to polymer encapsulation can significantly increase the level and duration of expression *in vivo (*Huang et al., 2005). However, the controlled release of DNA or viral vectors did not ultimately address the issue of low efficiency and limited usage, more sophisticated strategies based on controllable gene expression should be adopted in patterning gene expression in a more dynamic and precise manner.

1.5 Overview of the thesis

1.5.1 Project 1: Regulation of cell proliferation - Controllable expansion of primary cardiomyocytes by reversible immortalization

One of the challenges for tissue engineering is limited cell sources, especially for regeneration therapy. For example, heart is an organ that fails beyond repair, because of the intrinsic inability of the damaged heart tissue to regenerate after injury. Clearly, tissue engineering could be most valuable for the reconstruction of malformed hearts in children and the regeneration of failing hearts in adults.

A great deal of effort has been spent exploring the reparative capabilities of exogenous stem and progenitor cells. Utilization of adult stem cells from various sources has been motivated by the advantages of alleviating concerns about

immune rejection or transmission of disease. Although adult stem cells were first isolated from the bone marrow, recent literature supports their presence in a variety of extramedullary organs including adipose tissue, dental pulp, circulating blood, amniotic fluid, and joint synovium(Gimble et al., 2007; Anker et al., 2003; Pei et al., 2008; Miura et al., 2003; Zhang et al., 2004). Limitations of the adult stem cells investigated include the limited capacity of mesenchymal stem cells (MSCs) to induce myogenesis, and the inability of skeletal myocytes for proper electrical coupling with cardiac myocytes. The ongoing efforts to derive phenotypically stable cardiac and vascular cell populations from human ESCs (hESCs), in numbers sufficient for tissue engineering hold promise that the advantages of these cells will be fully utilized (Yang et al., 2008). But, the use of these cells carries the risk of uncontrolled differentiation and teratoma formation.

The Cre/loxP system is a measure widely used as an effective tool of gene targeting to evaluate function and differentiation in developmental processes of specific individual genes. Cre recombinase derived from Escherichia coli P1 phage can independently perform a series of responses, including 1) recognizing loxP sequence consisting of 34 base pairs, and 2) binding to its recombination site and cutting off the intervened DNA that is coded between loxP sequences (Sternberg et al., 1981). Previously Cre/loxP site-specific recombination was applied to reversibly induce the proliferation of human cells, by transferring immortalization genes between a pair of loxP sequences. Once cells are immortalized by introduction of loxP-flanked immortalizing genes, and proliferate

to sufficient numbers, the immortalizing gene can be cut out by transferring Cre recombinase. By this method, a large amount of reverted form of cells with original pre-immortalized status can be obtained.

We explored a new strategy for expanding the non-proliferating primary cardiomyocytes, by immortalization that requires the transfection of combination of immortalization genes (Hahn et al., 1999), followed by subsequently removal of these genes by Cre-loxP site recombination, thereby reversal into the terminally differentiated phenotype after the cells are expanded in culture. By using this strategy, we could expand primary cardiomyocytes by gene transfer, which has potential for providing large amounts of the patient's own cardiomyocytes for cell therapy.

We immortalized the primary rat neonatal cardiomyocytes by two different combinations of genes: TAg and Bmi-1/hTERT. After cells expansion, we used Cre mediated gene reversion, reverting immortalized cells back to cardiac phenotype. We demonstrated reversible transfer of cell immortalization gene can be used to expand primary cardiac cells to numbers that are sufficient for basic research and regenerative medicine

Publication:

Y. Zhang, E. Nuglozeh, E. Toure, AM. Schmidt. G. Vunjak-Novakovic. Controllable Expansion of Primary Cardiomyocytes by Reversible Immortalization. *Hum Gene Ther.* (12):1687-1696 2009.

1.5.2 Project 2: Patterning cells differentiation - Patterning osteogenesis by inducible gene expression in microfluidic systems

During native tissue development and remodeling, the differentiating cells form boundaries and interfaces, in response to spatial gradients of gene expression and cytokines distribution, whereas the formation of transitional zones in vitro remains a significant challenge.

We explored an alternate strategy to pattern gene expression within a cell population, by patterning the gene expression mdulators with a multiple - laminar fluidic system. The patterned delivery of gene expression modulators in mulitple -laminar flow system, leads to patterned gene expression, and subsequently patterned gene mediated cell differentiation.

Using a bone–soft tissue interface as a model, we proposed a strategy to spatially regulate expression and secretion of the bone morphogenetic protein (BMP-2), by using flow patterning of inducible BMP-2 gene expression. As BMP-2 plays an important role in osteogenesis and bone metabolism as a powerful inducer of osteoblast differentiation *in vitro* and bone formation *in vivo (*Hay et al., 1999; Ruhe et al., 2004*)*. Combining Doxcycline regulated inducible BMP-2

expression and multi-laminar fluidic system, we developed a novel approach to spatially regulate expression of BMP-2 within tissue-engineered constructs, and thereby modulated osteogenic differentiation, in engineering and studying tissue interface. In summary, we developed a strategy to engineer osteo-mesenchymal tissue interface by patterning inducible BMP-2 expression within a laminar fluidic system, the strategy presented a innovative method to pattern particular gene expression in an inducible manner.

Publication:

Y. Zhang, Z. Gazit, G. Pelled, D. Gazit, G. Vunjak-Novakovic. Patterning osteogenesis by inducible gene expression in microfluidic culture systems. *Integrative Biology* 3(1):39-47 2011.

1.5.3 Project 3: Patterning pluripotency - Patterning embryonic cell differentiation by patterned inducible Nanog expression in multi-laminar fluidic system

Embryonic stem cells (hESCs), derived from the blastocyst inner cell mass, provide a potentially unlimited supply of cells that may be directed to differentiate toward specific lineages and a model to study the early embryo development. The mechanisms by which inductive signals control the identity, proliferation and timing of differentiation of progenitor cells in establishing spatial pattern in developing embryonic tissues remain poorly understood, which presents

challenges as well opportunities to develop innovative strategies in study the spatial control of embryonic differentiation.

Our previous study demonstrated an alternative strategy to pattern gene expression within a cell population, by patterning the gene expression modulators with a multiple - laminar fluidic system. We proposed this strategy could be a good platform in studying and engineering the spatial control of embryonic differentiation.

We chose an inducible Nanog expressing cells line, under control of a Nanog gene expression vector, composed of a shRNA fragment, suppressing cells' endogenous Nanog, coupled with a Tet-on inducible expression system of exogenous Nanog. This unique expression vector offers precise control of Nanog expression in cells. As Nanog safeguards the pluripotency by reversing/ resisting nascent epigenetic modification, the absence of Nanog provides window of opportunity when intrinsic / exogenous signals consolidate into differentiation commitment. Therefore by patterning the delivery of Dox to the cultured cells in laminar flow system, we effectively pattern the expression of Nanog expression and thereby modulate Nanog mediated embryonic stem cells differentiation.

Publication:

Y. Zhang, A. Sevilla, L.Q. Wan, I.R. Lemischka, G. Vunjak-Novakovic. Patterning embryonic differentiation by inducible Nanog gene expression in laminar fluidic culture system. *[In Preparation]*

1.6 References

1. Abhyankar VV, Lokuta MA, Huttenlocher A, Beebe DJ. Characterization of a membrane-based gradient generator for use in cell-signaling studies. *Lab Chip* 6(3):389-393, 2006
2. Abhyankar VV, Beebe DJ. Spatiotemporal micropatterning of cells on arbitrary substrates. *Anal Chem.* 79(11):4066-4073, 2007
3. Affolter M, Basler K. The Decapentaplegic morphogen gradient: from pattern formation to growth regulation. *Nat Rev Genet.* 8(9):663-674, 2007
4. Anker, P.S., Scherjon, S.A., Kleijburg-van der Keur, C.,Noort, W.A., Claas, F.H.J., Willemze, R., Fibbe, W.E., and Kanhai, H.H.H. Amniotic fluid as a novel source of mesenchymal stem cells for therapeutic transplantation. *Blood* 102, 1548-1559, 2003.
5. Ashe H, Briscore The interpretation of morphogen gradients. *J. Development* 133,385-394, 2006
6. Azarin SM, Palecek SP. Development of Scalable Culture Systems for Human Embryonic Stem Cells. *Biochem Eng J.* 48(3):378-389, 2010
7. Bhattacharya B, Puri S, Puri RK. A review of gene expression profiling of human embryonic stem cell lines and their differentiated progeny. *Curr Stem Cell Res Ther*. 4(2):98-106, 2009
8. Branda CS, Dymecki SM. Talking about a revolution: The impact of site-specific recombinases on genetic analyses in mice. *Dev Cell* 6:7–28, 2004
9. Bodnar A. G.; Ouellette M.; Frolkis M.; Holt S. E.; Chiu C. P.; Morin G. B.; Harley C. B.; Shay J. W.; Lichtsteiner S.; Wright W. E. Extension of life-span by introduction of telomerase into normal human cells. *Science* 279:349-352; 1998
10. Boyden S. The chemotactic effect of mixtures of antibody and antigen on polymorphonuclear leucocytes. *J Exp Med.*115:453-466, 1962.
11. Burdick JA, Khademhosseini A, Langer R. Fabrication of gradient hydrogels using a microfluidics/photopolymerization process. *Langmuir* 20(13):5153-5156, 2004
12. Caelen I. Bernard A. Juncker D. Michel B. Heinzelmann H. Delamarche E. Formation of gradients of proteins on surfaces with microfluidic networks. *Langmuir* 16:9125-9130, 2000.
13. Chen RR, Mooney DJ. Polymeric growth factor delivery strategies for tissue engineering. *Pharm Res*. 20(8):1103-1112, 2003

14. Christopherson KS, Mark MR, Bajaj V, Godowski PJ. Ecdysteroid-dependent regulation of genes in mammalian cells by a Drosophila ecdysone receptor and chimeric transactivators, *Proc. Natl. Acad. Sci. USA* 89: 6314–6318, 1992

15. Chung BG, Flanagan LA, Rhee SW, Schwartz PH, Lee AP, Monuki ES, Jeon NL. Human neural stem cell growth and differentiation in a gradient-generating microfluidic device. *Lab Chip* 5(4):401-406, 2005

16. Cooksey GA, Sip CG, Folch A. A multi-purpose microfluidic perfusion system with combinatorial choice of inputs, mixtures, gradient patterns, and flow rates. *Lab Chip* 9(3):417-426, 2009

17. Cudré-Mauroux C. Occhiodoro T. Knig S. Salmon P. Bernheim L. Trono D. Lentivector-mediated transfer of Bmi-1 and telomerase in muscle satellite cells yields a Duchenne myoblast cell line with long-term genotypic and phenotypic stability. *Hum. Gene Ther.* 14:1525–153, 2003

18. De Graaf M, Zivkovic D, Joore J. Hormone-inducible expression of secreted factors in zebrafish embryos, *Dev. Growth Differ*. 40 577–582, 1998

19. DeLong SA, Gobin AS, West JL. Covalent immobilization of RGDS on hydrogel surfaces to direct cell alignment and migration. *J Control Release* 109(1-3):139-148, 2005

20. Dertinger SK, Jiang X, Li Z, Murthy VN, Whitesides GM. Gradients of substrate-bound laminin orient axonal specification of neurons. *Proc Natl Acad Sci U S A*. 99(20):12542-12547, 2002

21. Discher DE, Janmey P, Wang YL. Tissue cells feel and respond to the stiffness of their substrate. *Science* 310(5751):1139-1143, 2005

22. Dodla MC, Bellamkonda RV. Anisotropic scaffolds facilitate enhanced neurite extension in vitro. *J Biomed Mater Res A* 78(2):213-221, 2006

23. Dodla MC, Bellamkonda RV. Differences between the effect of anisotropic and isotropic laminin and nerve growth factor presenting scaffolds on nerve regeneration across long peripheral nerve gaps. *Biomaterials* 29(1):33-46, 2008

24. Driever W, Nüsslein-Volhard C. A gradient of bicoid protein in Drosophila embryos. *Cell* 54(1):83-93,1988

25. Driever W, Nüsslein-Volhard C. The bicoid protein determines position in the Drosophila embryo in a concentration-dependent manner. *Cell* 54(1):95-104, 1988

26. Du Y, Shim J, Vidula M, Hancock MJ, Lo E, Chung BG, Borenstein JT, Khabiry M, Cropek DM, Khademhosseini A. Rapid generation of spatially and temporally controllable long-range concentration gradients in a microfluidic device. *Lab Chip* 9(6):761-767, 2009

27. Dubruel P, Unger R, Vlierberghe SV, Cnudde V, Jacobs PJ, Schacht E, Kirkpatrick CJ. Porous gelatin hydrogels: 2. In vitro cell interaction study. *Biomacromolecules* 8(2):338-344, 2007

28. Eilers M, Picard D, Yamamoto KR, Bishop JM. Chimaeras of myc oncoprotein and steroid receptors cause hormone-dependent transformation of cells. *Nature* 340 66–68, 1989.

29. Engler A, Bacakova L, Newman C, Hategan A, Griffin M, Discher D. Substrate compliance versus ligand density in cell on gel responses. *Biophys J.* 86:617-628, 2004

30. Ennett AB, Mooney DJ. Tissue engineering strategies for in vivo neovascularisation. *Expert Opin Biol Ther*. 2(8):805-818, 2002

31. Esengil H, Chang V, Mich JK, . Chen JK. Small-molecule regulation of zebrafish gene expression. *Nat. Chem. Biol*. 3 154–155, 2007

32. Feil R, Wagner J, Metzger D, Chambon P. Regulation of Cre recombinase activity by mutated estrogen receptor ligand-binding domains. *Biochem Biophys Res Commun*. 237:752–757, 1997

33. Flanagan LA, Ju YE, Marg B, Osterfield M, Janmey PA. Neurite branching on deformable substrates. *Neuroreport* 13(18):2411-2415, 2002

34. Forest C.; Czerucka D.; Negrel R.; Ailhaud G. Establishment of a human cell line after transformation by a plasmid containing the early region of the SV40 genome. *Cell Biol. Int. Rep*. 7:73-81; 1983

35. Fosser KA, Nuzzo RG. Fabrication of patterned multicomponent protein gradients and gradient arrays using microfluidic depletion. *Anal Chem*. 75(21):5775-5782, 2003

36. Friedman MJ, Sherman OH, Fox JM, Del Pizzo W, Snyder SJ, Ferkel RJ. Autogeneic anterior cruciate ligament (ACL) anterior reconstruction of the knee. A review. *Clin Orthop Relat Res*. (196):9-14, 1985

37. Geurts AM, Collier LS, Geurts JL, Oseth LL, Bell ML, Mu D, Lucito R, Godbout SA, Green LE, Lowe SW, Hirsch BA, Leinwand LA, Largaespada DA. Gene mutations and genomic rearrangements in the mouse as a result of transposon mobilization from chromosomal concatemers. *PLoS Genet*. 29;2(9):e156, 2006

38. Gimble, J.M., Katz, A.J., and Bunnell, B.A. Adipose-derived stem cells for regenerative medicine. *Circ Res* 100, 1249-1260, 2007

39. Gossen M, Bujard H. Tight control of gene expression in mammalian cells by tetracycline-responsive promoters. *Proc Natl Acad Sci U S A.* 89(12):5547-5551, 1992

40. Gossen M, Freundlieb S, Bender G, Müller G, Hillen W, Bujard H. Transcriptional activation by tetracyclines in mammalian cells. *Science* 268(5218):1766-1769, 1995

41. Green H, Easley K, Iuchi S. Marker succession during the development of keratinocytes from cultured human embryonic stem cells. *Proc Natl Acad Sci U S A*. 100(26):15625-15630, 2003

42. Green S, Chambon P. Oestradiol induction of a glucocorticoid-responsive gene by a chimaeric receptor, *Nature* 325 75–78, 1987

43. Gunawan RC, Silvestre J, Gaskins HR, Kenis PJ, Leckband DE. Cell migration and polarity on microfabricated gradients of extracellular matrix proteins. *Langmuir* 22(9):4250-4258, 2006

44. Guo WH, Frey MT, Burnham NA, Wang YL. Substrate rigidity regulates the formation and maintenance of tissues. *Biophys J.* 90(6):2213-2220, 2006

45. Gurdon JB, Bourillot PY. Morphogen gradient interpretation. *Nature* 413(6858):797-803, 2001

46. Hahn, W.C., Counter, C.M., Lundberg, A.S., Beijersbergen, R.L., Brooks, M.W., and Weinberg, R.A. Creation of human tumour cells with defined genetic elements. *Nature* 400, 464-468, 1999

47. Harley BA, Hastings AZ, Yannas IV, Sannino A. Fabricating tubular scaffolds with a radial pore size gradient by a spinning technique. *Biomaterials* 27(6):866-874, 2006

48. Harris BP, Kutty JK, Fritz EW, Webb CK, Burg KJ, Metters AT. Photopatterned polymer brushes promoting cell adhesion gradients. *Langmuir* 22(10):4467-4471, 2006

49. Hashimoto N. Kiyono T. Wada M.R. Shimizu S. Yasumoto S. Inagawa M. Immortalization of human myogenic progenitor cell clone retaining multipotentiality. *Biochem. Biophys. Res. Commun*. 348:1383–1388, 2006

50. Hay E, Hott EM, Graulet AM, Lomri A, Marie PJ. Effects of bone morphogenetic protein-2 on human neonatal calvaria cell differentiation *J. Cell. Biochem*. 72,81-93, 1999

51. Huang YC, Riddle K, Rice KG, Mooney DJ. Long-term in vivo gene expression via delivery of PEI-DNA condensates from porous polymer scaffolds. *Hum Gene Ther*. 16(5):609-617, 2005

52. Ilkhanizadeh S, Teixeira AI, Hermanson O. Inkjet printing of macromolecules on hydrogels to steer neural stem cell differentiation. *Biomaterials* 28(27):3936-3943, 2007

53. Indra AK, Warot X, Brocard J, Bornert JM, Xiao JH, Chambon P, Metzger D. Temporally-controlled site-specific mutagenesis in the basal layer of the epidermis: comparison of the recombinase activity of the tamoxifen-inducible Cre-ER(T) and Cre-ER(T2) recombinases. *Nucleic Acids Res*. 27:4324–4327, 1999

54. Ingber DE, Mow VC, Butler D, Niklason L, Huard J, Mao J, Yannas I, Kaplan D, Vunjak-Novakovic G. Tissue engineering and developmental biology: going biomimetic. *Tissue Eng*. 12(12):3265-3283, 2006

55. Jacot JG, Dianis S, Schnall J, Wong JY. A simple microindentation technique for mapping the microscale compliance of soft hydrated materials and tissues. *J Biomed Mater Res A*. 79(3):485-494, 2006

56. Jamora C, DasGupta R, Kocieniewski P, Fuchs E. Links between signal transduction, transcription and adhesion in epithelial bud development. *Nature* 422(6929):317-322, 2003

57. Jernvall J, Thesleff I. Reiterative signaling and patterning during mammalian tooth morphogenesis. *Mech Dev*. 92(1):19-29, 2000

58. Joyner AL, Zervas M. Genetic inducible fate mapping in mouse: establishing genetic lineages and defining genetic neuroanatomy in the nervous system. *Dev Dyn.* 235:2376–2385, 2006

59. Keenan TM, Folch A. Biomolecular gradients in cell culture systems. *Lab Chip* 8(1):34-57, 2008

60. Keller R. Shaping the vertebrate body plan by polarized embryonic cell movements. *Science* 298(5600):1950-1954, 2002

61. Kidoaki S, Matsuda T. Microelastic gradient gelatinous gels to induce cellular mechanotaxis. *J Biotechnol.* 133(2):225-230, 2008

62. Kobayashi N. Noguchi H. Westerman K.A. Watanabe T. Matsumura T. Totsugawa T. Fujiwara T. Leboulch P. Tanaka N. Cre/loxP-based reversible immortalization of human hepatocytes. *Cell Transplant.* 10:383–386, 2001

63. Kolm PJ, Sive HL. Efficient hormone-inducible protein function in Xenopus laevis, *Dev. Biol.* 171: 267–272, 1995

64. Koster MI, Kim S, Mills AA, DeMayo FJ, Roop DR. p63 is the molecular switch for initiation of an epithelial stratification program. *Genes Dev.* 18(2):126-131, 2004

65. Koster MI, Roop DR. p63 and epithelial appendage development. *Differentiation* 72(8):364-370, 2004

66. Kowolik C.M. Liang S. Yu Y. Yee J.K. Cre-mediated reversible immortalization of human renal proximal tubular epithelial cells. *Oncogene* 23:5950–5957, 2004

67. Lane D. P. Cell immortalization and transformation by the p53 gene. *Nature* 312:596-597; 1984.

68. Lewandoski M. Conditional control of gene expression in the mouse. *Nat Rev Genet.* 2:743–755, 2001

69. Li B, Ma Y, Wang S, Moran PM. A technique for preparing protein gradients on polymeric surfaces: effects on PC12 pheochromocytoma cells. *Biomaterials* 26(13):1487-1495, 2005

70. Li S, Guan JL, Chien S. Biochemistry and biomechanics of cell motility. *Annu Rev Biomed Eng*. 7:105-150, 2005

71. Li Jeon N, Baskaran H, Dertinger SK, Whitesides GM, Van de Water L, Toner M. Neutrophil chemotaxis in linear and complex gradients of interleukin-8 formed in a microfabricated device. *Nat Biotechnol*. 20(8):826-830, 2002

72. Lin-Gibson S, Landis FA, Drzal PL. Combinatorial investigation of the structure-properties characterization of photopolymerized dimethacrylate networks. *Biomaterials* 27(9):1711-1717, 2006

73. Livi CB, Davidson EH. Expression and function of blimp1/krox, an alternatively transcribed regulatory gene of the sea urchin endomesoderm network. *Dev Biol.* 293(2):513-525, 2006

74. Lo CM, Wang HB, Dembo M, Wang YL. Cell movement is guided by the rigidity of the substrate. *Biophys J.* 79(1):144-152, 2000

75. Lu HH, Jiang J. Interface tissue engineering and the formulation of multiple-tissue systems. *Adv Biochem Eng Biotechnol*. 102:91-111, 2006

76. Lundberg AS, Hahn WC, Gupta P, Weinberg RA. Genes involved in senescence and immortalization. *Curr Opin Cell Biol.* 12(6):705-709, 2000

77. Lutolf MP, Hubbell JA Synthetic biomaterials as instructive extracellular microenvironments for morphogenesis in tissue engineering, *Nat Biotechnol* 23 (1): 47–55, 2005

78. Lutolf MP, Gilbert PM, Blau HM. Designing materials to direct stem-cell fate. *Nature* 462(7272):433-441, 2009

79. Maherali N, Hochedlinger K. Guidelines and techniques for the generation of induced pluripotent stem cells. *Cell Stem Cell* 3(6):595-605, 2008

80. Malda J, Woodfield TB, van der Vloodt F, Kooy FK, Martens DE, Tramper J, van Blitterswijk CA, Riesle J. The effect of PEGT/PBT scaffold architecture on oxygen gradients in tissue engineered cartilaginous constructs. *Biomaterials* 25(26):5773-5780, 2004

81. Mao H, Cremer PS, Manson MD. A sensitive, versatile microfluidic assay for bacterial chemotaxis. *Proc Natl Acad Sci U S A.* 100(9):5449-5454, 2003

82. Martinez Arias A. Wnts as morphogens? The view from the wing of Drosophila. *Nat Rev Mol Cell Biol.* 4(4):321-325, 2003

83. Mei Y, Elliott JT, Smith JR, Langenbach KJ, Wu T, Xu C, Beers KL, Amis EJ, Henderson L. Gradient substrate assembly for quantifying cellular response to biomaterials. *J Biomed Mater Res A*. 79(4):974-988, 2006

84. Meyvantsson I, Warrick JW, Hayes S, Skoien A, Beebe DJ. Automated cell culture in high density tubeless microfluidic device arrays. *Lab Chip* 8(5):717-724, 2008

85. Mikos AG, Herring SW, Ochareon P, Elisseeff J, Lu HH, Kandel R, Schoen FJ, Toner M, Mooney D, Atala A, Van Dyke ME, Kaplan D, Vunjak-Novakovic G. Engineering complex tissues. *Tissue Eng.* 12(12):3307-3339, 2006

86. Minokawa T, Wikramanayake AH, Davidson EH. cis-Regulatory inputs of the wnt8 gene in the sea urchin endomesoderm network. *Dev Biol.* 288(2):545-558, 2005

87. Miura, M., Gronthos, S., Zhao, M., Lu, B., Fisher, L.W.,Robey, P.G., et al. SHED: stem cells from human exfoliated deciduous teeth. *Proc Natl Acad Sci USA* 100, 5807-5812, 2003

88. Moffat KL, Kwei AS, Spalazzi JP, Doty SB, Levine WN, Lu HH. Novel nanofiber-based scaffold for rotator cuff repair and augmentation. *Tissue Eng Part A*. 15(1):115-126, 2009

89. Moore K, MacSween M, Shoichet M. Immobilized concentration gradients of neurotrophic factors guide neurite outgrowth of primary neurons in macroporous scaffolds. *Tissue Eng.* 12(2):267-278, 2006

90. Narushima M. Kobayashi N. Okitsu T. Tanaka Y. Li S.A. Chen Y. Miki A. Tanaka K. Nakaji S. Takei K. Gutierrez A.S. Rivas-Carrillo J.D. Navarro-Alvarez N. Jun H.S. Westerman K.A. Noguchi H. Lakey J.R. Leboulch P. Tanaka N. Yoon J.W. A human beta-cell line for transplantation therapy to control type 1 diabetes. *Nat. Biotechnol.* 23:1274–1282, 2005

91. Nawata K, Minamizaki T, Yamashita Y, Teshima R. Development of the attachment zones in the rat anterior cruciate ligament: changes in the distributions of proliferating cells and fibrillar collagens during postnatal growth. *J Orthop Res.* 20(6):1339-1344, 2002

92. Noguchi H. Kobayashi N. Westerman K.A. Sakaguchi M. Okitsu T. Totsugawa T. Watanabe T. Matsumura T. Fujiwara T. Ueda T. Miyazaki M. Tanaka N.

Leboulch P. Controlled expansion of human endothelial cell populations by Cre–loxP-based reversible immortalization. *Hum. Gene Ther.* 13:321–334, 2002

93. Oh SH, Park IK, Kim JM, Lee JH. In vitro and in vivo characteristics of PCL scaffolds with pore size gradient fabricated by a centrifugation method. *Biomaterials* 28(9):1664-1671, 2007

94. Okitsu T.; Kobayashi N.; Jun H. S.; Shin S.; Kim S. J.; Han J.; Kwon H.; Sakaguchi M.; Totsugawa T.; Kohara M.; Westerman K. A.; Tanaka N.; Leboulch P.; Yoon J. W. Transplantation of reversibly immortalized insulin-secreting human hepatocytes controls diabetes in pancreatectomized pigs. *Diabetes* 53:105-112; 2004

95. Park JY*,* Kim SK*,* Woo DH*,* Lee EJ*.,* Kim JH*,* Lee SH. Differentiation of Neural Progenitor Cells in a Microfluidic Chip-Generated Cytokine Gradient. *Stem Cells* 27*,* 2646–2654, 2009

96. Pei, M., He, F., and Vunjak-Novakovic, G. Synoviumderived stem cell-based chondrogenesis. *Differentiation* 76, 1044-1056, 2008

97. Pelham RJ Jr, Wang Y. Cell locomotion and focal adhesions are regulated by substrate flexibility. *Proc Natl Acad Sci U S A*. 94(25):13661-3665, 1997

98. Phillips JE, Burns KL, Le Doux JM, Guldberg RE, García AJ. Engineering graded tissue interfaces. *Proc Natl Acad Sci U S A*. 105(34):12170-12175, 2008

99. Range RC, Venuti JM, McClay DR. LvGroucho and nuclear beta-catenin functionally compete for Tcf binding to influence activation of the endomesoderm gene regulatory network in the sea urchin embryo. *Dev Biol.* 279(1):252-267, 2005

100. Rodeo SA, Arnoczky SP, Torzilli PA, Hidaka C, Warren RF. Tendon-healing in a bone tunnel. A biomechanical and histological study in the dog. *J Bone Joint Surg Am.* 75(12):1795-803, 1993

101. Rosoff WJ, McAllister R, Esrick MA, Goodhill GJ, Urbach JS. Generating controlled molecular gradients in 3D gels. *Biotechnol Bioeng.* 91(6):754-759, 2005

102. Ruhe P.Q., Kroese-Deutman H. C., Wolke J. G., Spauwen P. H., Jansen J. A.. Bone inductive properties of rhBMP-2 loaded porous calcium phosphate cement implants in cranial defects in rabbits. *Biomaterials* 25, 2123-2132, 2004

103. Schier AF, Talbot WS. Molecular genetics of axis formation in zebrafish. *Annu Rev Genet.* 39:561-613, 2005

104. Schoenwolf GC. Cell movements driving neurulation in avian embryos. *Development* Suppl 2:157-168, 1991

105. Schoenwolf GC, Alvarez IS. Roles of neuroepithelial cell rearrangement and division in shaping of the avian neural plate. *Development* 106(3):427-439, 1989

106. Schultz L.B. Chehab N.H. Malikzay A. Halazonetis T.D. p53 binding protein 1 (53BP1) is an early participant in the cellular response to DNA double-strand breaks. *J. Cell Biol.* 151:1381–1390, 2000

107. Schwarz K. Epple M. Hierarchically structured polyglycolide—a biomaterial mimicking natural bone. *Macromol Rapid Commun*. 19:613-617, 1998

108. Segall JE. Polarization of yeast cells in spatial gradients of alpha mating factor. *Proc Natl Acad Sci U S A*. 90(18):8332-8336, 1993

109. Shay JW, Pereira-Smith OM, Wright WE. A role for both RB and p53 in the regulation of human cellular senescence. *Exp Cell Res.* 196(1):33-39, 1991

110. Shea LD, Smiley E, Bonadio J, Mooney DJ. DNA delivery from polymer matrices for tissue engineering. *Nat Biotechnol*. 17(6):551-554, 1999

111. Sherwood JK, Riley SL, Palazzolo R, Brown SC, Monkhouse DC, Coates M, Griffith LG, Landeen LK, Ratcliffe A. A three-dimensional osteochondral composite scaffold for articular cartilage repair. *Biomaterials* 23(24):4739-4751, 2002

112. Singh M, Berkland C, Detamore MS. Strategies and applications for incorporating physical and chemical signal gradients in tissue engineering. *Tissue Eng Part B Rev.* 14(4):341-66, 2008

113. Smith J, Theodoris C, Davidson EH. A gene regulatory network subcircuit drives a dynamic pattern of gene expression. *Science* 318(5851):794-797, 2007

114. Soldner F, Hockemeyer D, Beard C, Gao Q, Bell GW, Cook EG, Hargus G, Blak A, Cooper O, Mitalipova M, Isacson O, Jaenisch R. Parkinson's disease patient-derived induced pluripotent stem cells free of viral reprogramming factors. *Cell* 136(5):964-977, 2009

115. Spalazzi JP, Vyner MC, Jacobs MT, Moffat KL, Lu HH. Mechanoactive scaffold induces tendon remodeling and expression of fibrocartilage markers. *Clin Orthop Relat Res.* 466(8):1938-1948, 2008

116. Sternberg N., Hamilton D. Bacteriophage P1 site-specific recombination. I. Recombination between loxP sites. *J. Mol. Biol*. 150,467-486, 1981.

117. Tabata T, Takei Y. Morphogens, their identification and regulation. *Development* 131(4):703-712, 2004

118. Takahashi, K., and Yamanaka, S. Induction of pluripotent stem cells from mouse embryonic and adult fibroblast cultures by defined factors. Cell 126, 663, 2006.

119. Takahashi, K., Tanabe, K., Ohnuki, M., Narita, M., Ichisaka, T., Tomoda, K., and Yamanaka, S. Induction of pluripotent stem cells from adult human fibroblasts by defined factors. *Cell* 131, 861, 2007.

120. Tampieri A, Sandri M, Landi E, Pressato D, Francioli S, Quarto R, Martin I. Design of graded biomimetic osteochondral composite scaffolds. *Biomaterials* 29(26):3539-3546, 2008

121. Tourovskaia A, Li N, Folch A. Localized acetylcholine receptor clustering dynamics in response to microfluidic focal stimulation with agrin. *Biophys J.* 95(6):3009-3016, 2008

122. Vazin T, Schaffer DV. Engineering strategies to emulate the stem cell niche. *Trends Biotechnol.* 28(3):117-1124, 2010

123. Vepari CP, Kaplan DL. Covalently immobilized enzyme gradients within three-dimensional porous scaffolds. *Biotechnol Bioeng.* 93(6):1130-1137, 2006

124. Vlierberghe SV, Cnudde V, Dubruel P, Masschaele B, Cosijns A, Paepe ID, Jacobs PJ, Hoorebeke LV, Remon JP, Schacht E. Porous gelatin hydrogels:

Cryogenic formation and structure analysis. *Biomacromolecules* 8(2):331-337, 2007

125. Vunjak-Novakovic G, Kaplan DL. Tissue engineering: the next generation. *Tissue Eng.* 12(12):3261-3263, 2006
126. Walker GM, Sai J, Richmond A, Stremler M, Chung CY, Wikswo JP. Effects of flow and diffusion on chemotaxis studies in a microfabricated gradient generator. *Lab Chip* 5(6):611-8, 2005
127. Wang W, Lin C, Lu D, Ning Z, Cox T, Melvin D, Wang X, Bradley A, Liu P. Chromosomal transposition of PiggyBac in mouse embryonic stem cells. *Proc Natl Acad Sci U S A.* 105(27):9290-9295, 2008
128. Wei Y, Mikawa T. Formation of the avian primitive streak from spatially restricted blastoderm: evidence for polarized cell division in the elongating streak. *Development* 127(1):87-96, 2000
129. Westerman K.A. Leboulch P. Reversible immortalization of mammalian cells mediated by retroviral transfer and site-specific recombination. *Proc. Natl. Acad. Sci. U.S.A.* 93:8971–8976, 1996
130. Whitesides GM, Ostuni E, Takayama S, Jiang X, Ingber DE. Soft lithography in biology and biochemistry. *Annu Rev Biomed Eng.* 3:335-373, 2001
131. Whitesides GM. The origins and the future of microfluidics. *Nature* 442(7101):368-373, 2006
132. Woltjen K, Michael IP, Mohseni P, Desai R, Mileikovsky M, Hämäläinen R, Cowling R, Wang W, Liu P, Gertsenstein M, Kaji K, Sung HK, Nagy A. piggyBac transposition reprograms fibroblasts to induced pluripotent stem cells. *Nature* 458(7239):766-770, 2009
133. Woodfield TB, Van Blitterswijk CA, De Wijn J, Sims TJ, Hollander AP, Riesle J. Polymer scaffolds fabricated with pore-size gradients as a model for studying the zonal organization within tissue-engineered cartilage constructs. *Tissue Eng.* 11(9-10):1297-1311, 2005
134. Wu H, Huang B, Zare RN. Generation of complex, static solution gradients in microfluidic channels. *J Am Chem Soc*. 128(13):4194-4205, 2006
135. Yang, L., Soonpaa, M.H., Adler, E.D., Roepke, T.K., Kattman, S.J., Kennedy, M., et al. Human cardiovascular progenitor cells develop from a KDRþ embryonic-stem-cellderived population. *Nature* 453, 524-528, 2008
136. Yang S, Leong KF, Du Z, Chua CK. The design of scaffolds for use in tissue engineering. Part I. Traditional factors. *Tissue Eng*. 7(6):679-689, 2001
137. Yeung T, Georges PC, Flanagan LA, Marg B, Ortiz M, Funaki M, Zahir N, Ming W, Weaver V, Janmey PA. Effects of substrate stiffness on cell morphology, cytoskeletal structure, and adhesion. *Cell Motil Cytoskeleton* 60(1):24-34, 2005
138. Yusa K, Rad R, Takeda J, Bradley A. Generation of transgene-free induced pluripotent mouse stem cells by the piggyBac transposon. *Nat Methods* 6(5):363-369, 2009
139. Zhang, S., Wang, D., Estrov, Z., Raj, S., Willerson, J.T., and Yeh, E.T.H. Both cell fusion and transdifferentiation account for the transformation of human

peripheral blood CD34-positive cells into cardiomyocytes in vivo. *Circulation* 110, 3803-3807, 2004

140. Zhang Y, Nuglozeh E, Touré F, Schmidt AM, Vunjak-Novakovic G. Controllable expansion of primary cardiomyocytes by reversible immortalization. *Hum Gene Ther.* 20(12):1687-1696, 2009
141. Zheng JQ, Felder M, Connor JA, Poo MM. Turning of nerve growth cones induced by neurotransmitters. *Nature* 368(6467):140-144, 1994
142. Zhu J.; Wang H.; Bishop J. M.; Blackburn E. H. Telomerase extends the lifespan of virus-transformed human cells without net telomere lengthening. *Proc. Natl. Acad. Sci. USA.* 96:3723-3728; 1999
143. Zigmond SH. Ability of polymorphonuclear leukocytes to orient in gradients of chemotactic factors. *J Cell Biol.* 75: 606-616, 1977
144. Zmora S, Glicklis R, Cohen S. Tailoring the pore architecture in 3-D alginate scaffolds by controlling the freezing regime during fabrication. *Biomaterials* 23(20):4087-4094, 2002

Chapter 2 Regulation of cell proliferation - Controllable expansion of primary cardiomyocytes by reversible gene expression

2.1 Abstract

Cardiac tissue engineering will remain only a prospect unless large numbers of therapeutic cells can be provided, either from small samples of cardiac cells or from stem cell sources. In contrast to most adult cells, cardiomyocytes are terminally differentiated and cannot be expanded in culture. We explored the feasibility of enabling the *in vitro* expansion of primary neonatal rat cardiomyocytes by lentivector-mediated cell immortalization, and then reverting the phenotype of the expanded cells back to the cardiomyocyte state. Primary rat cardiomyocytes were transduced with simian virus 40 large T antigen (TAg), or with Bmi-1 followed by the human telomerase reverse transcriptase (hTERT) gene; the cells were expanded; and the transduced genes were removed by adenoviral vector expressing Cre recombinase. The TAg gene was more efficient in cell transduction than the Bmi-1/hTERT gene, based on the rate of cell proliferation. Immortalized cells exhibited the morphological features of dedifferentiation (increased vimentin expression, and reduced expression of troponin I and Nkx2.5) along with the continued expression of cardiac markers (α-actin, connexin-43, and calcium transients). After the immortalization was reversed, cells returned to their differentiated state. This strategy for controlled expansion of primary cardiomyocytes by gene transfer has potential for providing large amounts of a patient's own cardiomyocytes for cell therapy, and the

cardiomyocytes derived by this method could be a useful cellular model by which to study cardiogenesis.

2.2 Introduction

Myocardial infarction affects more than 500,000 patients in the United States each year (Kirkpatrick *et al.*, 2007), largely because of minimal endogenous cardiac regeneration that cannot compensate for the massive loss of cardiomyocytes after myocardial infarction. Tissue engineering of a functional cardiac patch is being studied as a potential way to replace damaged myocardium. However, engineering a clinically sized cardiac patch (centimeters in size, millimeters thick) requires large numbers of cells, because of the high cell density (~10^8 cells/cm^3) that needs to be established for functional cell coupling and signaling (Gerecht-Nir *et al.*, 2006).

A small fraction of adult heart cells has stem cell-like properties (Moretti *et al.*, 2006); however, it is difficult to isolate and expand these cells *in vitro*, because of their low frequency and limited access. Transplantation of exogenous adult and embryonic stem cells showed improved myocardial function by increasing vascularization and reducing ventricular remodeling (Orlic *et al.*, 2001; Kehat *et al.*, 2004). However, these cells may generate immunogenic or tumorigenic problems. Breakthroughs resulting in the derivation of induced pluripotent stem cells (iPS) by the introduction of four transcription factors (Oct3/4, Sox2, Klf4, and c-Myc) into adult cells represents a potential way to address this issue

(Takahashi and Yamanaka, 2006; Takahashi *et al.*, 2007), and may offer a source of autologous functional cardiomyocytes (Mauritz *et al.*, 2008; Narazaki *et al.*, 2008). It remains to be determined whether these cells have all the properties of embryonic stem cells, and how much phenotypic stabilization needs to be done *in vitro* to avoid the risk of teratoma formation.

A potential alternative approach is that of expanding nonproliferating primary cardiomyocytes, by step-wise immortalization that requires a combination of immortalization genes (Hahn *et al.*, 1999), followed by reversal into the terminally differentiated phenotype after the cells are expanded in culture. The process of reversible immortalization involves transfer and expression of specific immortalization genes in primary cells, and the subsequently removal of these genes by Cre–*loxP* site recombination. So far, reversible immortalization had been successfully applied to primary fibroblasts (Westerman and Leboulch 1996), human muscle satellite cells (Cudré-Mauroux *et al.*, 2003), human insulin secreting beta cells (Narushima *et al.*, 2005), and other types of cells (Kobayashi *et al.*, 2001; Noguchi *et al.*, 2002; Kowolik *et al.*, 2004; Hashimoto *et al.*, 2006). Here, we explore whether this method of gene transfer may be used to expand primary cardiac cells to numbers that are sufficient for basic research and regenerative medicine applications. We selected neonatal rat cardiomyocytes as model cells because they represent a widely used “standard” for cardiac tissue engineering studies. It has been established that neonatal rat cardiomyocytes undergo terminal differentiation stage during early neonatal myocardial growth,

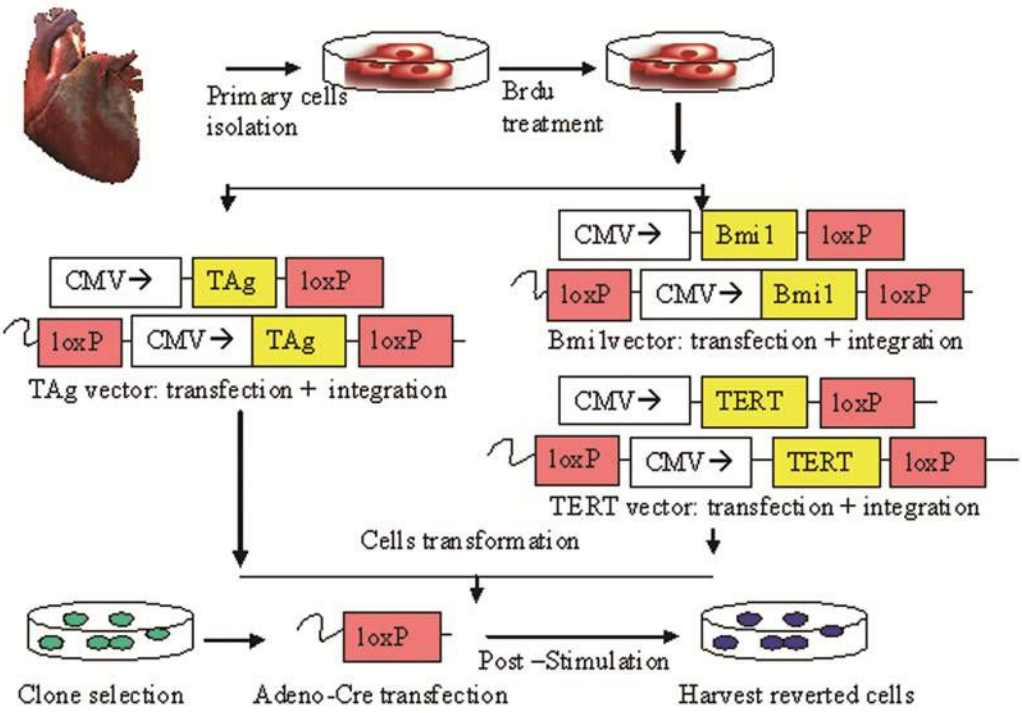

Figure 2.1 Experimental design for reversible immortalization of cardiac myocytes Freshly isolated neonatal rat cardiomyocytes were preplated for 1 hr and cultured in monolayer, using DMEM supplemented with bromodeoxyuridine (BrdU, 100 µ*M*) for 3–4 days to eliminate fibroblast contamination. The cells were then transduced either with lentiviral vector expressing simian virus 40 large T antigen (TAg) under the control of the cytomegalovirus (CMV) promoter, or with Bmi-1 vector and then human telomerase reverse transcriptase (hTERT) vector. The transformed cells were subjected to single cell cloning to yield TAg clone 8 or Bmi-1 clone 4. The cells were then infected with a recombinant adenovirus expressing Cre recombinase (Ad-CMV-Cre), to remove the TAg, Bmi-1, and hTERT genes that were flanked by *loxP* sites. Biophysical stimulation (100 µ*M* phenylephrine [PE], 10 µ*M* norepinephrine [NE], vascular endothelial growth factor [VEGF, 10 ng/ml], and dickkopf homolog-1 [DKK1, 150 ng/ml]) was applied to the reverted cells.

after which cellular proliferation no longer occurs (Simpson and Savion, 1982; Long *et al.*, 1990). For example, the 8-day culture of cell populations harvested from 1-day-old neonatal rat hearts resulted in a 6-fold increase in numbers of vascular cells and fibroblasts, and no increase in the number of cardiomyocytes (Long *et al.*, 1990). This is consistent with our experience in studies of cardiac tissue engineering using neonatal rat heart cells (Radisic *et al.* 2008). We studied

reversible immortalization of primary neonatal rat cardiomyocytes that were (1) immortalized by two different combinations of genes (simian virus 40 large T antigen [TAg], or Bmi-1/human telomerase reverse transcriptase [hTERT]), (2) expanded in culture, and (3) reversed back to cardiac phenotype (**Figure 2.1**).

2.3 Materails and Methods

2.3.1 Lentiviral vector production

loxP-containing human immunodeficiency virus (HIV)-derived lentiviral vectors expressing enhanced fluorescent green protein (GFP), TAg, Bmi-1, and hTERT from an internal human cytomegalovirus (CMV) immediate promoter (Salmon *et al.*, 2000) were obtained from Addgene (plasmids 12243, 12246, 12240, and 12245; Addgene, Cambridge, MA). The recombinant retroviruses were produced by established methods (Naghavi *et al.*, 2005). In brief, the lentiviral vector expressing the target gene, the lentiviral packaging construct (pCMVR8.91) encoding the HIV-1 Gag and Pol precursors, and the vesicular stomatitis virus (VSV) G envelope construct (pMD.G) (kindly provided by S. Goff, Department of Microbiology, Columbia University, NY) were cotransfected into 293T cells in the presence of FuGENE 6 (Roche, Basel, Switzerland). The culture fluid was harvested 48–72 hr posttransfection and stored at −80°C. The titer of recombinant viruses was $>5 \times 10^4$ transduction units/ml, as determined by flow cytometric analysis of 293T cells or diluted colonies, counting after selection in hypoxanthine–aminopterin–thymidine (HAT) medium (Sigma-Aldrich, St. Louis, MO).

2.3.2 Isolation, culture, and transduction of primary neonatal cardiomyocytes

Primary cultures of neonatal rat ventricular cardiomyocytes were derived according to previously published procedures (Radisic *et al.*, 2008). In brief, cardiomyocytes were obtained from 1- to 2-day-old neonatal Sprague-Dawley rats by means of a protocol approved by the committee on animal care at Columbia University (New York, NY). The ventricles were quartered, dissociated overnight at 4°C in a 0.06% (w/v) solution of trypsin in Hanks' balanced salt solution (HBSS; GIBCO, Grand Island, NY), washed in culture medium (Dulbecco's modified Eagle's medium [DMEM] supplemented with 10–20% fetal bovine serum [FBS], 10 m*M* HEPES, 2 m*M* L-glutamine, and penicillin–streptomycin [100 units/ml]; GIBCO), and then subjected to a series of digestions (8 min at 37°C; 75 rpm) in a 0.1% (w/v) solution of collagenase type II in HBSS. The harvested cells were then pooled and resuspended in culture medium. Cells were preplated for one 60-min period to enrich for cardiomyocytes. The cells were seeded at a density of 20×10^3 cells/cm^2 in 6-well plates. Bromodeoxyuridine (BrdU, 100 µ*M*; Sigma-Aldrich) was added to the growth medium for 3–4 days to eliminate proliferating fibroblast cells and progenitor cells (Lokuta *et al.*, 1994; Miragoli *et al.*, 2006).

For transduction, cardiomyocytes were exposed to lentiviral vectors at a multiplicity of infection (MOI) of 0.5–2 in the presence of Polybrene (10 µg/ml; Sigma-Aldrich) at 37°C for 6 hr (protocol adapted from Noguchi *et al.*, 2002; Naghavi *et al.*, 2005). For Bmi-1 and hTERT transduction, the infection was

repeated for 3–4 days. For single cell cloning, 1000 transduced cells were plated on a 100-mm culture dish coated with methylcellulose-based medium (R&D Systems, Minneapolis, MN). Colonies were isolated and expanded for experimentation.

2.3.3 Western blots

Cells were lysed in cell extraction buffer (Invitrogen, Carlsbad, CA). Total protein from lysate (15 μg per sample) was loaded for sodium dodecyl sulfate–polyacrylamide gel electrophoresis (SDS–PAGE) and the proteins were transferred to nitrocellulose membranes. Membranes were blocked in 10% milk and incubated with primary antibodies: mouse monoclonal antibodies against TAg and Bmi-1 (Santa Cruz Biotechnology, Santa Cruz, CA), and against TERT and glyceraldehydes-3-phosphate dehydrogenase (GAPDH) (Abcam, Cambridge, MA) at dilutions of 1:200–1:500, followed by secondary antibodies against mouse IgG conjugated with horseradish peroxidase (GE Healthcare, Buckinghamshire, UK). Signal was detected with enhanced chemiluminescence (ECL) reagent (GE Healthcare).

2.3.4 Cell growth kinetics

Primary heart cells isolated from neonatal rat were transduced with lentiviral vectors expressing TAg or Bmi-1/hTERT genes, and their growth kinetics were monitored by measuring the cell number in each of the first 6–8 passages of culture in the laboratory. The number of population doublings at each passage

was defined as log *N*/log 2, where *N* is the number of cells harvested at confluence divided by the number of cells initially seeded. Alternatively, DNA was measured with a PicoGreen dsDNA kit (Invitrogen) according to the manufacturer's protocol. The cytotoxicity of adenovirus was tested in a 3-(4, 5-dimethylthiazol-2-yl)-2,5-diphenyltetrazolium bromide (MTT) assay (Sigma-Aldrich).

2.3.5 Reversal to differentiated cell phenotype

Purified adenoviral vector expressing Cre recombinase under the control of the CMV promoter (Ad-CMV-Cre) (Vector Biolabs, Philadelphia, PA) was stored at −80°C at a titer of 2×10^7 transduction units/ml. TAg-transduced or Bmi-1/hTERT-transduced cells were infected with Ad-CMV-Cre at an MOI of 100–500 for 6–12 hr. The medium was then replaced with growth medium and the Cre-transduced cells were continuously cultured for another 4 days and passaged, to measure the proliferation capability of cells after Ad-CMV-Cre transduction. For further phenotype characterization experiments on the transduced cells after reversal, the cells were transduced by Ad-CMV-Cre at the required concentration (TAg clone 8, MOI: 300; Bmi-1/hTERT clone 4, MOI: 400) and were maintained in differentiation medium: DMEM–F12 containing penicillin–streptomycin (100 units/ml), 2 m*M* L-glutamine, 5% heat-inactivated FBS, insulin (10 µg/ml), transferrin (5.5 µg/ml), and sodium selenite (6.7 ng/ml) (Sigma-Aldrich) and further supplemented with 100 µ*M* phenylephrine (PE) and 10 µ*M* norepinephrine

(NE) (Sigma-Aldrich) or with vascular endothelial growth factor (VEGF, 10 ng/ml)/dickkopf homolog-1 (DKK1, 150 ng/ml; R&D Systems).

2.3.6 Immunofluorescence studies of marker expression

Cells were fixed in 4% paraformaldehyde for 20 min at room temperature, blocked with 10% horse serum (Vector Biolabs) for 40 min at room temperature, and then incubated for 1 hr at 37°C with primary antibodies: mouse anti-cardiac troponin I (diluted 1:150; Biodesign, Saco, ME), mouse anti-sarcomeric α-actin (diluted 1:150; Sigma-Aldrich), rabbit anti-connexin-43 (Cx-43, diluted 1:150; Chemicon, Temecula, CA), rabbit anti-vimentin (diluted 1:150; Chemicon), and rabbit anti-Nkx2.5 (diluted 1:50; Santa Cruz Biotechnology) in phosphate-buffered saline (PBS) containing 0.5% Tween 20 and 1.5% horse serum. Subsequently, the cells were incubated with secondary antibodies: Texas red-conjugated horse anti-IgG (diluted 1:200; Chemicon) and fluorescein-conjugated horse anti-mouse IgG (diluted 1:200; Chemicon). The nuclei were costained with 4′,6-diamidino-2-phenylindole (DAPI, diluted 1:1000; Vector Biolabs). The images were captured by fluorescence microscopy (IX81; Olympus, Tokyo, Japan) and the MetaMorph program (Molecular Devices, Downingtown, PA). The Matlab program CONNEXINMEASUREMENT, developed by our laboratory (Tandon *et al.*, 2009), was adapted to quantify the presence of Cx-43 protein. The number of instances of Cx-43 was measured in $n > 40$ sections per experimental group, and normalized by the cell number (measured by counting DAPI-stained nuclei in the same sections).

2.3.7 Calcium transients

The excitation–contraction coupling between cells was evaluated by measuring calcium transients. Briefly, cells were grown in 35-mm tissue culture dishes for 2–3 days until 70–80% confluent and loaded with 2 μ*M* Fluo-4 (Molecular Probes/Invitrogen, Carlsbad, CA) in PBS for 30 min at 37°C, washed with PBS, and incubated in growth medium for another 30 min to allow complete deesterification of intracellular acetoxymethyl ester (AM). Last, the cells were loaded with pulsing buffer containing 255 m*M* sucrose, 1 m*M* $CaCl_2$, 1 m*M* $MgCl_2$, and 5 m*M* HEPES (conductivity, 500 μS/cm). A pair of carbon electrodes (1/8-in. diameter, spaced 3.2 in. apart; Ladd Research Industries, Williston, VT) was connected to an electrical stimulator (Grass Technologies, West Warwick, RI) via a platinum wire (Ladd Research Industries) and placed in the tissue culture chamber. For excitation, field stimulation was applied at a frequency of 0.3–1 Hz, current pulses of 2 to 100 msec in duration, and a signal amplitude of 1–34.2 V/cm. Calcium transient images were acquired with a fluorescence microscope (IX81; Olympus), stored, and analyzed digitally with the ImageJ program (National Institutes of Health, Bethesda, MD). For each image, fluorescence intensity was integrated over the entire cell culture space and corrected by subtracting the background fluorescence measured for an area of the same size but without cultured cells.

2.4 Results

2.4.1 Lentivector-mediated conditional immortalization of primary cardiomyocytes

Cardiomyocytes isolated from neonatal rat left ventricles were treated with BrdU (100 µ*M*), a mitotic inhibitor, which binds to the newly synthesized DNA during the S phase of the cell cycle, substituting for thymidine during DNA replication. A high concentration of BrdU *in vitro* effectively blocked the proliferation of dividing cells (see **Supplementary Figure. 2.2**), including fibroblasts and progenitor cells, presumably because of activation of classical apoptosis pathways in BrdU-incorporating cells (Xia *et al.*, 1995; Caldwell *et al.*, 2005). After BrdU incorporation, the cardiac fibroblasts could not be passaged (Lokuta *et al.*, 1994; Miragoli *et al.*, 2006) or transduced by lentivirus-mediated TAg or Bmi-1/hTERT transfection. Likewise, we were not able to produce any clones from the BrdU-treated fibroblasts.

Approximately 10–20% of the purified cardiomyocytes exposed to lentiviral vector expressing GFP from the CMV promoter at an MOI of 2 were transduced (see **Supplementary Figure 2.1C**). By the same cell preparation protocol, DNAs encoding TAg, Bmi-1, hTERT were introduced by lentivector-mediated transduction into cardiomyocytes, either alone or in combinations. Insertion of the gene was confirmed by Western blot analysis of the expressed protein (**Figure 2.2**).

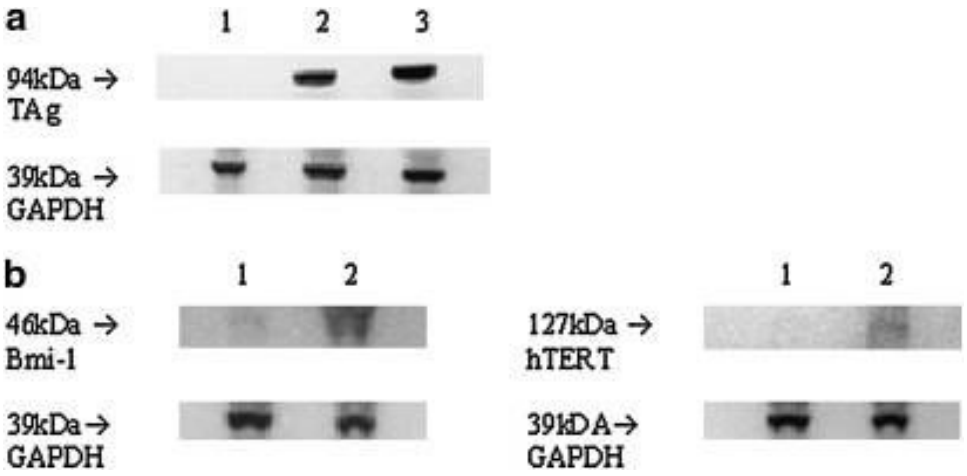

Figure 2.2 Western blot analysis of lentiviral vectors Expression of TAg and Bmi-1 followed by hTERT in infected cells was determined before and after Cre expression. **(A)** Lane 1, TAg clone 8 cells (passage 11) after Cre expression; lanes 2 and 3, TAg clone 8 cells before Cre expression (passage 11 and passage 3, respectively). **(B)** Lane 1, Bmi-1/hTERT clone 4 cells (passage 8) after Cre expression; lane 2, Bmi-1/hTERT clone 4 cells before Cre expression.

Cells quickly responded to TAg gene by increased cell proliferation, within 1–2 weeks of transduction. In contrast, cells transduced with Bmi-1/hTERT exhibited a significant delay before starting to form stabilized proliferative clones (**Figure 2.3**). The delay was probably due to the low Bmi-1-induced immortalization frequency (Hashimoto *et al.*, 2006) and slow cell proliferation rate in the single cell cloning process. Therefore, we repeatedly transduced cells with Bmi-1 vector (three or four times), followed by transduction of hTERT three or four times to increase the immortalization frequency (protocol adapted from Noguchi *et al.*, 2002; Kowolik *et al.*, 2004). Without hTERT transduction, Bmi-1-transformed cells undergo replicative senescence within five passages. With only hTERT, primary cardiomyocytes cannot be transduced, as evidenced by the lack of clone induction with up to five rounds of transfection in multiple experiments.

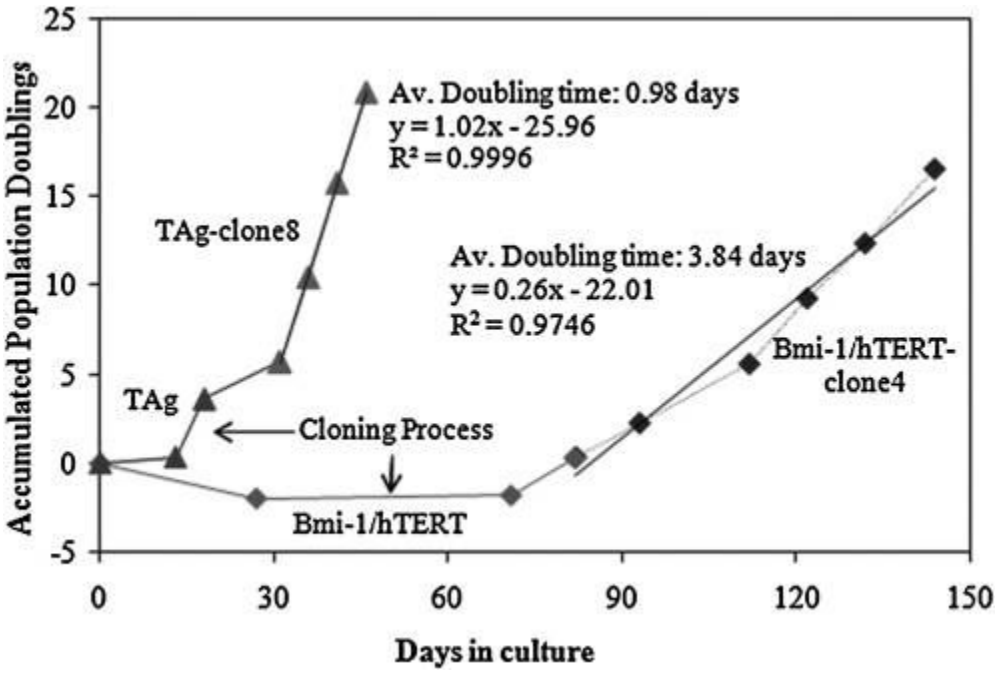

Figure 2.3 Proliferation of immortalized cardiomyocytes The proliferation of cardiac myocytes transduced with TAg or with Bmi-1/hTERT in the first six to eight passages of culture in the laboratory. Cell growth kinetics was monitored by measuring accumulated population doublings. Cell culture medium was DMEM supplemented with 10% FBS, 10 m*M* HEPES, 2 m*M* L-glutamine, and penicillin–streptomycin (100 U/ml).

The average doubling time of TAg-containing cells (TAg clone 8) was 0.98 days, whereas the average doubling time of Bmi-1/hTERT-containing cells (Bmi-1/hTERT clone 4) was 3.84 days (**Figure 2.3**). When cells were seeded at a higher density of 10^4 cells/cm^2 and cultured in growth medium containing 20% FBS, the doubling time fell to 2.5 days for Bmi-1/hTERT-transduced cells (Bmi-1/hTERT clone 4). TAg-transduced cells had more compact cell morphology, a lower tendency to align or flatten (**Figure 2.4**), and tended to form nodules, whereas Bmi-1/hTERT-transduced cells maintained contact inhibition and did not grow on top of each other.

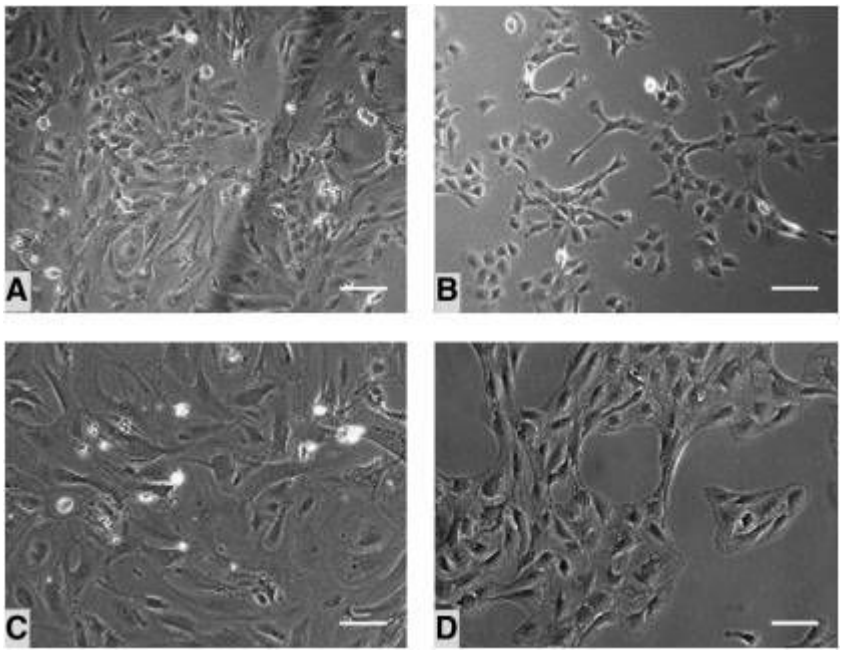

Figure 2.4 Cell morphology (A) TAg-transduced cells on day 7. **(B)** TAg clone 8 cells. **(C)** Bmi-1/hTERT-transduced cells on day 13. **(D)** Bmi-1/hTERT clone 4 cells. Cells immortalized with Bmi-1 and hTERT appeared large and elongated, whereas TAg-containing cells were smaller in size and more rounded in shape. Scale bars: 100 µm.

Remarkably, some of the Bmi-1/hTERT-transduced cells maintained contractile activity until passage 3 or 4. When the derived cells were seeded at low density onto methylcellulose-coated plates, they proliferated and formed well-defined colonies. In total, 28 clones of TAg-transduced cells and 7 clones of Bmi-1/hTERT-transduced cells were isolated. None of the colonies showed contractile activity beyond passage 3 or 4. We scanned all the clones on the basis of immunostaining (Cx-43, α-actin, and vimentin) and morphology, and then selected the best clones, TAg clone 8 and Bmi-1/hTERT clone 4, for in-depth analysis.

2.4.2 Reversal of cell immortalization after Cre recombinase expression

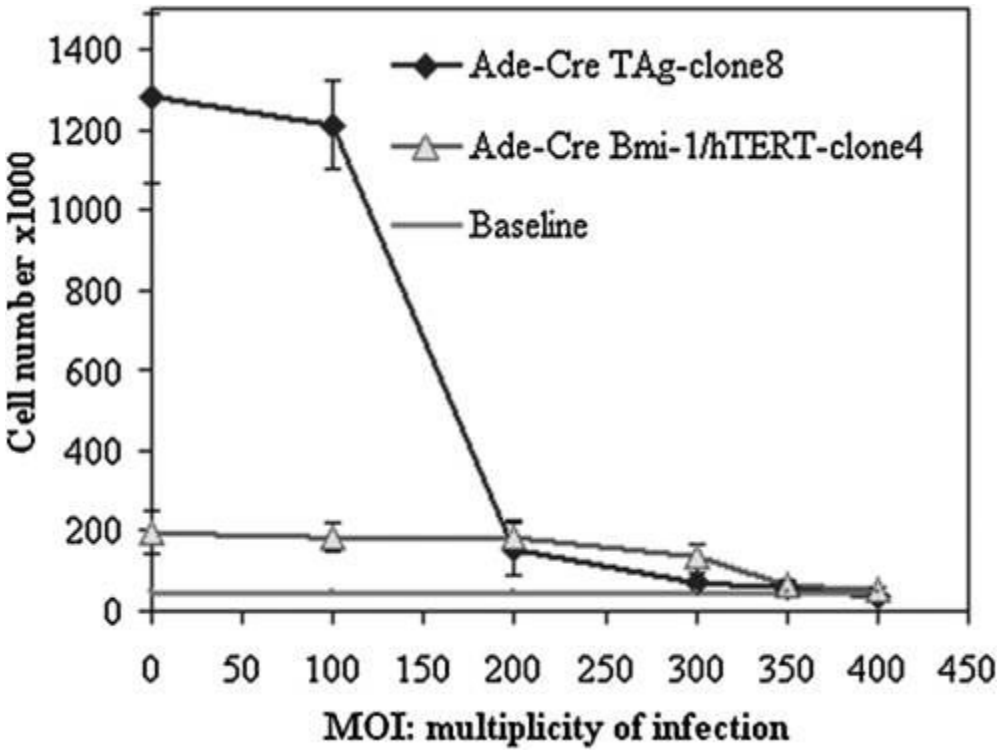

Figure 2.5 Effect of multiplicity of infection (MOI) on cell proliferation Cells were harvested, counted, and cultured 4 days after Cre transduction. Baseline: initial seeding cell number. After high-dose Cre transduction (MOI, 300 for TAg clone 8; MOI, 400 for Bmi-1/hTERT clone 4), the transfected cells stopped growing as confirmed by lack of proliferation in the next passage. Data are shown as averages ± SD ($n = 4$).

Both TAg- and Bmi-1/hTERT-transduced cells proliferated without apparent senescence for more than 6 months of culture. To totally reverse the immortalization by Cre–*loxP* site recombination, we tested the infection of the transduced cells with adenovirus expressing Cre recombinase (Ad-CMV-Cre) at various concentrations (MOI, 100–500). Only at a high concentration (TAg clone 8, MOI ≥ 300; Bmi-1/hTERT clone 4, MOI: 400) of Ad-CMV-Cre transduction did cell proliferation completely cease for the duration of the study (**Figure 2.5**). The high MOI adenovirus transduction was probably due to the limited expression of certain interaction receptors on the transduced cell surface, such as

coxsackievirus and adenovirus receptor (CAR) (Li *et al.,* 1999) and heparan sulfate proteoglycans (HSPGs) (Fender *et al.*, 2008). The removal of immortalization genes from the cellular genome was confirmed by Western blot (**Figure 2.2**). After 6 hr of incubation with adenoviral vector Ad-CMV-Cre, the bioactivity of control cells (nontransduced cells) was reduced by 12.30% (MOI, 300) or 35.71% (MOI, 400) by MTT measurement.

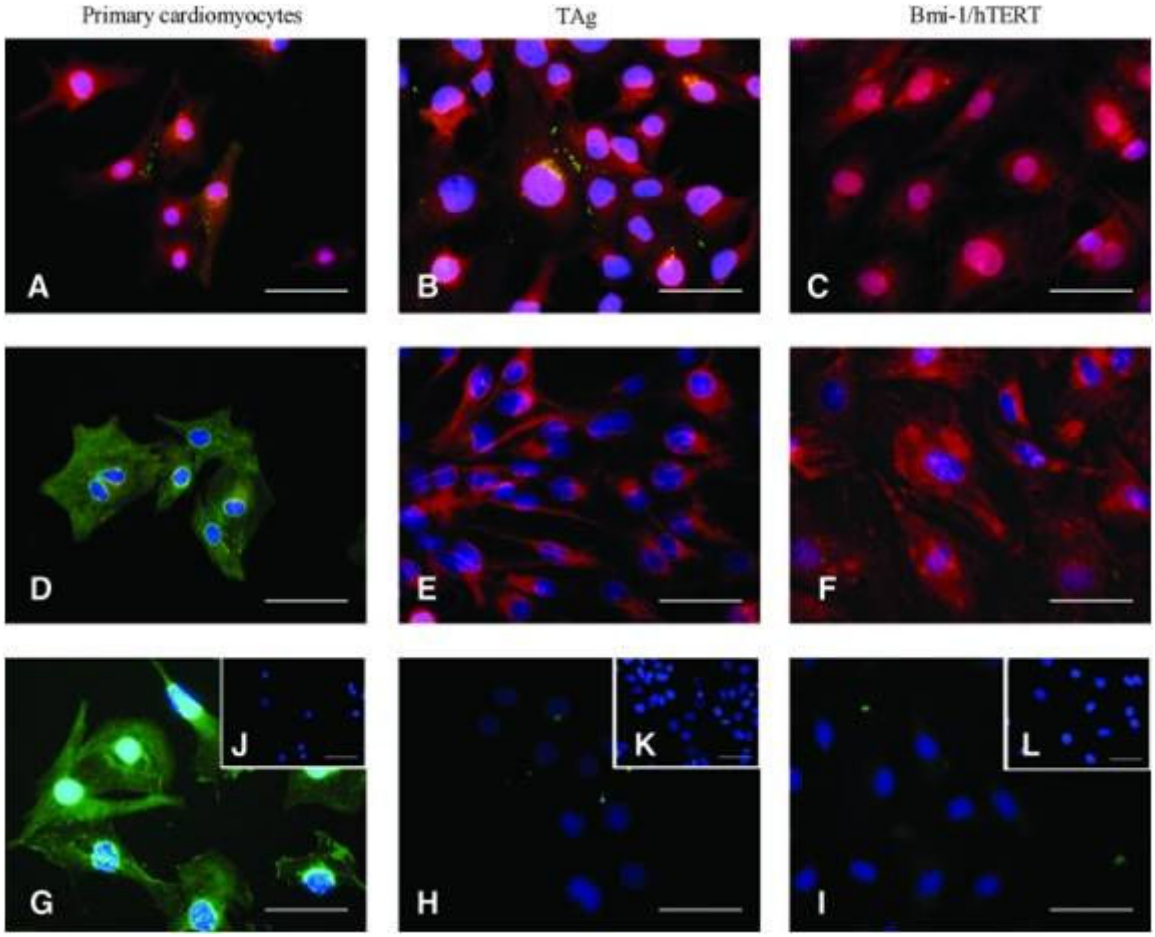

Figure 2.6 Phenotypic characterization of transduced cardiomyocytes (A–C) Cx-43 (FITC) and α-actin (Texas red) staining of **(A)** primary cardiomyocytes, **(B)** TAg clone 8 cells, and **(C)** Bmi-1/hTERT clone 4 cells. **(D–F)** Troponin (FITC) and vimentin (Texas red) staining of **(D)** primary cardiomyocytes, **(E)** TAg clone 8 cells and (**F**) Bmi-1/hTERT clone 4 cells. **(G–I)** Nkx2.5 (FITC) staining of **(G)** primary cardiomyocytes, **(H)** TAg clone 8 cells, and **(I)** Bmi-1/hTERT clone 4 cells. **(J–K)** Isotype controls for **(J)** primary cardiomyocytes, **(K)** TAg clone 8 cells, and **(L)** Bmi-1/hTERT clone 4 cells. Scale bars: 50 μm.

2.4.3 Phenotype characterization of transduced cells before and after reversal

Immunofluorescence analysis of transduced cells showed expression of α-actin, a prototypical Z-line protein in cardiomyocytes, and Cx-43, a connexin gap junction protein in cardiac muscles (**Figure 2.6**). TAg clone 8 cells exhibited normal patterns of Cx-43 expression in cell junctions, whereas Bmi-1/hTERT clone 4 cells did not exhibit these cardiac-specific patterns. Both clones had low expression of troponin I, a regulatory protein for cardiac muscle contraction; low expression of Nkx2.5, a transcription factor related to cardiac differentiation; and high expression of vimentin, which was consistent with the dedifferentiation of cells during transformation (LaFramboise *et al.*, 2007; Nakamura *et al.*, 2008). Both clones maintained Cx-43 and α-actin expression; however, only TAg clone 8 exhibited localized Cx-43 expression in cell–cell junctions.

We tested a group of biochemical simulation factors including 100 μ*M* PE and 10 μ*M* NE, and growth factors including VEGF (10 ng/ml) and DKK1 (150 ng/ml), on postexpansion differentiation. Cx-43 quantification, using a Matlab program (Tandon *et al.*, 2009), showed that the frequency of Cx-43 in primary cardiomyocytes (2.87 per cell) decreased after TAg-induced transformation (to 1.52 per cell) and then increased again after Cre recombinase reversion (to 1.62 per cell) as well as after stimulation with PE (to 1.72 per cell) and growth factors DKK1 and VEGF (to 2 per cell). Growth factor stimulation and NE also led to increases in α-actin and Cx-43 in Bmi-1/hTERT-transduced cells after reversion

(**Figure 2.7**); however, these stimulations still could not generate well-developed cardiac-specific patterned Cx-43.

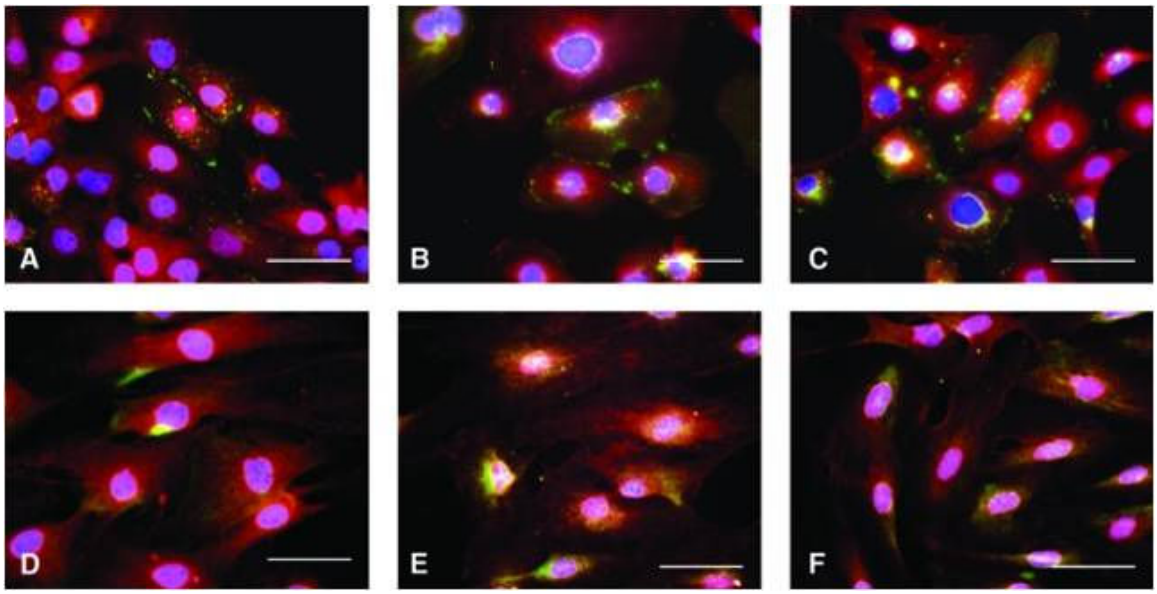

Figure 2.7 Phenotypic characterization of reverted clones after Cre transduction (A–C) Cx-43 (FITC) and α-actin (Texas red) staining of TAg clone 8 cells after Cre transduction **(A)** TAg clone 8 cells after Cre transduction and PE stimulation **(B)** and TAg clone 8 cells after Cre transduction and GF stimulation **(C)**. **(D–F)** Cx-43 (FITC) and α-actin (Texas red) staining of Bmi-1/hTERT clone 4 cells after Cre transduction **(D)** Bmi-1/hTERT clone 4 cells after Cre transduction and NE stimulation **(E)** and Bmi-1/hTERT clone 4 cells after Cre transduction and GF stimulation **(F)**. PE, phenylephrine (100 μ*M*); NE, norepinephrine (10 μ*M*); GF, VEGF (10 ng/ml) and DKK1 (150 ng/ml). Scale bars: 50 μm.

2.4.4 Spontaneous and induced calcium transients in immortalized cells

Primary cardiomyocytes exhibited spontaneous contractions associated with calcium transients, with the fastest transient rate observed at a frequency of 2 Hz, which is in the physiologic range for rats (**Figure 2.8A**). When contractile function was induced by electrical stimulation, primary cardiomyocytes showed excitable calcium transients in a relatively lower electrical field (20 V/cm) and short pulse duration (2 msec), with capture rates of up to 1 Hz.

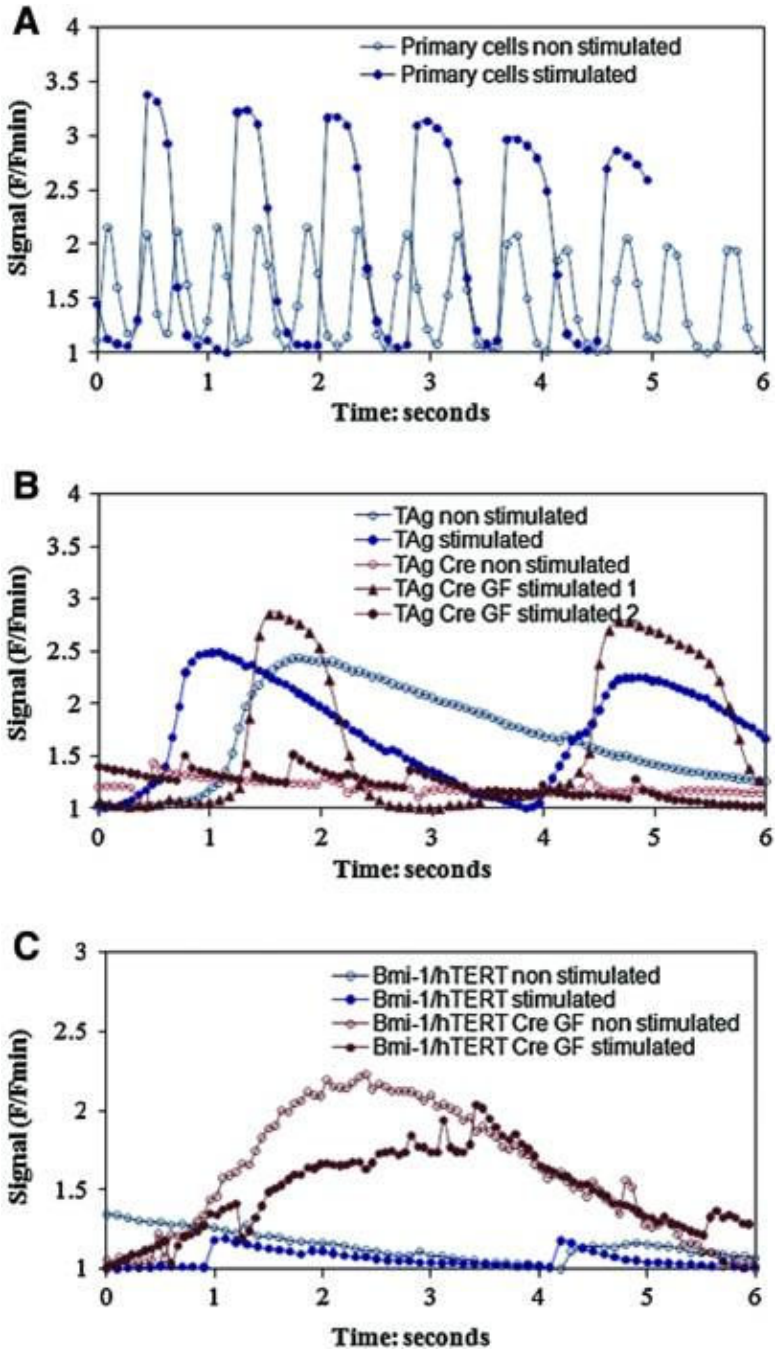

Figure 2.8 Calcium transients in primary cardiomyocytes and transduced cells **(A)** Spontaneous and paced calcium transient in primary cells (stimulation: 20 V/cm, 1 Hz, 2-msec duration). **(B)** Spontaneous and paced calcium transient in TAg clone 8 cells before and after Cre expression with growth factor treatment. (Before Cre expression, stimulation: 34.2 V/cm, 0.3 Hz, 100-msec duration; After Cre expression and growth factor treatment, stimulation 1: 34.2 V/cm, 0.3 Hz, 100-msec duration; stimulation 2: 34.2 V/cm, 1 Hz, 2-msec duration). **(C)** Spontaneous and paced calcium transient in Bmi-1/hTERT clone 4 cells before and after Cre expression with growth factor treatment (stimulation: 34.2 V/cm, 0.3 Hz, 100-msec duration).

TAg clone 8 cells also exhibit spontaneous calcium transients at much lower frequency (<0.2 Hz), and they could only be excited at lower frequency (0.3 Hz) with a higher electrical field (34.2 V/cm) and longer pulse duration (100 msec) (**Figure 2.8B**). Bmi-1/hTERT clone 4 cells were quiescent and did not undergo any apparent changes in calcium content, when given the same stimulation as TAg clone 8 cells (**Figure 2.8C**).

After Cre transduction, the reverted TAg-transduced cells showed increased spontaneous calcium transients at a frequency of 1 Hz (VEGF and DKK1 treatment; **Figure 2.8B**) or ~0.25 Hz (NE, PE, or Cre only; see **Supplementary Figure 2.3E, G, and C**). With electrical stimulation at 34.2 V/cm and a pulse duration of 100 msec, all reverted TAg-transduced cells could be excited except for the nontreatment group (**Supplementary Figure 2.3C, E, G, and I**). After VEGF and DKK1 treatment, reverted TAg-transduced cells exhibited an increased excitable calcium response frequency up to 1 Hz, suggesting enhanced cell excitability after removing the TAg gene and growth factor stimulation (**Supplementary Figure 2.3I**). In contrast, after removing the Bmi-1/hTERT gene, these effects were not seen—the cells exhibited enhanced spontaneous transients (<0.2 Hz) and increased amplitude of calcium changes, but could not respond to electrical stimulation. After VEGF and DKK1, PE, or NE treatment, reverted Bmi-1/hTERT-transduced cells exhibited enhanced spontaneous transients (<0.2 Hz), and an increased amplitude of calcium

changes; however, the cells did not show paced transients in response to electrical stimulation (**Supplementary Figure 2.3D, F, H, and J**).

2.5 Discussion

Our experiments show that reversible immortalization has the potential to generate large numbers of patient-specific cells for cardiac tissue engineering. First, we proved lentiviral vectors were efficient in introducing genes into primary cardiomyocytes; approximately 10–20% of the purified primary cardiomyocytes could be infected with lentiviral vector at an MOI of 2. The high transduction efficiency of lentiviral vector was the result of their ability to mediate stable integration and long-term expression of transgenes in a wide variety of targets irrespective of their proliferative status (Salmon *et al.*, 2000). However, potential insertional mutagenesis may occur through the random integration of inserted lentiviral vectors; site-specific insertion by adeno-associated virus (AAV)-mediated transduction may be a promising option for future work.

We compared the application of two frequently used immortalizing genes (Cudré-Mauroux *et al.*, 2003): TAg, which acts through the binding of retinoblastoma protein (Rb) and p53 (Ali and DeCaprio, 2001), and Bmi-1, which downregulates the p16 and $p19^{Arf}$ tumor suppressor genes encoded by the *ink4a* locus (Jacobs *et al.*, 1999), and is often combined with human telomerase (hTERT) (Hashimoto *et al.*, 2006). Lentivector-mediated transduction of TAg alone, or of Bmi-1/hTERT, resulted in the immortalization of primary neonatal rat cardiomyocytes such that

they acquired the ability to proliferate over prolonged periods of time (up to 6 months of continuous culture during our studies). In contrast, Bmi-1 alone was not able to sustain continuous cell growth. Consistently, the cell phenotypes associated with the transduction of these two sets of immortalization genes were distinctly different. The TAg gene was expressed at high levels, and induced fast cell proliferation without a lag phase, which led to cells arranged in colonies and round in shape, aggregating and growing without contact inhibition in most clones. In contrast, Bmi-1/hTERT transduction delayed cell proliferation, which occurred at a much slower rate, and Bmi-1/hTERT-transduced cells exhibited more extended cell morphology, and maintained the contact inhibition growth pattern in all clones, which was possibly due to the low levels of gene expression. The method established in this study enabled us to start with a small number of primary cells (<600,000), transform the cells, and derive stable TAg-transduced clones within approximately 3 weeks. The method could potentially be used to derive large numbers of repair cells from a small biopsy sample.

Interestingly, certain phenotype characteristics of primary cardiomyocytes (expression of α-actin, patterned Cx-43, and spontaneous and induced calcium transients) were conserved through multiple generations of TAg-transduced cells. In particular, the excitation–contraction coupling measured as calcium transients showed that the sarcoplasmic reticulum of TAg clone 8 cells was still able to release calcium in response to electrical stimulation. The lack of response to electrical stimulation at higher frequencies may be attributed to delayed

restoration of excitability, because intracellular calcium in these cells may return to the basal level more slowly than in primary cardiomyocytes. The presence of cardiac-specific features in Bmi-1/hTERT-transduced cells was less evident than in TAg-transduced cells (the expression of α-actin was conserved, but Cx-43 patterning and calcium responses were not).

After adenovirus-mediated Cre recombinase expression, which spliced the inserted genes, we noticed a complete arrest of cell proliferation and increased expression of Cx-43 in TAg-transduced cells. To redifferentiate cardiac phenotypes in those reverted cells, we tested a group of biochemical stimulatory molecules including PE, NE, VEGF, and DKK1. PE and NE are pharmacologic agents, used in clinics to elicit varied effects on vascular resistance, myocardial contractility, and heart rate (Coons and Seidl, 2007). Cellular studies showed that PE or NE could further induce sarcomere formation in some transformed cardiac cells (Rybkin *et al.*, 2003). In our studies, the supplementation of culture medium with PE or NE enhanced the expression of α-actin as well as Cx-43 in reverted cells. VEGF and DKK1 are growth factors used in the cardiovascular differentiation of embryonic stem cells, through stage-specific inhibition of Wnt signaling (Yang *et al.*, 2008). VEGF and DKK1 enhanced the expression of α-actin and Cx-43 in both TAg-transduced and Bmi-1/hTERT-transduced cells after reversion. Stimulation with VEGF and DKK1 also increased the calcium transient frequency in reverted TAg-transduced cells, suggesting improved capacity of the cells for electrical communication.

Our findings are consistent with the previous findings that Wnt signaling and VEGF are important modulators of Cx-43 expression in cardiomyocytes (Ai *et al.*, 2000; Yamada *et al.*, 2005). Because inappropriate expression of Wnt signaling had been found in a variety of cell transformations (Smalley and Dale, 1999), we hypothesized that Wnt signaling was triggered during cell immortalization, causing the loss of some properties of the cardiac phenotype, such as the decrease in Cx-43. Therefore, modulation of Wnt signaling with growth factors may present a method to redifferentiate the cardiac phenotype after reversion. Taken together, these data suggest that the immortalization of terminally differentiated cardiac myocytes could have practical value. Further phenotypic analysis of the cells *in vivo* should be included for future study, in order to better characterize the functional value of the reversible immortalization of cardiomyocytes.

This study shares some similarities with studies of reprogrammed (iPS) cells (Mauritz *et al.*, 2008; Narazaki *et al.*, 2008). Both strategies use lentivirus-based gene transduction to induce adult primary cells into dedifferentiated proliferating status, and apply growth factors to redifferentiate the expanded cells into specific lineages. Notably, when reversible immortalization is used, the expanded cells are depleted of the inserted genes via *loxP*–Cre recombination. As a result of complete gene splicing, cell proliferation was completely arrested, enabling the elimination of potential tumorigenic problems in transplantation practice.

The iPS research suggested various strategies of gene transfer toward deriving fully functional, mature cell phenotypes. The TAg gene interacts with cell cycling-related factors, such as p53 (Schultz *et al.*, 2000), which induces cell proliferation, but is also involved in the control of DNA repair and recombination. In iPS studies, differentiated cell phenotypes are derived through a series of steps starting with early cell differentiation. In studies of reversible immortalization, the process is being shortened by picking the most “promising” clones that express specific key phenotypes and by regaining the lost cell phenotypes by proper stimulation after gene splicing. This “shortcut” strategy worked well with many cell types, such as human insulin-secreting beta cells (Narushima *et al.*, 2005). If, however, the full phenotypic characteristics of cardiomyocytes are not restored (in particular, the contractile function), we may need to implement some of the strategies used to derive iPS cells.

2.6 Conclusion

In summary, the strategy for controlled expansion of primary cardiomyocytes by gene transfer has the potential to provide large amounts of a patient's own cardiomyocytes for cell therapy. Further studies are needed to determine whether the phenotypic properties of reversed cells are sufficient for cell therapy of the heart. In turn, because of the partial expression of the cardiac phenotype, these cells could serve as an interesting model for studies of cardiac differentiation.

2.7 Supplemental Information

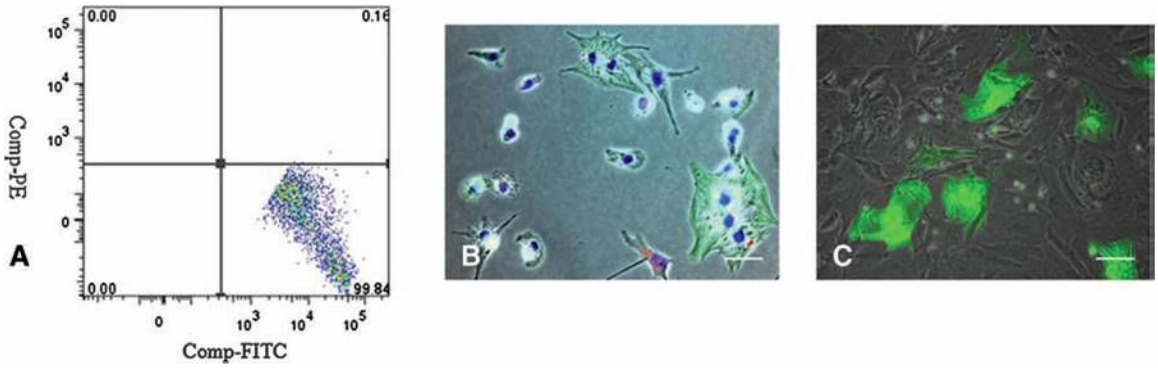

Supplemental figure 2.1 Purification and transduction of primary cardiomyocytes (A) FACS data. **(B)** Immunofluorescence of primary cardiomyocytes after preplating and BrdU treatment, showing that most cells were troponin (FITC) positive and vimentin (PE or Texas red) negative. **(C)** Primary cardiomyocytes transduced with lentiviral vector expressing GFP (MOI, 2). Scale bar: 50 mm.

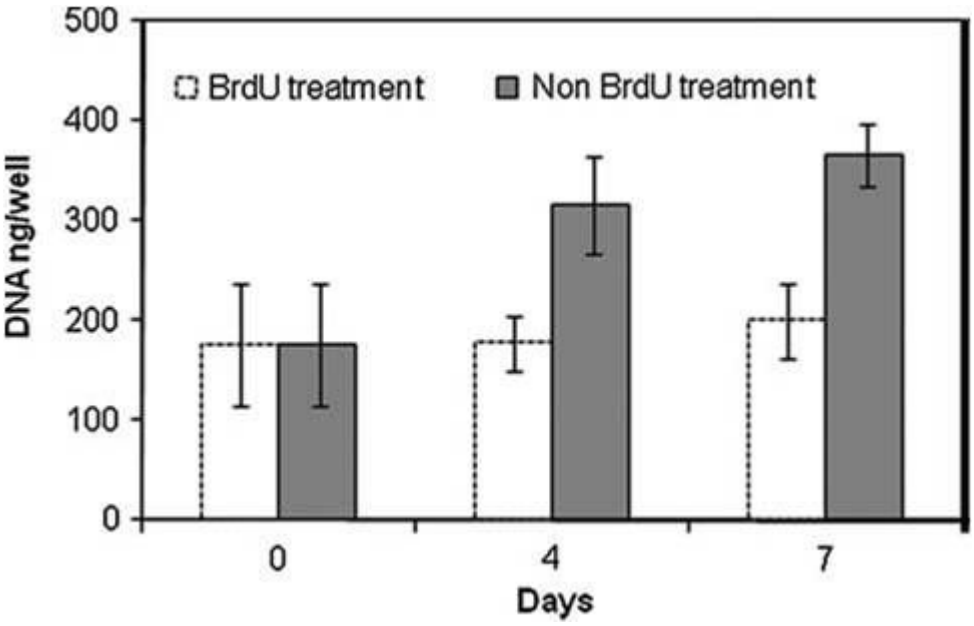

Supplemental figure 2.2 Proliferation of primary neonatal cardiomyocytes with BrdU or without BrdU treatment (100 mM). Cell growth kinetics was monitored by measuring total DNA quantification. Cell culture medium was DMEM supplemented with 10% FBS, 10mM HEPES, 2mM L-glutamine, and penicillin–streptomycin (100U/ml).

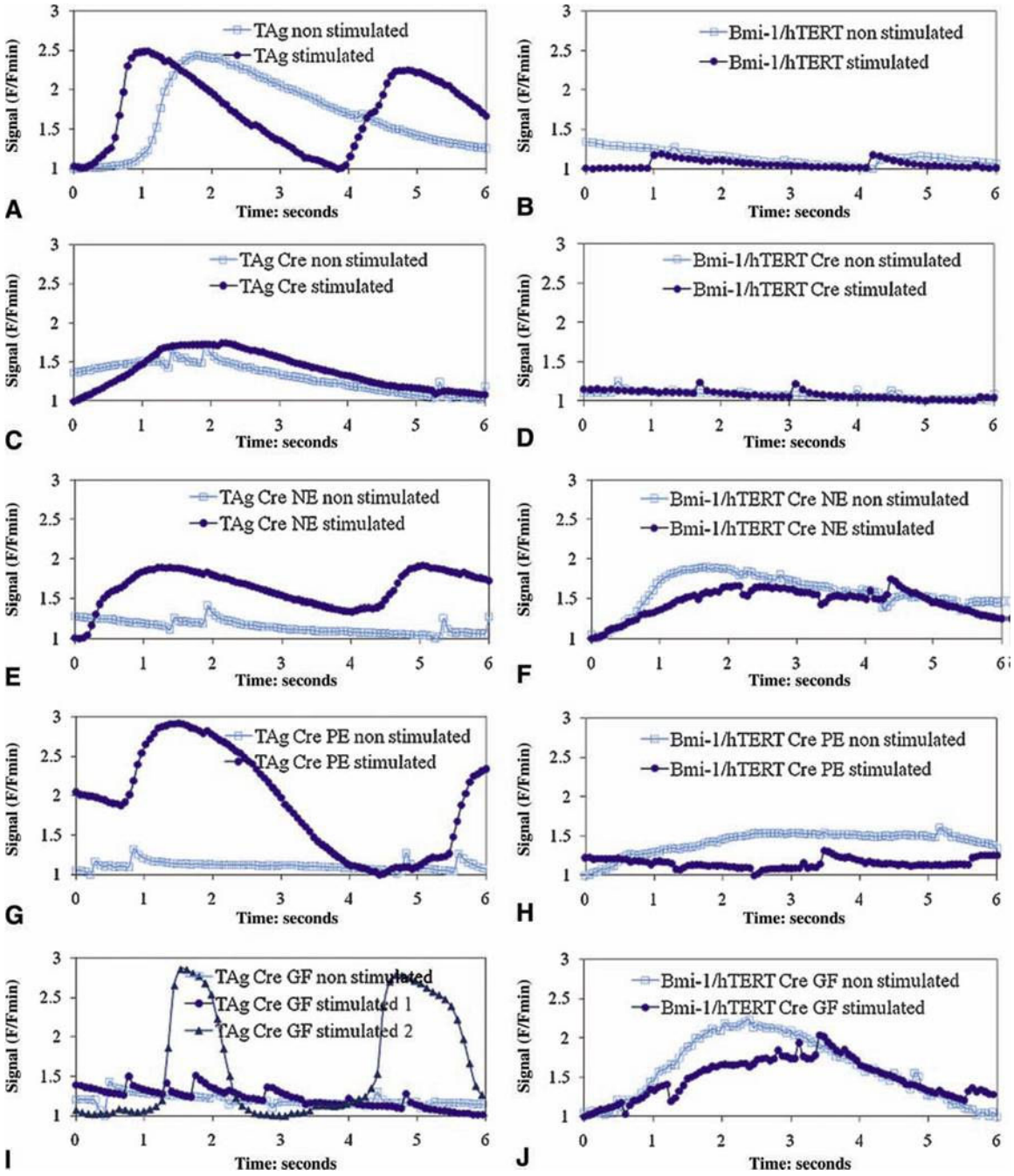

Supplemental figure 2.3 Calcium transient in TAg clone 8 and Bmi-1=hTERT clone 4 Spontaneous and paced calcium transient (stimulation: 34.2V/cm, 0.3 Hz, 100 ms duration; stimulation 2: 34.2V/cm, 1 Hz, 2 ms duration) in TAg clone 8 before **(A)** and after Cre expression **(C)**, with NE **(E)**, PE **(G)** or GF treatment **(I)**. Spontaneous and paced calcium transient (stimulation: 34.2V/cm, 0.3 Hz, 100 ms duration) in Bmi-1/hTERT clone 4 before **(B)** and after Cre expression **(D)**, with NE **(F)**, PE **(H)** or growth factor treatment **(J)**. PE: phenylephrine 100 mM; NE: norepinephrine 10 mM; GF: 10 ng/ml VEGF, 150 ng/ml DKK1.

2.8 References

1. Ai Z, Fischer A, Spray DC, Brown AM, Fishman GI. Wnt-1 regulation of connexin43 in cardiac myocytes. *J. Clin. Invest*. 105:161–171, 2000
2. Ali SH, DeCaprio JA. Cellular transformation by SV40 large T antigen: Interaction with host proteins. *Semin. Cancer Biol.* 11:15–23, 2001
3. Caldwell MA, He X, Svendsen CN. 5-Bromo-2′-deoxyuridine is selectively toxic to neuronal precursors in vitro. *Eur. J. Neurosci.* 22:2965–2970, 2005
4. Coons JC, Seidl E. Cardiovascular pharmacotherapy update for the intensive care unit. *Crit. Care Nurs. Q.* 30:44–57, 2007
5. Cudré-Mauroux C, Occhiodoro T, Knig S, Salmon P, Bernheim L, Trono D. Lentivector-mediated transfer of Bmi-1 and telomerase in muscle satellite cells yields a Duchenne myoblast cell line with long-term genotypic and phenotypic stability. *Hum. Gene Ther.* 14:1525–1533, 2003
6. Fender P, Schoehn G, Perron-Sierra F, Tucker GC, Lortat-Jacob H. Adenovirus dodecahedron cell attachment and entry are mediated by heparan sulfate and integrins and vary along the cell cycle. *Virology.* 371:155–164, 2008
7. Gerecht-Nir S, Radisic M, Park H, Cannizzaro C, Boublik J, Langer R, Vunjak-Novakovic G. Biophysical regulation during cardiac development and application to tissue engineering. *Int. J. Dev. Biol.* 50:233–243, 2006
8. Hahn WC, Counter CM, Lundberg AS, Beijersbergen RL, Brooks MW, Weinberg RA. Creation of human tumour cells with defined genetic elements. *Nature.* 400:464–468, 1999
9. Hashimoto N, Kiyono T, Wada MR, Shimizu S, Yasumoto S, Inagawa M. Immortalization of human myogenic progenitor cell clone retaining multipotentiality. *Biochem. Biophys. Res. Commun.* 348:1383–1388, 2006
10. Jacobs JJ, Kieboom K, Marino S, DePinho RA, van Lohuizen M. The oncogene and Polycomb-group gene bmi-1 regulates cell proliferation and senescence through the ink4a locus. *Nature.* 397:164–168, 1999
11. Kehat I, Khimovich L Caspi O, Gepstein A, Shofti R, Arbel G, Huber I, Satin J, Itskovitz-Eldor J, Gepstein L. Electromechanical integration of cardiomyocytes derived from human embryonic stem cells. *Nat. Biotechnol.* 22:1282–1289, 2004
12. Kirkpatrick JN, Vannan MA, Narula J, Lang RM. Echocardiography in heart failure: Applications, utility, and new horizons. *J. Am. Coll. Cardiol.* 50:381–396, 2007
13. Kobayashi N, Noguchi H,. Westerman KA, Watanabe T, Matsumura T, Totsugawa T, Fujiwara T, Leboulch P, Tanaka N. Cre/loxP-based reversible immortalization of human hepatocytes. *Cell Transplant.* 10:383–386, 2001
14. Kowolik CM, Liang S, Yu Y, Yee JK. Cre-mediated reversible immortalization of human renal proximal tubular epithelial cells. *Oncogene.* 23:5950–5957, 2004
15. LaFramboise WA, Scalise D, Stoodley P, Graner SR, Guthrie RD, Magovern JA, Becich MJ. Cardiac fibroblasts influence cardiomyocyte phenotype in vitro. *Am. J. Physiol. Cell Physiol.* 292:C1799–C1808, 2007

16. Li Y, Pong RC, Bergelson JM, Hall MC, Sagalowsky AI, Tseng CP, Wang Z, Hsieh JT. Loss of adenoviral receptor expression in human bladder cancer cells: A potential impact on the efficacy of gene therapy. *Cancer Res.* 59:325–330, 1999

17. Lokuta A, Kirby MS, Gaa ST, Lederer WJ, Rogers TB. On establishing primary cultures of neonatal rat ventricular myocytes for analysis over long periods. *J. Cardiovasc. Electrophysiol.* 5:50–62, 1994

18. Long CS, Kariya K, Karns L, Simpson PC. Trophic factors for cardiac myocytes. *J. Hypertens. Suppl.* 8:S219–S224, 1990

19. Mauritz C, Schwanke K, Reppel M, Neef S, Katsirntaki K, Maier LS, Nguemo F, Menke S, Haustein M, Hescheler J, Hasenfuss G, Martin U. Generation of functional murine cardiac myocytes from induced pluripotent stem cells. *Circulation.* 118:507–517, 2008

20. Miragoli M, Gaudesius G, Rohr S. Electrotonic modulation of cardiac impulse conduction by myofibroblasts. *Circ. Res.* 98:801–810, 2006

21. Moretti A, Caron L, Nakano A, Lam JT, Bernshausen A, Chen Y, Qyang Y, Bu L, Sasaki M, Martin-Puig S, Sun Y, Evans SM, Laugwitz KL, Chien KR. Multipotent embryonic isl1+ progenitor cells lead to cardiac, smooth muscle, and endothelial cell diversification. *Cell.* 127:1151–1165, 2006

22. Naghavi MH, Hatziioannou T, Gao G, Goff SP. Overexpression of fasciculation and elongation protein ζ-1 (FEZ1) induces a post-entry block to retroviruses in cultured cells. *Genes Dev.* 19:1105–1115, 2005

23. Nakamura T, Feng Z, Honda T, Nomura Y, Kitajima T, Umezu M. Comparison of mRNA expression of transcriptional factors and intercalated disk constituent proteins between in vivo and cultured cardiomyocytes. *J. Artif. Organs.* 11:134–140, 2008

24. Narazaki G, Uosaki H, Teranishi M, Okita K, Kim B, Matsuoka S, Yamanaka S, Yamashita JK. Directed and systematic differentiation of cardiovascular cells from mouse induced pluripotent stem cells. *Circulation.* 118:498–506, 2008

25. Narushima M, Kobayashi N, Okitsu T, Tanaka Y, Li SA, Chen Y, Miki A, Tanaka K, Nakaji S, Takei K, Gutierrez AS, Rivas-Carrillo JD, Navarro-Alvarez N, Jun HS, Westerman KA, Noguchi H, Lakey JR, Leboulch P, Tanaka N, Yoon JW. A human beta-cell line for transplantation therapy to control type 1 diabetes. *Nat. Biotechnol.* 23:1274–1282, 2005

26. Noguchi H, Kobayashi N, Westerman KA, Sakaguchi M, Okitsu T, Totsugawa T, Watanabe T, Matsumura T, Fujiwara T, Ueda T, Miyazaki M, Tanaka N, Leboulch P. Controlled expansion of human endothelial cell populations by Cre–loxP-based reversible immortalization. *Hum. Gene Ther.* 13:321–334, 2002

27. Orlic D, Kajstura J, Chimenti S, Jakoniuk I, Anderson SM, Li B, Pickel J, McKay R, Nadal-Ginard B, Bodine DM, Leri A, Anversa P. Bone marrow cells regenerate infarcted myocardium. *Nature.* 410:701–705, 2001

28. Radisic M, Marsano A, Maidhof R, Wang Y, Vunjak-Novakovic G. Cardiac tissue engineering using perfusion bioreactor systems. *Nat. Protoc.* 3:719–738, 2008

29. Rybkin II, Markham DW, Yan Z, Bassel-Duby R, Williams RS, Olson EN. Conditional expression of SV40 T-antigen in mouse cardiomyocytes facilitates an

inducible switch from proliferation to differentiation. *J. Biol. Chem.* 278:15927–15934, 2003

30. Salmon P, Oberholzer J, Occhiodoro T, Morel P, Lou J, Trono D. Reversible immortalization of human primary cells by lentivector-mediated transfer of specific genes. *Mol. Ther.* 2:404–414, 2000
31. Schultz LB, Chehab NH, Malikzay A, Halazonetis TD. p53 binding protein 1 (53BP1) is an early participant in the cellular response to DNA double-strand breaks. *J. Cell Biol.* 151:1381–1390, 2000
32. Simpson P, Savion S. Differentiation of rat myocytes in single cell cultures with and without proliferating nonmyocardial cells: Cross-striations, ultrastructure, and chronotropic response to isoproterenol. *Circ. Res.* 50:101–116, 1982
33. Smalley MJ, Dale TC. Wnt signalling in mammalian development and cancer. *Cancer Metastasis Rev.* 18:215–230, 1999
34. Takahashi K, Yamanaka S. Induction of pluripotent stem cells from mouse embryonic and adult fibroblast cultures by defined factors. *Cell.* 126:663–676, 2006
35. Takahashi K, Tanabe K, Ohnuki M, Narita M, Ichisaka T, Tomoda K, Yamanaka S. Induction of pluripotent stem cells from adult human fibroblasts by defined factors. *Cell.* 131:861–872, 2007
36. Tandon N, Cannizzaro C, Chao PH, Maidhof R, Marsano A, Au HT, Radisic M, Vunjak-Novakovic G. Electrical stimulation systems for cardiac tissue engineering. *Nat. Protoc.* 4:155–173, 2009
37. Westerman KA, Leboulch P. Reversible immortalization of mammalian cells mediated by retroviral transfer and site-specific recombination. *Proc. Natl. Acad. Sci. U.S.A.* 93:8971–8976, 1996
38. Xia Z, Dickens M, Raingeaud J, Davis RJ, Greenberg ME. Opposing effects of ERK and JNK-p38 MAP kinases on apoptosis. *Science.* 270:1326–1331, 1995
39. Yamada K, Green KG, Samarel AM, Saffitz JE. Distinct pathways regulate expression of cardiac electrical and mechanical junction proteins in response to stretch. *Circ. Res.* 97:346–353, 2005
40. Yang L, Soonpaa MH, Adler ED, Roepke TK, Kattman SJ, Kennedy M, Henckaerts E, Bonham K, Abbott GW, Linden RM, Field LJ, Keller GM. Human cardiovascular progenitor cells develop from a KDR+ embryonic-stem-cell-derived population. *Nature.* 453:524–528, 2008

Chapter 3 Patterning stem cells differentiation - Patterning osteogenesis by inducible BMP-2 expression in microfluidic systems

3.1 Abstract

The development of transitional interfacial zones between adjacent tissues remains a significant challenge for developing tissue engineering and regenerative medicine strategies. Using osteogenic differentiation as a model, we describe a novel approach to spatially regulate expression and secretion of the bone morphogenetic protein (BMP-2) in a two-dimensional field of cultured cells, by flow patterning the modulators of inducible BMP-2 gene expression. We first demonstrate control of gene expression, and of osteogenic differentiation of the cell line with inducible expression of BMP-2. Then we design laminar flow systems, with patterned delivery of Doxycycline (Dox), the expression modulator of BMP-2. The patterned concentration profiles were verified by computational simulation and dye separation experiments. Patterned differentiation experiments conducted in the flow systems for three weeks showed the Dox concentration dependent osteogenic differentiation, as evidenced by mineral deposition. In summary, by combining inducible gene expression with laminar flow technologies, this study provided an innovative way to engineer tissue interfaces.

3.2 Introduction

Highly organized structures are a defining feature of biological tissues. Among these structures, tissue interfaces play central roles in organ development and

function. For example, in musculoskeletal systems, the interface between bone and soft tissue facilitates transmission of mechanical loads and minimizes stress concentration in junctions (Thomopoulos et al., 2003). Without adequate tissue interaction in such junctions, conventional soft tissue grafts fail at the bone insertion site (Woo et al., 2006). An important goal in cell and tissue engineering is therefore to recapitulate tissue interfaces, if the organization of the engineered tissue is to reflect that of native tissue.

Numerous regeneration approaches have been investigated to reconstruct functional tissues interfaces. The layered structure combined with multiple-phase culture is commonly used to pattern different cells, and construct tissue interfaces (Mitsuhashi et al., 1993). One strategy to engineer osteochondral tissue interface is to fabricate a polymer scaffold consisting of two layers of materials with distinct properties—such as porosity, mechanical strength and material microstructure, to mimic the natural environment for bone and cartilage development. These scaffolds are seeded with either human mesenchymal stem cells or pre-differentiated chondrocytes and osteoblasts and the tissue formation is investigated *in vitro* or *in vivo* studies (Che et al., 2006; Shao et al., 2006; Chang et al., 2004; Tuli et al., 2004). However this approach is restricted by inherent discontinuities across different materials (Spalazzi et al., 2006). Growth factors and chemokines can serve as powerful long-range mediators of cellular organization and function (Chung et al., 2005). Thus, constructing growth factor gradients within the structure could be a promising way to develop tissue

interfaces. In some studies, sustained release of growth factors incorporated into polymer scaffolds facilitated bone and cartilage differentiation *in vitro* and *in vivo* (Li et al., 2006; Hosseinkhani et al., 2007; Boyan et al., 1999). However the dose of growth factors in these scaffold systems was not well defined, due to the lack of optimal techniques to deliver and maintain growth factor signals in engineered constructs (Langer, 1998).

Recent studies have focused on alternative strategies, by directly modulating spatial patterns of gene expression within a cell population, thereby modulating the functions of cells. Ziauddin and Sabatini demonstrated that gene expression could be patterned in culture *via* a reverse transfection procedure wherein plasmid DNA was immobilized on a substrate onto which a monolayer of cells was subsequently grown (Ziauddin and Sabatini, 2001). But this approach has been limited by the low efficiency of plasmid transfection. To alleviate the limitations of plasmid-based transfection, more efficient viral vectors (which may present safety issues) have been used to construct tissue interface by spatial regulation of gene transfer (Phillips et al., 2008).

In the present study we proposed a new strategy to pattern cell differentiation by patterning gene expression modulator within laminar fluidic system. When parallel laminar streams of different liquids flow inside a channel at a low Reynolds number ($Re < 1$), there is no mixing between these adjacent streams, other than by diffusion. For this reason, laminar flow systems have been utilized

for separations or patterning of the cells and factors (Takayama et al., 1999; Kenis et al., 1999; Rhee et al., 2005; Takayama et al., 2003). The generation of specific patterns by using such fluidic methods is rather straightforward, as the characteristics of the fluidic environment can be tightly controlled.

We chose an inducible BMP-2 expressing cell line (C9) under the control of Tet-off gene expression system. This model can provide efficient control of BMP-2 gene expression by modulating the concentration of BMP-2 expression modulator doxycycline (Dox) (**Figure 3.1**). BMP-2 belongs to the transforming growth factor superfamily and plays an important role in osteogenesis and bone metabolism, serving as a powerful inducer of osteoblast differentiation *in vitro* and bone formation *in vivo* (Hay et al., 1999; Ruhe et al., 2004). Therefore, by patterning the delivery of Dox to the cultured cells in laminar flow system, we can effectively pattern the expression of BMP-2 and thereby modulate osteogenic differentiation (**Figure 3.2A**).

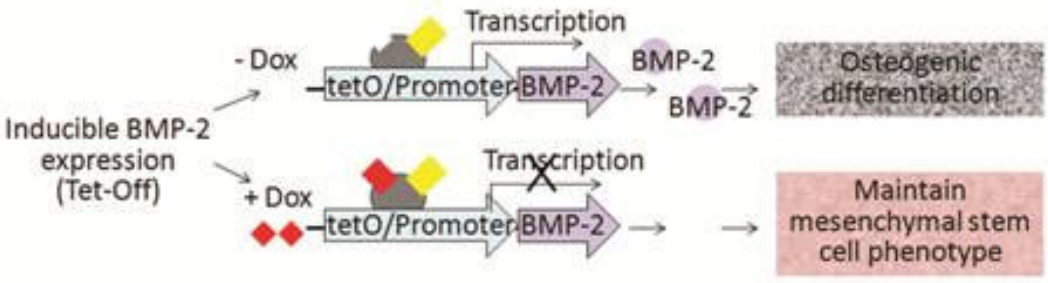

Figure 3.1 Biological model of inducible BMP-2 expression under Tet-off gene expression Dox concentration dependent BMP-2 expression leads to concentration-dependent osteogenic differentiation.

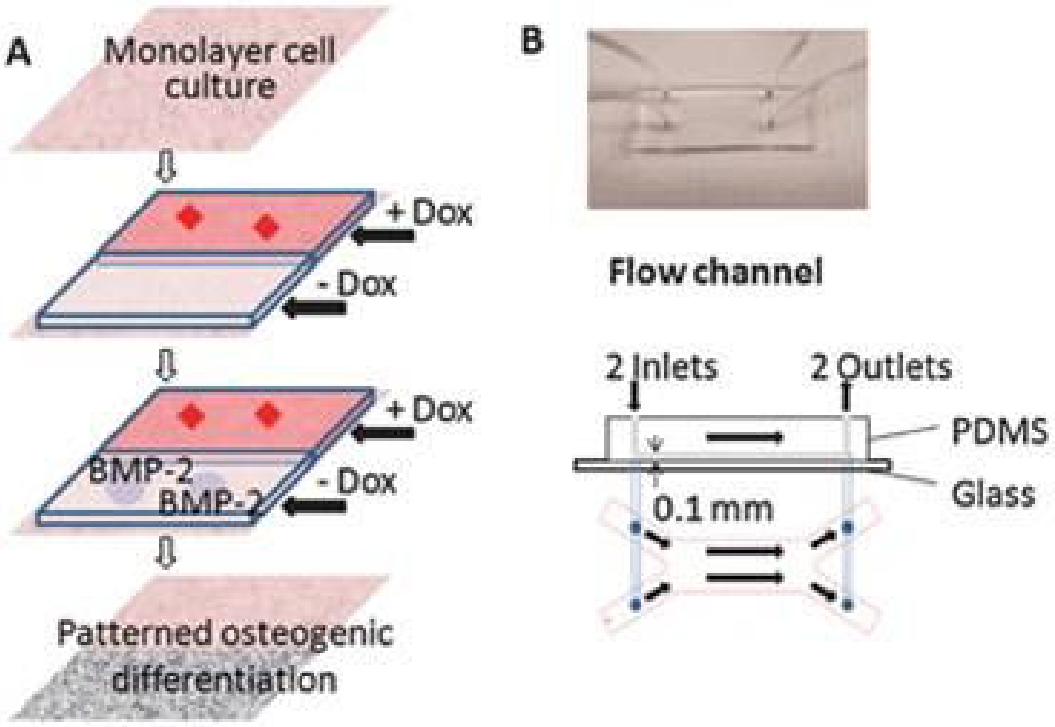

Figure 3.2 Experimental system (A) Strategy for patterning osteogenic cell differentiation. Cultured cells with inducible BMP-2 expression are exposed to laminar flow with two streams (one with and one without Dox), generating a pattern of Dox concentration. The patterned Dox concentration profile leads to patterned BMP-2 expression, and thereby to patterned osteogenic differentiation. **(B)** Flow channel (main channel: 20 mm L × 6 mm W × 0.1 mm H).

First, we characterized the inducible BMP-2 expression cell line (C9) in static culture, and proved that BMP-2 secretion was dependent on Dox concentration (0–1 ng ml^{-1}). By modulating Dox concentration, we could modulate the BMP-2 mediated osteogenic differentiation, as verified by calcium deposition and alkaline phosphatase (ALP) analysis. Then we designed a laminar-fluidic system microfluidic channel (**Figure 3.2B**). These fluidic systems can deliver different levels of Dox concentration to cultured monolayers of cells. In 3-week experiments of osteogenic differentiation, we demonstrated that patterning of

osteogenesis in a mesenchymal stem cell line can be achieved by patterning BMP-2 gene expression modulator, Dox.

We also developed a larger fluidic chamber (**Supplemental Figure 3.1**) and successfully replicated the same method for patterned osteogensis over a larger field of cells. In addition to the scale up to larger cell numbers, this fluidic chamber can accommodate cultivation of cells in a scaffold sheet or a layer of hydrogel for generating a 3D tissue interface.

3.3 Materials and Methods

3.3.1 Cell culture and osteogenic differentiation

The BMP-2 inducible expression cell line (C9 cell) was orginated from C3H10T1/2 murine MSCs cell line after transfection with the human BMP-2 gene under control of the inducible Tet-off system (Moutsatsos et al., 2001; Noël et al., 2004). The C9 cells were cultured in *basic medium*: Dulbecco's Modified Eagle's Medium (DMEM) (Fisher, Pittsburg, PA) supplemented with 10% fetal bovine serum (Fisher), 2 mM L-glutamine, 100 U ml^{-1} penicillin, 100 µg ml^{-1} streptomycin (Invitrogen, Carlsbad, CA), and 1 µg ml^{-1} Dox (Sigma-Aldrich, St Louis, MO) to repress BMP-2 secretion. Every 2–3 passages, C9 cells were subjected to *selection medium*: basic medium supplemented with 500 mg ml^{-1} G418, 200 mg ml^{-1} hygromycin (Sigma-Aldrich), and 1 µg ml^{-1} Dox to eliminate the cells which lost their genotype. For osteogenic differentiation, C9 cells were cultured in *differentiation medium*: basic medium supplemented with 10 mM

sodium-*b*-glycerophosphate, 0.05 mM ascorbic acid-2-phophate (Sigma-Aldrich) and with or without Dox added. Medium was changed twice a week.

3.3.2 BMP-2 and DNA

Secretion of BMP-2 into culture medium was measured by BMP-2 sandwich ELISA kit, according to the manufacturer's protocol (R&D Systems; Minneapolis, MN). For evaluating DNA content, the cells cultured in monolayer were washed in PBS, placed in digestion buffer (10 mM Tris, 1 mM EDTA, and 0.1% Triton X-100 with 0.1 mg mL^{-1} proteinase K, Sigma-Aldrich) in centrifuge tubes, and incubated overnight at 50 °C. The supernatants were sampled, the Picogreen dye (Molecular Probes, Eugene, OR) was added to the samples in 1 : 1 ratio, and read in fluorescent plate reader at excitation of 485 nm, emission of 528 nm (BioTek, Winooski, VT). A standard curve was prepared from a solution of salmon testes DNA (Molecular Probes).

3.3.3 Alkaline phosphatase (AP) measurement and staining

For alkaline phosphatase (ALP) measurement, cells were harvested in 100 µL of lysate buffer consisting of PBS (Fisher), 1% Triton X-100, 0.5% sodium deoxycholate, 0.1% sodium dodecyl sulfate, 0.1 mg mL^{-1} phenylmethylsulfonylfluoride (PMSF) and 3% aprotinin (Sigma-Aldrich), that was maintained on ice and vortexed intermittently for 30 min to break down the cell membranes. The extracts were removed, centrifuged and the supernatants were stored at −20 °C. 50 µL of a sample was incubated with 50 µL of alkaline buffer

and 50 µL nitrophenyl-phosphate substrate solution (Sigma-Aldrich) in micro-centrifuge tubes at 37 °C for 10–20 min. The reaction was stopped with 0.5 N NaOH (Sigma-Aldrich). The absorbance was read at 405 nm (Molecular Devices, Sunnyvale, CA) and compared to a standard curve obtained from *p*-nitrophenol solutions (Sigma-Aldrich) of known concentrations. For ALP staining, the cultured cell monolayer was fixed in citrate buffered acetone for 30 s, after rinsing in distilled water for 45 s, and the fixed monolayer was immersed into alkaline-dye mixture consisting of 4% AS-MX Phosphate Alkaline solution in diluted diazonium salt solution (Sigma-Aldrich), for 30 min in dark, and washed in de-ionized water. ALP staining was captured by microscope (Olympus IX81, Center Valley, PA).

3.3.4 Calcium measurement and von Kossa staining

For calcium measurement, the cells were extracted by 5% trichloroacetic acid (Sigma-Aldrich), and diluted as necessary to be within tolerance ranges of assay. Ocresolphtalein complex was added (Calcium CPC LiquiColor Test, Stanbio Laboratory, Boerne, TX) and the calcium content was measured in spectrophotometer at 550 nm (Molecular Devices). For von Kossa staining, the cultured cells monolayers were washed with PBS and fixed in cold 10% buffered formalin (Fisher). The cells were then rinsed by distilled water and then immersed in 5% silver nitrate (Sigma-Aldrich) solution followed by exposure to bright light for 1 h. Mineralization was captured by microscope (Olympus X81).

3.3.5 Bone sialoprotein (BSP) staining

For BSP staining, cell monolayers were washed with PBS and fixed in cold 10% buffered formalin (Fisher). The cells were then rinsed by distilled water quenched with 0.3% H_2O_2, and blocked with PBS containing 5% BSA and 0.02% (vol/vol) goat serum (Sigma-Aldrich) for 30 min at room temperature. After rinsing with PBS, slides were incubated with 1 : 1000 BSP antibody (Sigma-Aldrich) overnight. The fixed cells were washed with PBS and incubated with biotinylated goat anti-rabbit serum (Sigma-Aldrich) and Vectastain ABC Kit (Vector Laboratories, Burlingame, CA) for 30 min at room temperature. Brown color was developed with SIGMAFAST diaminobenzidine (Sigma-Aldrich) for 10 min at room temperature. Slides were then counter-stained with hematoxylin (Sigma-Aldrich).

3.3.6 Design and manufacture of fluidic systems

3.3.6.1 Flow channel

A microfluidic flow channel (**Figure 3.2B**) was fabricated by using standard soft lithography methods. Photo-masks with channel patterns were designed using AutoCAD (AutoDesk, San Rafael, CA), and printed on transparencies with 20 000 dpi resolution. Master molds patterned with 100 μm thick resist were made by patterning a negative photoresist on a silicon wafer (manufactured by Stanford Microfludics Foundry). PDMS molds were fabricated by curing prepolymer (Sylgard 184, Essex Chemical, Midland, MI) on silicon masters patterned with SU-8 photoresist. Briefly, PDMS prepolymer composed of elastomer and curing agent at 10 : 1 ratio, was poured on the silicon master that

was patterned with photoresist and cured at 60 °C for 2 h. The PDMS molds were peeled off the silicon wafer. The inlet and outlet of the micro channel were created by a sharp punch (1 mm diameter, Fisher) for medium perfusion and cell seeding. The complete microfluidic device consisted of a top PDMS fluidic channel, a bottom glass slide, tygon tubing (0.79 mm inside diameter (ID), 2.38 mm outside diameter (OD), McMaster, Robbinsville, NJ), stainless steel tubing (0.64 mm ID, 0.81 mm OD, McMaster) and syringe pump (Harvard Apparatus, Boston, MA). The main fluidic channel was 100 μm high × 20 mm long × 6 mm wide, and the branches were 100 μm high × 10 mm long × 3 mm wide. The microfluidic layer was bonded to oxygen plasma treated glass slide (Harrick Scientific, Pleasantville, NY), with channels at the top, slide at the bottom).

3.3.6.2 Flow experiments

The flow channel was sterilized by overnight exposure to 70% ethanol and UV light. Tubing was sterilized separately. The channels were coated with 10 μg ml^{-1} of fibronectin for 2 h, and let dry. A suspension of C9 cells was loaded into the channel (150 μL of suspension, at 1 × 10^5 cells mL^{-1}) and incubated overnight in a 37 °C/5% CO_2 humidified incubator. In this case, the cells formed a confluent monolayer. Prior to the experiment, the flow channel was connected to a syringe pump *via* tubing that was primed with proper culture medium, and the output ports were connected to the waste container.

For dye separation experiments, cells were subjected to 2 continuous streams of flow for 30–60 min, with one stream of media containing 2 μM Calcein-AM, and the other stream of unsupplemented medium. The stream with Calcein-AM was subsequently replaced with unsupplemented medium for a 30 min wash. For osteogenic differentiation experiments, cells were continuously perfused in differentiation medium, with 1 ng ml^{-1} or 0 ng ml^{-1} Dox for 3 weeks.

3.3.7 Mathematical model

3.3.7.1 Velocity and shear stress profiles

The channel geometry was selected to permit calculation of the wall shear stress as a function of laminar flow rate:

$$\tau_w = \frac{6\mu Q}{wh^3} \quad (1)$$

and the Reynolds number:

$$R_e = \frac{2\rho Q}{\mu(w+h)} \quad (2)$$

where μ is the fluid viscosity and ρ is the fluid density, Q is the fluid flow rate, w and h are the width and height of the channel/chamber. The hydrodynamic development length L in a channel of a height h can be estimated as (Atkinson et al., 1969):

$$\frac{L}{h} = 0.3125 + 0.011R_e \quad (3)$$

3.3.7.2 Computational model

A computational model based on finite element method (COMSOL Multiphysics v3.2, Burlington, MA) was used to simulate the concentration and velocity profiles in the channel/chamber. The concentration gradient could be described by 3D Navier–Stokes equations for incompressible laminar flow:

$$\rho\left(\frac{\mathrm{d}u}{\mathrm{d}t} + (u\nabla u)\right) = -\nabla p + \mu\nabla^2 u \qquad (4)$$

$$\nabla u = 0 \qquad (5)$$

and the convection-diffusion transport equation

$$\frac{\mathrm{d}c}{\mathrm{d}t} + (u\nabla)C = D\nabla^2 CX \qquad (6)$$

where ρ, u, and p are the density, flow velocity and pressure of the liquid, respectively, and C and D are the concentration and diffusivity of the molecules. At each time step, the flow velocity was first calculated independently, and the concentration was then determined for the computed flow. The boundary conditions were as follows. At the inlet, flow velocity was set according to the specific experiment. At the outlet, we imposed zero normal stress. At the channel walls, we imposed the no-slip condition, and no flux condition. For the convection-diffusion equation, a constant concentration was set at the channel inlet.

3.3.8 Image analysis

The sequential images were acquired using an inverted microscope (Olympus IX81), stored, assembled and analyzed digitally by Photoshop CS4 program (Adobe, San Jose, CA). For quantitative analysis of calcium deposition staining, the assembled color images were converted to black and white images, and the brightness and darkness of the images were inverted, to capture the dark stain of calcium deposition. Calcium deposition was quantified from ratio of the normalized sum of segmented image intensity and the minimum segmented image intensity, moving along the width of the channel/chamber, and using the Matlab R2007 program (Matlab, Natick, MA).

3.3.9 Statistics/data analysis

Data were expressed as mean ± standard deviation (SD) of the measured values. Data were analyzed by ANOVA for multiple comparisons, and a post hoc test for group to group comparisons, with $P < 0.05$ considered statistically significant.

3.4 Results

3.4.1 Regulation of BMP-2 expression and osteogenic differentiation in static culture

We first characterized the Dox-dependent BMP-2 secretion and Dox-dependent osteogenic differentiation in static culture, for a series of Dox concentrations (0–1000 ng ml^{-1}, **Figure 3.3**). For C9 cells grown in static culture, secretion of BMP-2 was induced when Dox concentration in osteogenic differentiation medium was

<1 ng ml^{-1}. The amount of secreted BMP-2 in medium was negatively correlated to the concentration of Dox, and reached ther maximum level when Dox was absent from medium. During 4 weeks of osteogenic differentiation, BMP-2 was mostly secreted within the first 2 weeks of culture, after which the secretion of BMP-2 significantly decreased, possibly due to the decrease in cell metabolism with time in culture. When Dox concentration was ≥1 ng ml^{-1}, BMP-2 secretion could not be detected by ELISA throughout the culture period (**Figure 3.3A**). The DNA measurements of the C9 cells showed that the variation of Dox concentration from 1000 ng ml^{-1} to 0 ng ml^{-1} had no significant effect on cell proliferation in the osteogenic-inductive culture (**Figure 3.3B**). The Dox concentrations in the range 1 ng ml^{-1} to 0 ng ml^{-1} induced Dox-dependent expression of BMP-2 that in turn induced BMP-2-dependent osteogenic differentiation of C9 cells, as evidenced by calcium deposition and expression of ALP (**Figure 3.3C–F**). Calcium measurement and von Kossa staining showed no detectable calcium deposition until the 3rd week of static culture. C9 cells cultured at lowest range of Dox concentrations (0 or 0.1 ng ml^{-1})

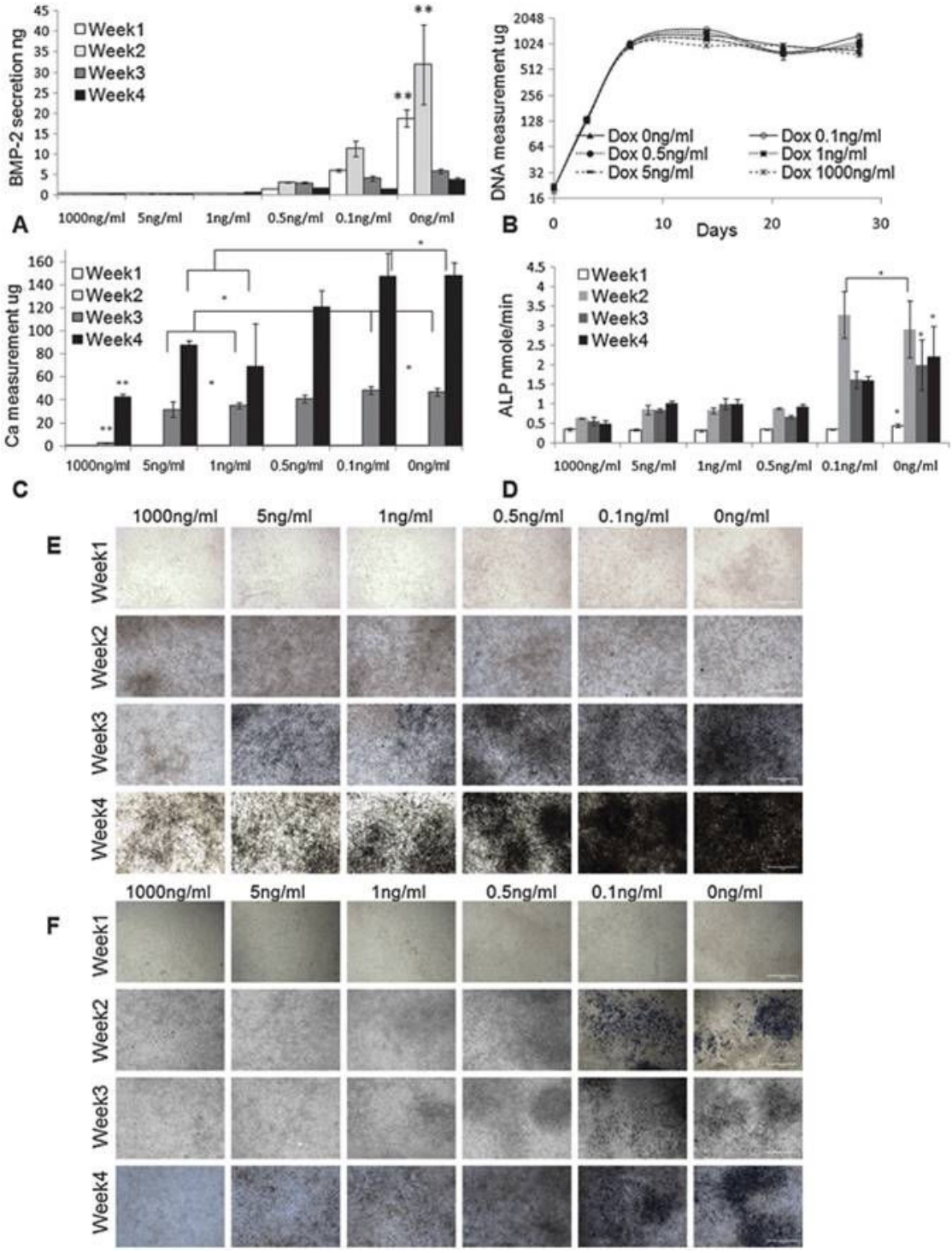

Figure 3.3 Characterization of inducible BMP-2 expressing cell line (C9) (A) ELISA measurement of the secreted BMP-2 in culture media (n = 3). **(B)** C9 cell proliferation profile by DNA measurement (n = 6). **(C)** Measurement of Calcium deposition (n = 4). **(D)** Measurement of alkaline phosphates (AP) (n = 4). *: $p < 0.05$. **: $p < 0.05$. **(E)** von Kossa staining of the C9 cells. **(F)** AP staining of the C9 cells. Original magnification: 200×. Scale bar: 1 mm.

had significantly higher deposition of calcium than C9 cells cultured at higher Dox concentrations (≥1 ng ml^{-1}) in weeks 3–4 of culture (**Figure 3.3C and E**). Consistently, the ALP expression in cells cultured at low Dox concentrations (0 or 0.1 ng ml^{-1}) was high after one week of osteogenic induction culture (**Figure 3.3D and F**), demonstrating the initiation of osteogenic differentiation.

In summary, the *in vitro* static culture suggested strong correlations between Dox concentration, BMP-2 secretion and osteogenic differentiation. These BMP-2 induced cells exhibited a clear "cutoff" of BMP-2 expression and osteogenic differentiation at Dox concentration of 1 ng ml^{-1}, and the differentiation was detectable after 3 weeks of culture. Based on these findings, in subsequent flow experiments we used bi-laminar flows of C_{Dox} = 1 ng ml^{-1} and C_{Dox} = 0 ng ml^{-1} to generate osteoblast–fibroblast interface in the same construct.

3.4.2 Characterization of the flow channel

The velocity profiles and concentration profiles in the device were analyzed in detail using COMSOL Multiphysics®. Firstly, the flow and mixing in the fluidic channel were determined. In order to generate a concentration interface perpendicular to the flow inside the channel, it was necessary that the flow past the inlet tubes be fully developed and laminar.

The flow was characterized by low Reynolds numbers, of 0.055–0.011 for the channel, for the range of flow rates studied (**Figure 3.4**). The maximum flow rate

of 5 µl min^{-1} × 2 corresponded to Re = 0.055 and the hydrodynamic development length of 32 µm in the flow channel. Thus, the flow in each system could be considered as fully developed, with negligible variation in the direction transverse to flow. The wall shear stress in the cell culture zone was 16.7–3.3 mPa.

Flow Channel: Cell culture area 120 mm^2		
L	W	H
20 mm	6 mm	0.1 mm
Flow Rate: Q	Shear Stress: τ	Reynolds: Re
5 µl/min x 2	16.7 mPa	0.055
1 µl/min x 2	3.3 mPa	0.011

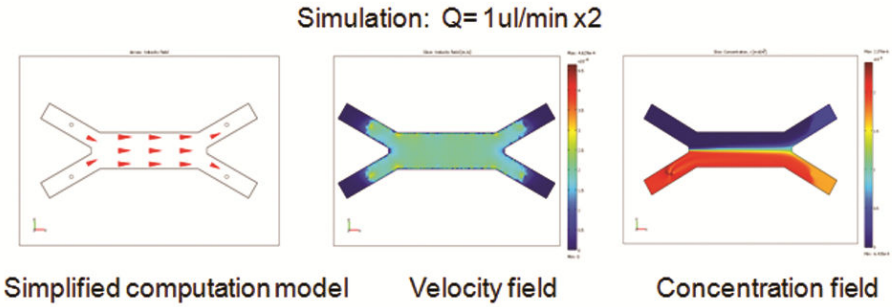

Figure 3.4 Flow analysis Simplified flow model, the steady-state velocity and concentration profiles are shown for a flow rate of 1 µl min^{-1} × 2. Data were calculated for the diffusion coefficient D_{Dox} = 3.93 × 10^{-6} cm^2 s^{-1}, fluid viscosity v = 10^{-3} Pa s, fluid density ρ = 10^3 kg m^{-3}, and inlet concentrations C_{Dox} = 1 ng ml^{-1} = 2.25 × 10^{-12} mol ml^{-1} and C_{Dox} = 0 ng ml^{-1}.

Simplified fluidic models were developed to study the flow and concentration profiles at steady state (**Figure 3.4**). Different values of the flow rate were simulated, while maintaining at constant levels the other parameters, such as diffusion coefficient (D_{Dox} = 3.93 × 10^{-6} cm^2 s^{-1}) (Wilke and Chang, 1955), flow viscosity (v = 10^{-3} Pa s), fluid density (ρ = 10^3 kg m^{-3}) and input concentrations (C_{Dox} = 1 ng ml^{-1} = 2.25 × 10^{-12} mol ml^{-1}; C_{Dox} = 0). Simulation showed that two fluid flows meet in the device, creating a concentration interface. Complete mixing inside the channel was dependent on the flow rate.

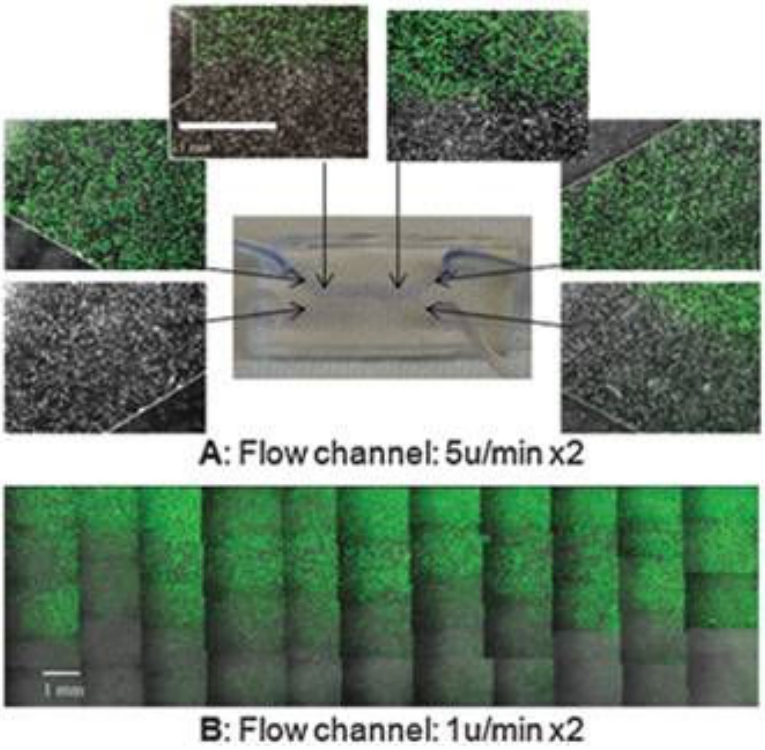

Figure 3.5 Dye separation studies Separation of Calcein stain in the flow channel at the flow rates of 5 µl min^{-1} × 2 **(A)** and 1 µl min^{-1} × 2 **(B)**. Data are for the diffusion coefficient of Calcein $D_{Calcein}$ = 2.6 × 10^{-6} cm^2 s^{-1}, and inlet concentrations of Calcein C_+ = 2 µM and C_- = 0, diffusion coefficient of Trypan blue of $D_{Trypan\ blue}$ = 2.21 × 10^{-6} cm^2 s^{-1}, and input concentrations of Trypan blue of C_+ = 229 µM and C_- = 0. Flow direction is left to right. Original magnification: 100×. Scale bar: 1 mm.

To visualize the concentration profiles in each of the fluidic systems, Calcein-AM, ($D_{Calcein}$ = 2.6 × $10^{-6}$$cm^2$ s^{-1}) was used as a model molecule, and the fluorescent images were acquired to show selective Calcein distribution only in cells within the channel (**Figure 3.5**). The concentration profiles were additionally verified in experiments that used the trypan blue dye (D_{trypan_blue} = 2.29 × 10^{-6} cm^2 s^{-1}). In summary, the patterned Calcein/Trypan blue distribution verified the simulation result, indicating that the bi-laminar-fluidic system permitted the alignment of two flows with different concentration profiles.

3.4.3 Patterning of osteogenic differentiation

We examined the effect of patterning Dox concentration on osteogenic differentiation. Mineral deposition within cell culture constructs was analyzed after 3 weeks dynamic culture in osteogenic differentiation media as a functional marker of osteogenesis. The result showed C9 cells cultured with continuous Dox (1 ng ml^{-1}) treatment displayed less mineral deposits (**Figure 3.6A1 and A2**), whereas C9 cells cultured without Dox treatment displayed more and relatively uniform mineral deposits (**Figure 3.6C1 and C2**). C9 cells cultured in a gradient of Dox concentration exhibited zonal organization of mineral deposition (**Figure 3.6B1 and B2**). By pooling together the independent experiments, and quantifying the normalized intensity of mineralization in the flow chamber, we observed a gradual decrease in mineralization across the Dox 0 ng ml^{-1} and Dox 1 ng ml^{-1} interface (**Figure 3.6B3**), that was not observed at continuous Dox concentrations of 1 ng ml^{-1} ((**Figure 3.6A3**), or 0 ng ml^{-1} (**Figure 3.6C3**). However, we also observed some scattering of mineralization across the interface, and close to edge areas, possibly due to molecular diffusion of Dox, intracellular signalling of BMP-2, edge effects, or disturbances of flow during medium exchange.

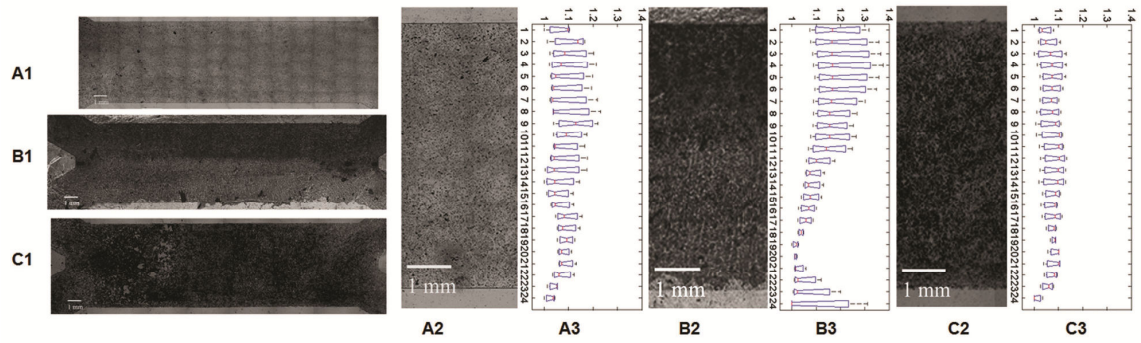

Figure 3.6 Dox dependent osteogenic differentiation in the flow channel. C9 cells were cultured in osteogenic differentiation medium in a perfused flow channel, at a flow rate of 1 µl min^{-1} × 2, for 3 weeks. Images show von Kossa staining of calcium deposition for selected conditions: **(A1, A2)** Perfusion medium with Dox 1 ng ml^{-1} (top)/1 ng ml^{-1} (bottom); **(B1, B2)** Perfusion medium: Dox 0 ng ml^{-1} (top)/1 ng ml^{-1} (bottom); **(C1, C2)** Perfusion medium: Dox 0 ng ml^{-1} (top)/0 ng ml^{-1} (bottom). **(A3, B3, C3)** Intensity of calcium staining, obtained by pooling repeated experiments (*n* = 3 per condition). The staining of the deposited calcium is expressed at the ratio of the normalized sum of segmented (~0.25 mm) image intensity and the minimum intensity along the *y* axis (the width) of the chamber. Data were processed using Matlab R2007 program. Flow direction: left to right. Scale bar: 1 mm

After the flow channel was scaled up to the fluidic chamber (**Supplemental Figure 3.1**), we successfully replicated the computational simulation of the fluidic profiles, the dye separation test (**Supplemental Figure 3.2**), and the patterning of osteogenc differentiation (**Supplemental Figure 3.3**).

We observed significant effects of medium flow rate on osteogenic differentiation. Under high flow rate at 5 µl min^{-1} × 2 in fluidic channel (**Supplemental Figure 3.4A**), or 8 µl min^{-1} × 2 in fluidic chamber (**Supplemental Figure 3.4B**), the C9 cells exhibited a less differentiated phenotype, compared to the cells cultured at a flow rate of 1 µl min^{-1} × 2 in fluidic channel (**Figure 3.6**), or 4 µl min^{-1} × 2 in fluidic chamber (**Supplemental Figure 3.3**). Osteogenic differentiation was further enhanced by lowering the flow rate to 0.5 µl min^{-1} × 2 in fluidic channel

(**Supplemental Figure 3.4C**). These effects were likely due to the dilution of cell-secreted factors (such as BMP-2) at higher medium flow rates.

We were not able to generate an uniform gradient of ALP staining along the Dox concentration profile. In contrast, we observed a clear pattern of distribution of bone sialoprotein, a major component of the bone extracellular matrix, that followed the pattern of Dox concentration, both in flow channel and flow chamber (**Supplemental Figure 3.5B and C**). In addition, we observed relatively uniform distribution of cells after 3 weeks fluidic culture (**Supplemental Figure 3.5A**). Taken together, these results demonstrate that spatial control over Dox distribution can lead to spatial control over BMP-2 expression, and spatial control over osteogenic differentiation.

3.5 Discussion

We explored a novel strategy to patterning osteogenic differentiation to generate a stable interface between differentiated and undifferentiated cells. Osteogenic differentiation was patterned by BMP-2 gene expression, which in turn was patterned by the BMP-2 modulator Dox, using a bi-laminar microfluidic system. This strategy of patterning the expression of key master regulator genes within tissues mimics the mechanisms of the development that underlie patterned differentiation *in vivo* (Seris et al., 2005). Previous gene expression and immunohistochemical studies described distribution and localization of BMP-2 during bone formation (McCullough et al., 2007; Ohyama et al., 2004), consistent

with the known effect of BMP-2 gradients on osteogenesis. BMP-2 gradients were also implicated in chondrogenic differentiation in the growth plate (Nilsson et al., 2007) and in pituitary organogenesis (Treier et al., 1998). The formation of BMP-2 gradients thus provides an interesting approach for application in tissue engineering.

Characterization of the C9 cells with inducible BMP-2 gene expression in static culture showed that BMP-2 secretion was tightly controlled by Dox concentration. The C9 cells had clear "cutoff" of BMP-2 secretion at Dox of 1 ng ml^{-1}. In the range of Dox concentrations of 1 ng ml^{-1} to 0 ng ml^{-1}, the cells showed Dox-dependent BMP-2 secretion, leading to BMP-2-mediated osteogenic differentiation, that was clearly evidenced by calcium deposition and ALP activity. Therefore, by coupling the Dox-dependent BMP-2 secretion and BMP-2-dependent osteogenic differentiation, we were able to directly control osteogenic differentiation by the gene expression modulator, Dox. Notably, Dox is a simple semi-synthetic tetracycline (molecular weight of 444), widely used to treat a variety of infections (Sweet et al., 1988), which could provides a cost-effective and efficient "turn on"–"turn off" functions for engineering tissue functionality. The "turn on"–"turn off" functions of the inducible gene expression could be further used in a temporary manner, and adapted to study the dynamics of gene expression in cell differentiation processes.

The microfluidic channel designed to conduct the present study is a simple device with two parallel laminar flow streams. The computational simulation and dye separation studies confirm that this microfluidic system can be used to create distinct regions of constant concentration and form time-invariant gradients across the cell culture area, due to the lack of convective mixing under low-Re number laminar flow. After 3 weeks of cell culture with perfusion that generated a patterned delivery of Dox, we observed patterned osteogenic differentiation that correlated to the pattern of Dox concentration. In the microfluidic chamber, after 3 weeks of osteogenic differentiation, a transient gradient of mineral deposition, with high calcium deposition at the top and low calcium deposition at the bottom, was established, in response to the Dox concentration profiles.

Compared to the fluidic channel, the fluidic chamber offers additional flexibility. First, it allows the cells to be attached to a glass slide before the chamber assembly, which can provide better control of cell seeding and distribution, a feature suitable to a variety of cell culture applications. Second, as the length of the flow chamber is increased, more mixing may occur *via* diffusion perpendicular to the direction of fluid flow, while keeping input flow rates and compositions constant. Therefore, we were able to create and maintain a range of gradients by carefully choosing the concentrations and flow rates of the fluid streams, for long periods of time. This feature may enable studies of more sophisticated cell functionality in response to gradients of signals. Third, the height of the fluidic chamber can be varied, by adjusting the thickness of the

gasket, thereby adjusting shear stress in the system. Potentially, the microfluidic chamber could be eventually up-graded to hold slim 3-dimensional tissue constructs for study of higher order tissue interfaces.

In laminar-fluidic systems, the paracrine/autocrine signals released by the cells in response to the applied gradient could be quickly removed by medium perfusion and accumulated downstream. In this study we observed that flow diluted the extracellular concentration of BMP-2, leading to “less differentiated” phenotype compared to static culture. These effects could be modulated to some extent by adjusting the flow rates. By decreasing the flow rates, from 8 μl min^{-1} × 2 to 4 μl min^{-1} × 2 in fluidic chamber, or from 5 μl min^{-1} × 2 to 1 μl min^{-1} × 2 in fluidic channel osteogenic differentiation was markedly enhanced calcium deposition.

We also observed that the osteogenic differentiation increased at the channel walls, presumably due to the edge effects in laminar flow system. In a typical laminar flow profile, the highest velocity is found in the center of channel or chamber, while the lowest velocity (V = 0) is found along the wall. As discussed above, osteogenic differentiation is enhanced at lower fluid flow rates. Therefore, the zero velocity along the wall can lead to the accumulation of autocrine and paracrine signals, and result in a higher degree of osteogenic differentiation even with the presence of Dox. Therefore, we suggest that the analysis of cell differentiation in this flow system needs to take into account the edge effects.

In summary, we developed an interface between osteogenic and undifferentiated cells, as a prototype of our proposed patterned gene expression strategy. The 2D system investigated in this study presents a valuable tool for controlled *in viro* study of osteogenesis.

Patterned osteogenesis of mesenchymal stem cells, when scaled up to 3D, would enable generation bone-ligament or osteo–chondrogenic interface in engineered tissue constructs. Future work of interest includes patterning of osteogenesis–fibrogenesis interfaces, by modulation of inducible BMP-2 expression on one side of the interface, and modulation of other growth factors (Lee et al., 2010) (connective tissue growth factor, CTGF, and TGF-beta1) on the other side of the interface, using the fluidic chamber. Likewise, osteogenic–chondrogenic interface could be patterned by constructing a super vector composed of two gene expression cassettes—inducible BMP-2 expression under Tet-on promoter and inducible Sox9 under RheoSwitch promoter. Such a vector would mimic a biological circuit controlling the expression of two separate genes (BMP-2 and Sox9) with combination of modulators.

3.6 Conclusion

In summary, this study demonstrates that a continuous, graded osteogenesis tissue interface can be established by patterning the BMP-2 gene expression, *via* patterning of the BMP-2 modulator Dox, using a simple laminar-fluidic system. This approach provides an alternative way to develop transitional interface zones

for enhanced tissue integration and biological function. The technology also provides an interesting model to study how a gradient of gene expression can modulate cell fate and expression of a specific phenotype or function. The use of alternative cell types and 3-dimensional scaffolds could enable regeneration of more sophisticated, higher-order tissue interfaces that mimic the structural and functional characteristics of native tissues.

3.7 Supplemental Information

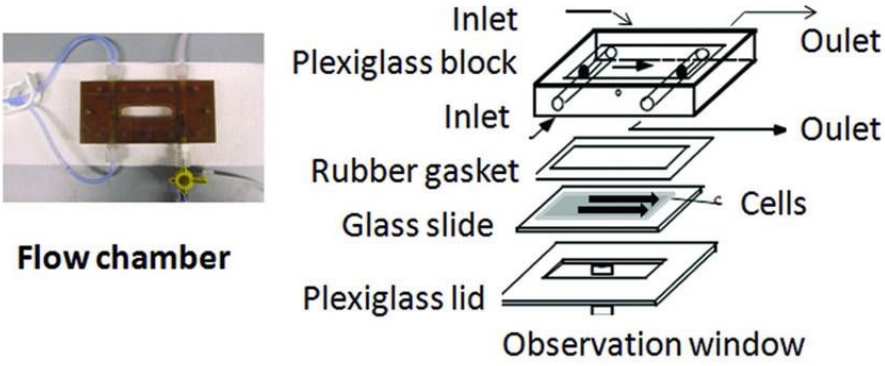

Supplemental figure 3.1 Flow chamber The flow chamber consisted of a 1mm thick borosilicate glass plate glued into the bottom of a uniformly deep groove milled into a Plexiglas block, and another glass slide with pre-seeded cells. The two plates were held together with screws and a Plexiglas lid, separated by a uniform thickness rectangular silastic spacer (McMaster). As a result, a flow chamber (5.2 cm long x 1.2cm wide x 154>m high) was created. Flow inlets and outlets were connected to cylindrical reservoirs in the Plexiglas block. A 2mm thick borosilicate glass blocked each of the cylindrical reservoirs in the middle, and separated the flows to and from the two ports. Plastic tubing (high-temperature silicone rubber soft tubing, 1.59mm ID, 3.18mm OD, McMaster) connected the inlet port to one-direction syringe pump (Harvard) and the outlet port to the waste collecting bottles.

Flow Chamber: Cell culture area 624 mm²		
L	W	H
52 mm	12 mm	0.154 mm
Flow Rate: Q	Shear Stress: τ	Reynolds: Re
8 µl/min x 2	5.6 mPa	0.044
4 µl/min x 2	2.8 mPa	0.022

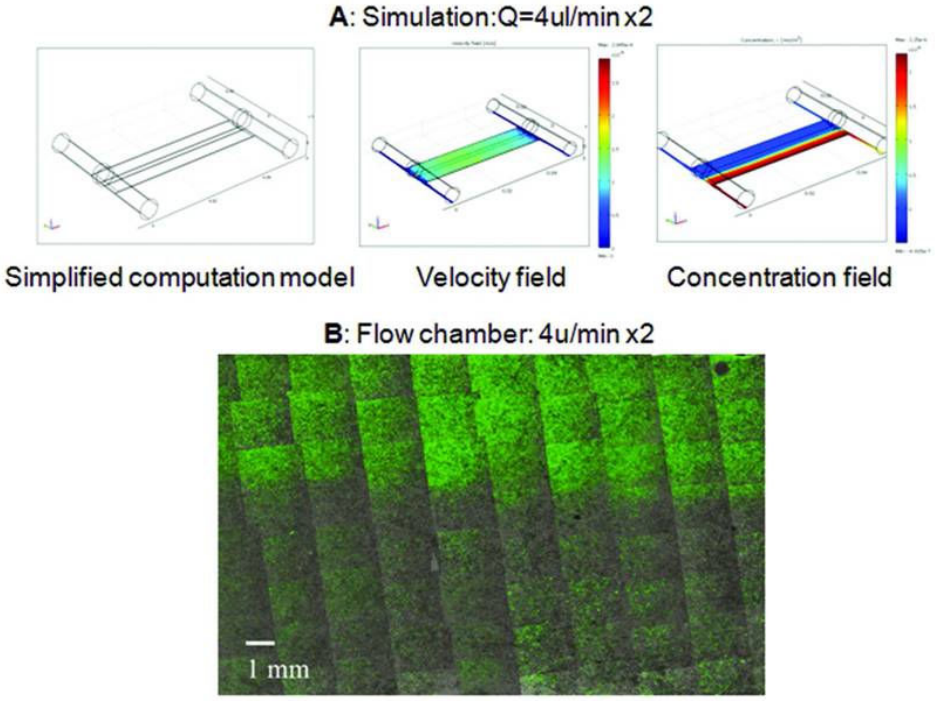

Supplemental figure 3.2 Characterization of flow chamber (A) Simplified flow models, the steady-state velocity and concentration profiles are shown for the flow channel at flow rate of 4µl/min x2. Data were calculated for the diffusion coefficient $D_{Dox}=3.93x10^{-6}cm^2/s$, fluid viscosity $v=10^{-3}Pa*s$, fluid density $\rho=10^3kg/m^3$, and inlet concentrations C_{Dox}=1ng/ml= $2.25x10^{-12}$mol/ml and C_{Dox}=0ng/ml=0. **(B)** Separation of Calcein stain in the flow channel at the flow rates of 4µl/min x2. Data are for the diffusion coefficient of Calcein $DCalcein=2.6*10^{-6}cm^2/s$, and inlet concentrations of Calcein C+=2µM and C-=0, diffusion coefficient of Flow direction is left to right. Original magnification: 100X. Scale bar: 1mm.

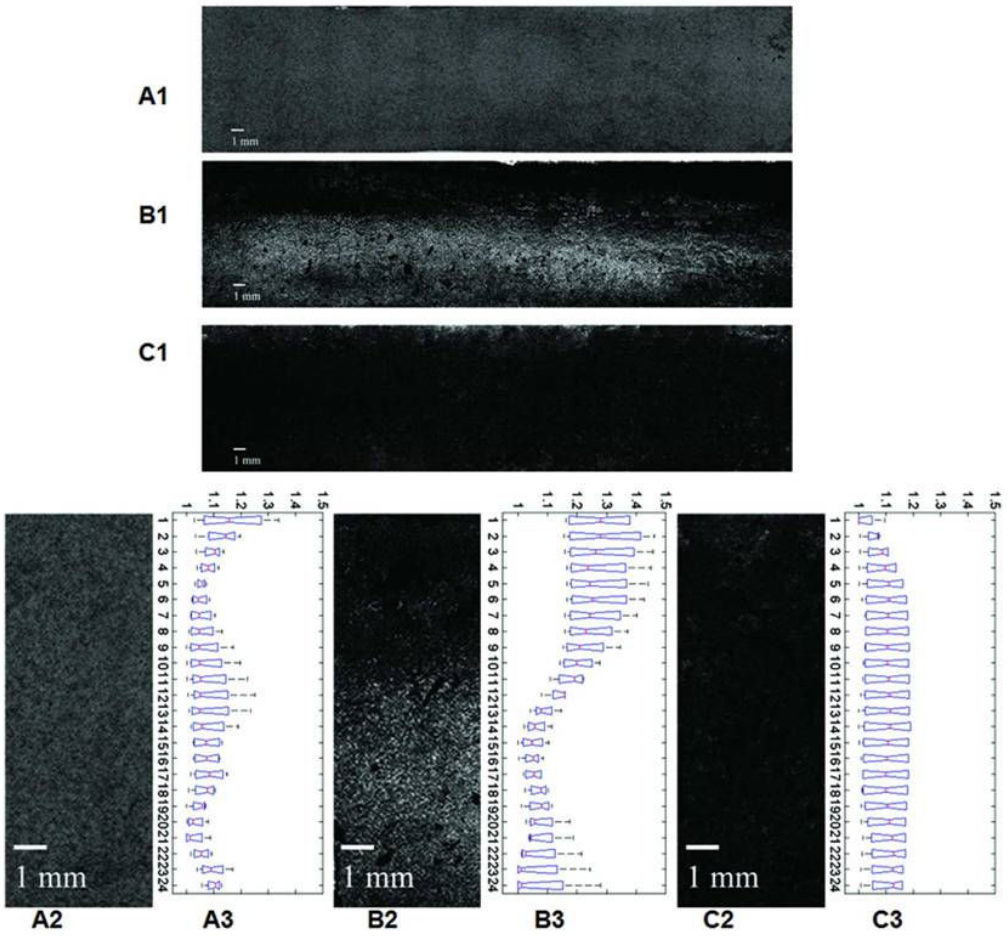

Supplemental figure 3.3 Dox dependent osteogenic differentiation in flow chamber C9 cells were cultured in osteogenic differentiation medium in a perfused flow chamber, at a flow rate of 4µl/min x2, for 3 weeks. Images show von Kossa staining of calcium deposition for selected conditions: **(A1, A2)** Perfusion medium with Dox 1ng/ml (top) / 1ng/ml (bottom); **(B1, B2)** Perfusion medium: Dox 0ng/ml (top) / 1ng/ml (bottom); **(C1, C2)** Perfusion medium: Dox 0ng/ml (top) / 0ng/ml (bottom). **(A3, B3, C3)** Intensity of calcium staining, obtained by pooling repeated experiments (n=4 per condition). The staining of the deposited calcium is expressed at the ratio of the normalized sum of segmented (~0.25mm) image intensity and the minimum intensity along the y axis (the width) of the chamber. Data were processed using Matlab R2007 program. Flow direction: left to right. Scale bar: 1mm

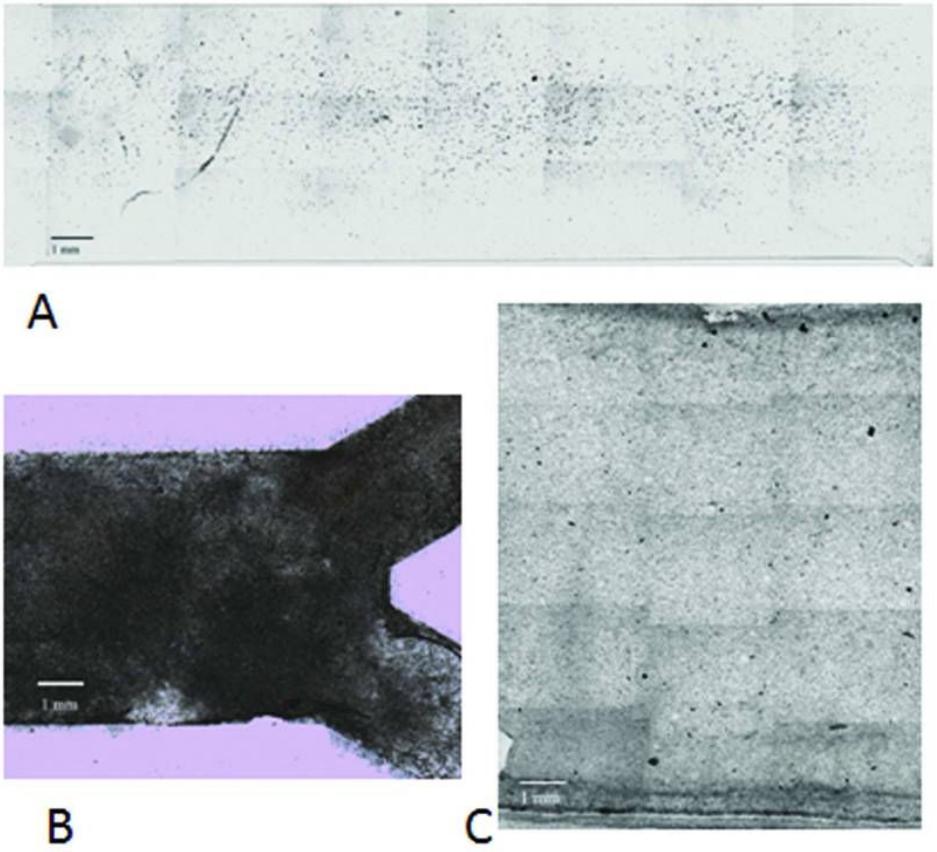

Supplemental figure 3.4 The effect of flow rate to osteogenic differentiation (A) von Kossa staining of the fluidic channel, at flow rate of 5µl/min x2. Perfusion medium: Dox 0ng/ml (top) / 1ng/ml (bottom); **(B)** von Kossa staining of the fluidic channel, at flow rate of 0.5µl/min x2. Perfusion medium: Dox 0ng/ml (top) / 0ng/ml (bottom); **(C)** von Kossa staining fragment of the fluidic chamber, at flow rate of 8µl/min x2. Perfusion medium: Dox 0ng/ml (top) / 0ng/ml (bottom).

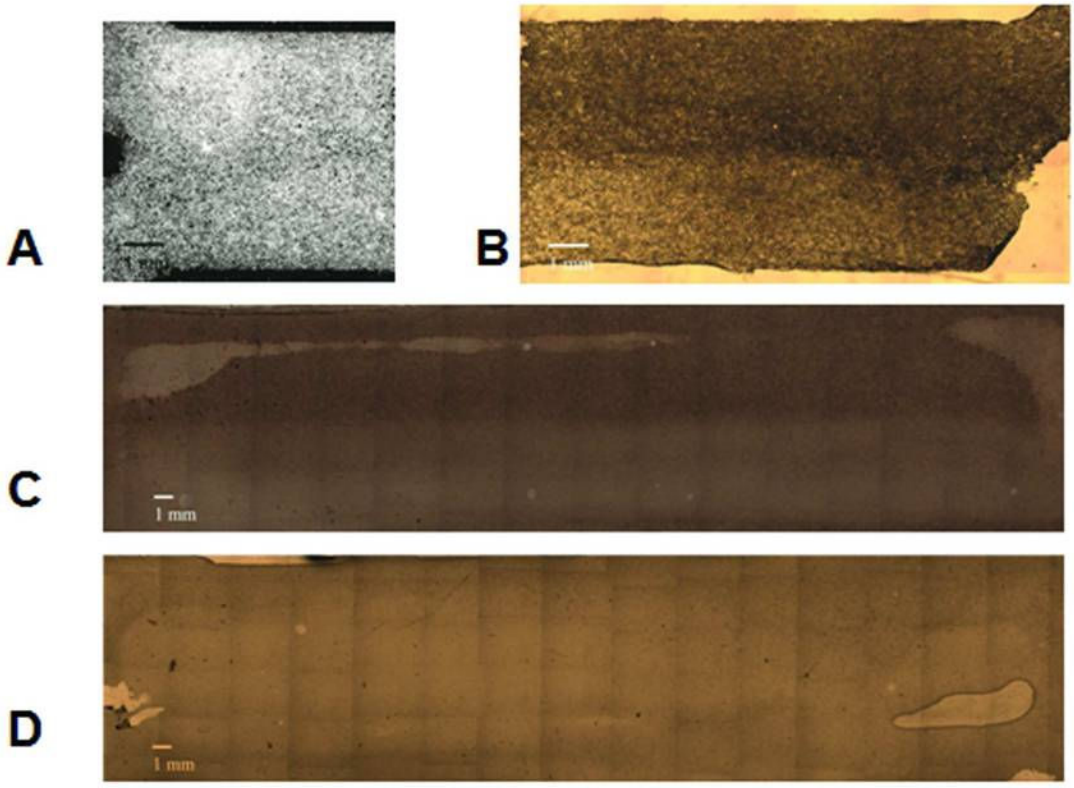

Supplemental figure 3.5 Cell distribution and BSP staining (A) Phase contrast image of cell distribution in fluidic channel after 3 weeks osteogenic differentiation at flow rate of 1µl/min x2. Perfusion medium: Dox 0ng/ml (top) / 1ng/ml (bottom). **(B)** BSP staining of the cells after 3 weeks patterned osteogenic differentiation in fluidic channel at flow rate of 1µl/min x2. Perfusion medium: Dox 0ng/ml (top) / 1ng/ml (bottom). BSP staining of the cells after 3 weeks patterned osteogenic differentiation in fluidic chamber at flow rate of 4µl/ml x2. **(C)** Perfusion medium: Dox 0ng/ml (top) /1ng/ml (bottom); **(D)** Perfusion medium: Dox 1ng/ml (top) / 1ng/ml (bottom); Flow direction: left to right.

3.8 References

1. Atkinson B, Brocklebank MP, Card CCH, Smith JM. Low Reynolds number developing flows. *AIChE J.* 15(4), 548–553, 1969.
2. Boyan BD, Lohmann CH, Somers A, Niederauer GG, Wozney JM, Dean DD, Carnes Jr DL, Schwartz Z. Potential of porous poly-D,L-lactide-*co*-glycolide particles as a carrier for recombinant human bone morphogenetic protein-2 during osteoinduction *in vivo. J. Biomed. Mater. Res.,* 46, 51–59, 1999
3. Chang CH, Lin FH, Lin CC, Chou CH, Liu HC. Cartilage tissue engineering on the surface of a novel gelatin-calcium-phosphate biphasic scaffold in a double-chamber bioreactor", *J. of Biomed. Mater. Res. B, Appl. Biomaterials*. 71(2):313-321, 2004

4. Chen G, Sato T, Tanaka J, Tateishi T. Preparation of a biphasic scaffold for osteochondral tissue engineering. *Mater. Eng., C, Biomim. Mater., Sens. Syst.,* 26, 118–123, 2006

5. Chung BG, Flanagan LA, Rhee SW, Schwartz PH, Lee AP, Monuki ES, Jeon N L. Human neural stem cell growth and differentiation in a gradient-generating microfluidic device. *Lab Chip*, 5(4), 401–406, 2005

6. Hay E, Hott EM, Graulet AM, Lomri A, Marie PJ. Effects of bone morphogenetic protein-2 on human neonatal calvaria cell differentiation. *J. Cell. Biochem.* 72, 81–93, 1999

7. Hosseinkhani H, Hosseinkhani M, Khademhosseini A, Kobayashi H. Bone regeneration through controlled release of bone morphogenetic protein-2 from 3-D tissue engineered nano-scaffold *J. Controlled Release* 117, 380–386, 2007

8. Kenis PJA, Ismagilov RF, Whitesides GM. Microfabrication Inside Capillaries Using Multiphase Laminar Flow Patterning. *Science*, 285, 83–85, 1999

9. Langer R. Drug delivery and targeting. *Nature*, 1998, 392, 5–10, 1998

10. Lee CH, Shah B, Moioli EK, Mao JJ. CTGF directs fibroblast differentiation from human mesenchymal stem/stromal cells and defines connective tissue healing in a rodent injury model. *J. Clin. Invest*. 120(9), 3340–3349, 2010

11. Li C, Vepari CH. Jin J, Kim HJ, Kaplan DL. Electrospun silk-BMP-2 scaffolds for bone tissue engineering. *Biomaterials* 27, 3115–3124, 2006

12. McCullough KA, Waits CA, Garimella R, Tague SE, Sipe JB, Anderson HC. Immunohistochemical localization of bone morphogenetic proteins (BMPs) 2, 4, 6, and 7 during induced heterotopic bone formation. *J. Orthop. Res.* 25(4), 465–472, 2007

13. Mitsuhashi Y, Mikami Y, Mikami H, Ishikawa H, Tamai K, Hashimoto I. Simultaneous and separated culture of keratinocytes and fibroblasts on each side of a collagen membrane. *J. Dermatol. Sci*., 5(1), 3–13, 1993

14. Moutsatsos IK, Turgeman G, Zhou S, Kurkalli BG, Pelled G, Tzur L, Kelley P, Stumm N, Mi S, Müller R, Zilberman Y, Gazit D. Exogenously Regulated Stem Cell-Mediated Gene Therapy for Bone Regeneration. *Mol. Ther.,* 3, 449–461, 2001

15. Nilsson O, Parker EA, Hegde A, Chau M, Barnes KM, Baron J. Gradients in bone morphogenetic protein-related gene expression across the growth plate. *J. Endocrinol*. 193(1), 75–84, 2007

16. Noël D, Gazit D, Bouquet C, Apparailly F, Bony C, Plence P, Millet V, Turgeman G, Perricaudet M, Sany J, Jorgensen C. Short-term BMP-2 expression is sufficient for in vivo osteochondral differentiation of mesenchymal stem cells. *Stem Cells* 22(1), 74–85, 2004

17. Ohyama Y, Nifuji A, Maeda Y, Amagasa T, Noda M. Spaciotemporal Association and Bone Morphogenetic Protein Regulation of Sclerostin and Osterix Expression during Embryonic Osteogenesis. *Endocrinology* 145(10), 4685–4692, 2004

18. Phillips JE, Burns KL, Le Doux JM, Guldberg RE, García AJ. Engineering graded tissue interfaces. *Proc. Natl. Acad. Sci. U. S. A.,* 105(34), 12170–12175, 2008

19. Rhee SW, Taylor AM, Tu CH, Cribbs DH, Cotman CW, Jeon NL. Patterned cell culture inside microfluidic devices. *Lab Chip*, 5(1), 102–107, 2005

20. Ruhe PQ, Kroese-Deutman HC, Wolke JG, Spauwen PH, Jansen JA. Bone inductive properties of rhBMP-2 loaded porous calcium phosphate cement implants in cranial defects in rabbits. *Biomaterials* 25, 2123–2132, 2004

21. Serls AE, Doherty S, Parvatiyar P, Wells JM, Deutsch GH. Different thresholds of fibroblast growth factors pattern the ventral foregut into liver and lung. *Development*. 132(1), 35–47, 2005

22. Shao XX, Hutmacher DW, Ho ST, Goh JC, Lee EH. Evaluation of a hybrid scaffold/cell construct in repair of high-load-bearing osteochondral defects in rabbits. *Biomaterials*, 27, 1071–1080, 2006

23. Spalazzi JP, Doty SB, Moffat KL, Levine WN, Lu HH. Development of Controlled Matrix Heterogeneity on a Triphasic Scaffold for Orthopedic Interface Tissue Engineering. *Tissue Eng*., 12, 3497–3508, 2006

24. Sweet RL, Schachter J, Landers DV, Ohm-Smith M, Robbie MO. Treatment of hospitalized patients with acute pelvic inflammatory disease: comparison of cefotetan plus doxycycline and cefoxitin plus doxycycline. *Am. J. Obstet. Gynecol.* 158(3 Pt 2), 736–741, 1988

25. Takayama S, McDonald JC, Ostuni E, Liang MN, Kenis JA, Ismagilov RF, Whitesides GM. Patterning cells and their environments using multiple laminar fluid flows in capillary networks. *Proc. Natl. Acad. Sci. U. S. A.,* 96, 5545–5548, 1999

26. Takayama S, Ostuni E, LeDuc P, Naruse K, Ingber DE, Whitesides GM. Selective Chemical Treatment of Cellular Microdomains Using Multiple Laminar Streams. *Chem. Biol*., 10(2), 123–130, 2003

27. Thomopoulos S, Williams GR, Gimbel JA, Favata M, Soslowsky LJ. Variation of biomechanical, structural, and compositional properties along the tendon to bone insertion site. *J. Orthop. Res*., 21, 413–419, 2003

28. Treier M, Gleiberman AS, O'Connell SM, Szeto DP, McMahon JA, McMahon AP, Rosenfeld MG. Multistep signaling requirements for pituitary organogenesis in vivo. *Genes Dev*. 12(11), 1691–1704, 1998

29. Tuli R, Nandi S. Li WJ, Tuli S, Huang X, Manner PA, Laquerriere P, Noth U, Hall DJ, Tuan RS. Human mesenchymal progenitor cell-based tissue engineering of a single-unit osteochondral construct. *Tissue Eng.,* 10, 1169–1179, 2004

30. Wilke CR, Chang P. Correlation of diffusion coefficients in dilute solutions *AIChE J.* 1, 264–270, 1955

31. Woo SL, Abramowitch SD, Kilger R, Liang R. Biomechanics of knee ligaments: injury, healing, and repair. *J. Biomech*. 39(1), 1–20, 2006

32. Ziauddin J, Sabatini DM. Microarrays of cells expressing defined cDNAs. *Nature*, 411(6833), 107–110, 2001

Chapter 4 Patterning embryonic cell pluripotency by inducible Nanog expression in multi-laminar fluidic system

4.1 Abstract

During native tissue development and remodeling, the differentiating cells self-organize into multicellular domains, forming boundaries and interfaces, in response to spatial gradients of signals. Deciphering how this transformation occurs and regenerating these transitional zones *in vitro* remains a significant challenge. By combining inducible gene expression with laminar flow technologies, we developed a strategy to pattern gene expression in cultured cells, along with forming gradients of soluble factors. Using Nanog safeguarded embryonic pluripotency as a model, we patterned Nanog expression, and thereby patterned early differentiation status under the exposure or withdrawal of small molecules, as evidenced by the analysis of genes and proteins. By this strategy, we successfully developed controllable differentiation – pluripotency boundaries between Nanog expressing (pluripotency) zone and Nanog suppressed (early differentiation) zone from the same population of cells, to mimic some aspects of development. By using this approach, mechanistic insights can be gained on dissecting the signaling pathways that drive multicellular patterning during embryonic and adult development.

4.2 Introduction

Embryonic stem cell (ESC) lines maintain on a long-term their self-renewal capacity and the capacity to differentiate into cells of all three germ layers. Cell fate choices are regulated by a complex orchestration of transcription factors Oct4, Sox2, Nanog as well as the LIF-gp130-Stat3, BMP-TGF-beta-Smad, MAPK-ERK, and possibly the WNT signaling pathways (Nichols et al., 1998; Niwa et al., 2000; Chambers et al., 2003; Mitsui et al., 2003; Niwa et al., 1998; Ying et al., 2003; Burdon et al., 1999; Sato et al., 2004). The spatial control of these signals and the arrangement of stem and differentiation cells lead to highly organized structure and graded tissue interface or boundaries in embryonic development, which play central role in organ development and function. Over the past few decades, evidence accumulated to support a model for the patterning of cells. This model, known as the French Flag model, describes how a signal gradient across the field is converted into gene expression domains by the concentration specific response of target genes (Wolpert, 1969). Boundaries are formed between these different gene expression domains, where interaction between these different types of cells leads to form secondary signaling centers and more sophisticated local patterns (Meinhardt, 1983). Thereby it is critical to recapitulate these tissue interfaces and boundaries in studies of native and engineered tissues.

Based on current engineering technologies, precise spatial patterns of boundaries can be achieved by laser ablation of cell borders and inactivation of

proteins (Monier et al., 2010, Landsberg et al., 2009), and by patterning the soluble and adhesive biological factors (Singh et al., 2008; Dormer et al., 2010). Only a few efforts have focused on direct patterning of gene expression at the transcriptional level, for control of downstream cellular function. In a previous study, we have developed a novel engineering strategy which for direct patterning and modulation of gene expression at transcriptional level in a two-dimensional field of cultured cells, by regulating the presence of modulators of inducible gene expression (Zhang et al., 2011). Using the inducible BMP-2 gene expression as a model, we demonstrated that a continuous, graded osteogenesis tissue interface can be established by patterning the BMP-2 gene expression, via patterning of the BMP-2 modulator doxycycline (Dox), in a simple microfluidic system.

In this study we developed a strategy to study a single genetic perturbation in hESCs (**Figure 4.1**). We used mouse ESC Nanog rescue clone (NanogR) (Ivanova et al., 2006) which is an inducible lentiviral-based complementation system. In this lentiviral system, a short hairpin RNA (shRNA) depletes endogenous Nanog mRNA, and normal levels of Nanog can be restored in a doxycycline-dependent manner for a shRNA 'immune" version (**Figure 4.1A**). As Nanog plays a central role in embryonic stem cell fate, safeguards pluripotency by reversing / resisting nascent epigenetic modification (Chambers et al., 2007; Lu et al., 2009). By patterning Nanog expression in multiple-laminar fluidic systems, we can modulate in a spatial controlled manner the stem cell self-

renewal and early commitment towards differentiation. This strategy can provide a platform to engineer and analyze the boundaries of different gene expression domains in a wide range of culture conditions, and to study how intrinsic / exogenous signals consolidate into differentiation commitment decisions.

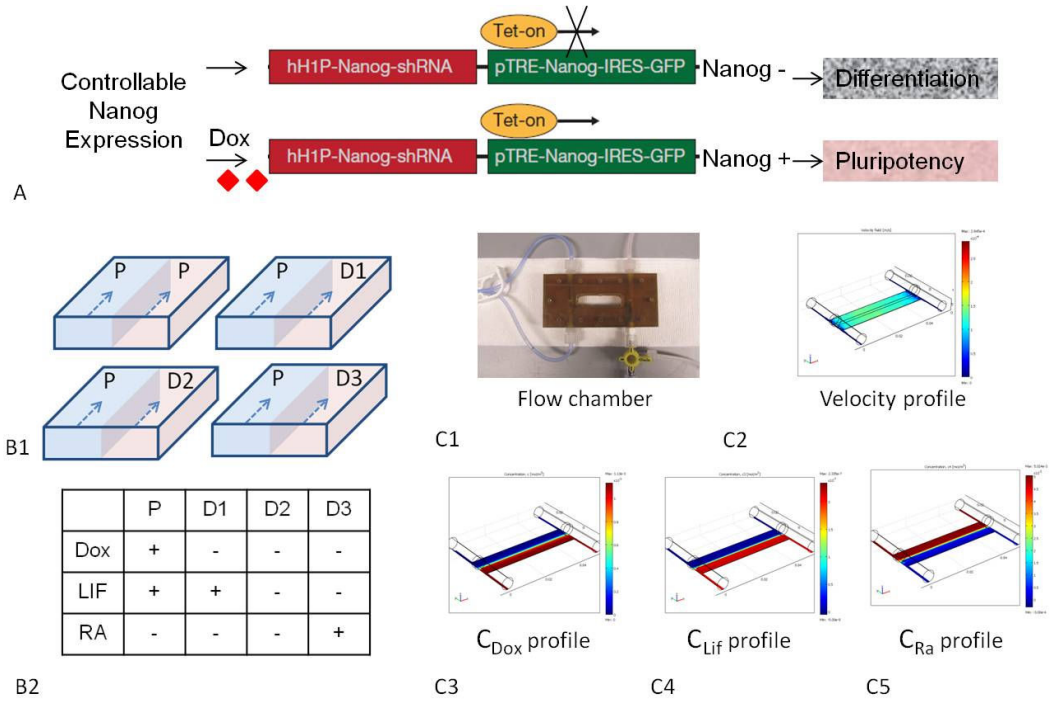

Figure 4.1 Cell model and experiment Scheme (A) Scheme of inducible Nanog expression in a Dox dependent manner. Without Dox, shRNA depletes endogenous Nanog mRNA, which leads to Nanog mediated cell differentiation in the presence of proper differentiation signals; with Dox, inducible exogenous Nanog gene expression under the control of inducible Tet-on expression system, restore the normal levels of Nanog expression. **(B1, B2)** Experiment outline: cultured NanogR cells are exposed to laminar fluidic flows with two streams (one pluripotency [P] stream contains both Dox and LIF, in align with another P stream, a differentiation [D1] stream contains LIF, a differentiation [D2] stream contains no LIF, or a differentiation [D3] stream contains RA). **(C1)** Flow chamber (main chamber: 52mm L x 12mm W x 0.154mm H). **(C2)** Simulated fluidic profiles (flow rate v=4μl x2/min) in simplified flow model. **(C3)** Simulated Dox concentration profiles at P:D1, P:D2, P:D3 conditions in steady status. **(C4)** Simulated LIF concentration profiles at P:D2, P:D3 conditions in steady status. **(C5)** Simulated RA concentration profiles at P:D3 condition in steady status. Input concentration: Dox: 500μg/ml=1.13×10^{-9}[mol/ml]; LIF: 10^3units/ml=2.13×10^{-13}[mol/ml]; RA: 5μM=5×10^{-9}[mol/ml]. Diffusion coefficient: $D_{Dox}=3.93\times10^{-6}cm^2/s$, $D_{LIF}=1.66\times10^{-6}$ cm^2/s, $D_{RA}=2.3\times10^{-6}cm^2/s$. Flow viscosity (eta=$10^{-3}$Pa*s). Fluid density (□=$10^3kg/m^3$).

First, we characterized the inducible Nanog expression in the Nanog rescue clone (NanogR) in static culture, titrated with varied differentiation conditions: (*i*) LIF supplemented mouse ESC (mESC) maintenance media, (*ii*) LIF free mESC maintenance media, and (*iii*) LIF free and Retinoic Acid (RA) supplemented. We assayed a Dox dosis respond (0ng/ml-1000ng/ml) for Nanog expression levels in all different culture conditions verified by both immunological staining and real time PCR. The Dox concentration depended Nanog expression lead to Nanog concentration depended differentiation, verified by alkaline phosphatase (AP) staining and gene expression analysis. Then in the flow experiments, we successfully patterned the pluirpotency zone with sustained Nanog expression in alignment with different differentiation zones by patterning Dox / LIF / RA in the fluidic system. We demonstrated the pattern of pluripotency and differentiation can be achieved in the same population of cells at an individual colony level.

4.3 Materials and Methods

4.3.1 Embryonic stem cell culture and differentiation

The murine Nanog inducible expression mESC cell line (NanogR) was developed from mouse embryonic stem cell line Aniv15 that contains the transactivator (rtTA, TetOn) by infection with the lentiviral that contains a Nanog short hairpin RNA (shRNA), which depletes endogenous Nanog mRNA, and under the control of inducible Tet-on expression system is cloned the coding region of the genes, which can restore the normal levels of Nanog expression in a doxycycline dependent manner without effect of the shRNA (Ivanova et al., 2006).

The NanogR cells were maintained on primary mouse irradiated embryonic fibroblasts (pMEFs) in the DMEM media supplemented with 15% FBS (Hyclone), 100 mM MEM nonessential amino acids, 0.1 mM 2-mercaptoethanol, 1 mM L-glutamine (Invitrogen), 100 U/ml penicillin, 100mg/ml streptomycin, 1 mM sodium pyruvate and 10^3 units/ml of LIF (Chemicon). For experiment assays, NanogR cells were cultured on 0.1% gelatin-coated tissue culture plates without pMEFs. To induce differentiation, we withdrew doxycycline (1 μg ml^{-1}) from the media, and maintained cells in LIF containing, LIF free, or LIF free plus Retinoic Acid (5μM) media. All cell cultures were maintained at 37ºC with 5% CO_2.

4.3.2 Alkaline phosphatase staining

Alkaline phosphatase (AP) activity was measured using a commercial detection kit (Sigma-Aldrich). The cultured cells were fixed in 4% paraformaldehyde in PBS for 2 minutes. After washed with TBST (20mM Tris-HCL, pH7.4, 0.15M NaCl, 0.05% Tween-20), the fixed cells were immersed into alkaline-dye mixture consisting of fast red violate, Napthol phosphate solution and water in 2:1:1 ratio, for 20minutes in darkness (or 7 minutes when staining flow experiment samples), and were washed in TBST again. ALP staining images was captured by microscope (Olympus IX81, Center Valley PA).

4.3.3 Real-Time (RT) PCR

For gene expression analysis, total RNA was TRIzol® -extracted (Invitrogen), column-purified with RNeasy kit (Qiagen). Total RNA (1μg) was reverse

transcribed using high capacity reverse transcription kit (Applied Biosystems). All quantitative PCR analyses were performed using the Fast SYBR® Green Master Mix (Applied Biosystems) following manufacturers' protocol on the LightCycler480 Real-Time PCR System (Roche). Each PCR reaction generated a specific amplicon, as demonstrated by melting-temperature profiles of final products (Dissociation Curve analysis). No PCR products were observed in the absence of template. In gene expression analysis, all data were normalized to beta-actin. Gene-specific primers used for amplification are listed in **Supplemental Table 4.1**.

4.3.4 Immunofluorescent staining

Cells cultured at different Doxycycline concentrations and at the respective days 0, 1, 3 and 5 were rinsed twice with PBS, fixed with 4% paraformaldehyde in PBS 1X for 20 min at room temperature, quenched with 0.2M glycine in PBS 1X for 10 min, permeabilized with PBS containing 0.5% Triton X-100 for 30 min. Nonspecific sites were blocked by incubation with PBS containing 0.1% BSA for 30min at room temperature. Cells were then incubated with the specific primary antibodies: 1:100 anti-mouse Oct4 (Santa Cruz), or 1:150 anti-mouse Nanog (Cosmo Bio), diluted in PBS 1X containing 0.2% Triton X-100 and 0.1% of BSA for overnight incubation at 4 degree. After that, cells were incubated with one of the following secondary antibodies: Alexa Fluor® 546 donkey anti-goat (Invitrogen) (1:1000 dilution) and Alexa Fluor® 488 donkey anti-rabbit IgG (Invitrogen) (1:1000 dilutions). After washing with PBS 1X containing 0.2% Triton

X-100 for 3 times, the samples were incubated for 5 minutes with 1:1000 DAPI in water, followed by wash with PBS 1X containing 0.2% Triton X-100 for 3 times. We observed the complete loss of GFP three days after fixation (**Supplemental Figure 4.1**), to avoid GFP signal contamination in immune-fluorescence staining, the staining was completed and fluorescence images were captured three days after fixation with a Nikon Eclipse TE 2000-U or Olympus BX41 fluorescent microscope.

4.3.5 Design and manufacture of the microfluidic systems

4.3.5.1 Flow chamber

The flow chamber (**Figure 4.1**) consists of a 1mm thick borosilicate glass plate glued into the bottom of a uniform depth groove milled into a Plexiglas block and another glass slide with pre-seeded cells. The two plates are brought together with screws and a Plexiglas lid, separated by a uniform thickness rectangular silastic spacer (McMaster) creating a flow chamber which is 5.2 cm, 1.2 cm, 154μm (length, width, and height or gap distance). Flow enters / exits the chamber from two ports of the cylindrical reservoirs into/out of the Plexiglas block. A 2mm thick borosilicate glass blocks each of the cylindrical reservoirs in the middle, which separate the flows from /to two ports. Plastic tubing (high-temperature silicone rubber tubing soft, 1/16" ID, 1/8" OD, McMaster) connected the entrance port to the one direction syringe pump and the exit port to the waste collecting bottles.

4.3.5.2 Flow experiments

The composites of flow chamber and tubing were sterilized separately by autoclave or 70% ethanol immersion or UV exposure overnight. The sterilized plastic slide was coated with 0.1% gelatin for more than 4 hours, and then dried in the air. NanogR cells were then seeded into the slide at density of 5000 cells/cm^2 in LIF free Dox free ESC media and then incubated at 37°C in a 5% CO_2 atmosphere humidified incubator overnight. Prior to the experiment, the flow chamber was assembled and connected to a syringe pump with tubing filled with proper medium, the output ports were connected to waste container. For dye separation experiments, cells were subjected to continuous flow of medium with 2μM Calcein-AM for 30- 60minutes, then 10-30minutes continuous flow of complete medium.

4.3.6 Mathematical Model

4.3.6.1 Velocity and shear stress profiles

The chamber geometry permits the wall shear stress acting at the chamber wall to be calculated as a function of the laminar flow rate, which is in turn controlled by a mechanical single-pass syringe pump and fluid viscosity.

Shear Stress: $$\tau_w = \frac{6\mu Q}{wh^2} \quad (1)$$

Reynolds number: $$R_e = \frac{2Q}{\frac{\mu}{\rho}(w+h)} \quad (2)$$

where μ, ρ are the viscosity, density of the fluid; Q is flow rate; w and h are the width and height of the channel / chamber. The hydrodynamic development

length L in a channel of height h can be estimated from the relation (Atkinson etla., 1969):

$$\frac{L}{h} = 0.3125 + 0.011R_e \qquad (3)$$

4.3.6.2 Computational scheme

Computational fluid model was used to simulate the concentration and velocity profiles using the finite element method (COMSOL Multiphysics v3.2, Burlington, MA). The concentration gradient generation driven by the syringe pump was based on the following three equations, including the 3D incompressible Navier–Stokes equations:

$$\rho\left(\frac{\mathrm{d}u}{\mathrm{d}t} + (u\nabla u)\right) = -\nabla p + \mu\nabla^2 u \qquad (4)$$

$$\nabla u = 0 \qquad (5)$$

And the convection-diffusion transport equation

$$\frac{\mathrm{d}c}{\mathrm{d}t} + (u\nabla)C = D\nabla^2 CX \qquad (6)$$

where ρ, u, and p are the density, flow velocity and pressure of the liquid, and *C* and D are the concentration and diffusivity of the molecules in the liquid. At each time step, the flow velocity was first obtained, independently of the concentration, which was then calculated based on fluid flow field. The boundary conditions were as follows: specified flow velocity qt the inlet, zero normal stress at the outlet and no-slip conditions on the channel walls. For the convection–diffusion

equation, a constant concentration was set at the channel inlet. No-flux conditions were imposed at all channel walls.

4.3.7 Image analysis

Sequential images were acquired with a phase-inverted microscope (Olympus IX81), stored, assembled, and analyzed digitally by Photoshop CS4 program (Adobe). For the quantitative analysis of immune-fluorescent staining, the assembled color images were converted to black-white images. The integrated staining intensity was quantified with Matlab R2007 program (Matlab, Natick, MA) by normalized sum) of segmented image (0.5mm) intensity moving lengthwise along the y axis (the width) of the chamber images.

4.3.8 Statistics/Data Analysis

Experimental results were expressed as mean ± standard deviation (SD) . All the collected data were analyzed by ANOVA for multiple comparisons, and statistical significance was accepted at $P<0.05$.

4.4 Results

4.4.1 Regulation of Nanog expression and embryonic pluripotency in genetically modified embryonic stem cells in static culture

We first characterized the Dox dependent Nanog expression and embryonic stem cell differentiation in varied static culture conditions, with a series of Dox concentrations (0ng/ml to 1000ng/ml) over 5 days of culture (**Figure 4.2,**

Supplemental Figure 4.2, 4.3, 4.4). The NanogR cells grown in static culture were shown to have secretion of exogenous Nanog, when Dox concentration in medium was higher than 100ng/ml, while the endogenous Nanog was constantly suppressed (data not shown). The amount of Nanog expression measured by immuno-fluorescence staining and RT-PCR was positively corelated to the concentration of Dox, and reached a maximum when Dox was 1000ng/ml.

Dox induced Nanog expression, which in turn induced Dox concentration dependent early embryonic differentiation of NanogR cells, as shown by alkaline phosphatase (AP) analysis, Immunofluorescent staining of Oct 4 and RT-PCR analysis of varied pluripotency and early lineage differentiation markers. When cultured in mESC media supplemented with LIF, the Dox concentration mediated change of Nanog expression, did not induce specific differentiation (**Figure 4.2, Supplemental Figure 4.2**).

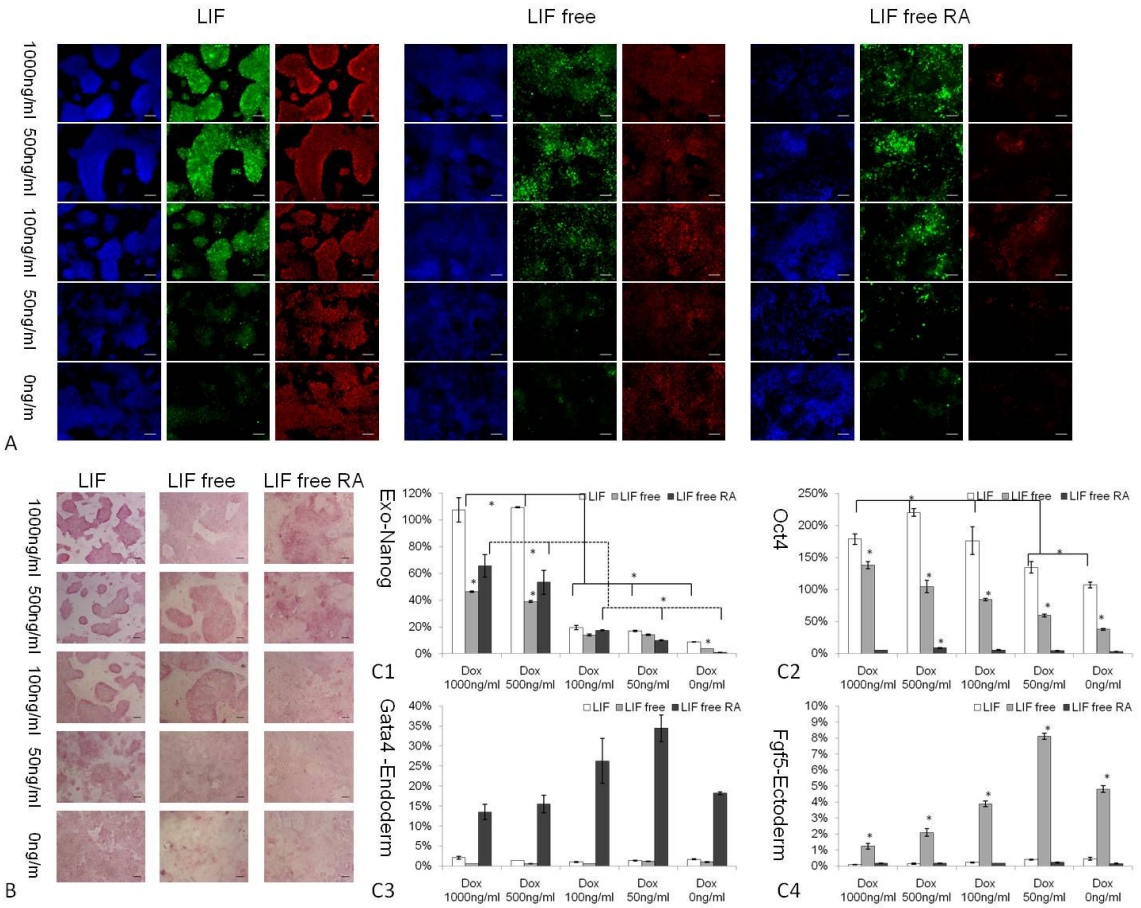

Figure 4.2 Titration of Dox concentration in NanogR cells (A) Immunofluorescent staining of NanogR cells at Day 3 (blue: DAPI; green: Nanog; red: Oct4). **(B)** AP staining of the NanogR cells at Day 3. (**C1-C4**): RT-PCR measurement of Exogenous Nanog, Oct4, Gata4 and Fgf5 at Day3. *p<0.05. Scale bar: 100μm.

The expression of the pluripotent marker Oct4 was sustained through the culture period, even when Nanog expression was suppressed by Dox removal. We observed decreases in Oct4 expression (by RT-PCR) and AP staining when Dox concentration was < 100ng/ml. Expression of endoderm/ectoderm/mesoderm differentiation markers was not detected (RT-PCR). These results suggested that the suppression of Nanog expression in culture media supplemented with LIF might lead to the activation of compensatory mechanisms to recover the

pluirpotent state. Therefore, downregulation of Nanog alone was not sufficient to induce cell differentiation.

When LIF was removed from the ESC culture media (**Figure 4.2, Supplemental Figure 4.3**), we observed a decrease of AP (staining), and Oct4 expression (RT-PCR) and increase of Fgf5 expression, suggesting early stage of ectoderm differentiation. No other differentiation markers were detected. When a stronger differentiation factor, RA, was added to the LIF-free ESC culture system, we observed further degree of differentiation, the loss of Oct4 expression and AP staining markers even with the presence of Nanog expression (**Figure** 4.**2, Supplemental Figure 4.4**). We also observed a significant increase of endoderm differentiation marker, Gata4, but no increase of Fgf5 associated with the decrease Dox concentration, suggesting RA suppression of early ectodermal differentiation, and enhancement of endodermal differentiation.

In summary, static culture demonstrated the correlation between Dox concentration and Dox induced Nanog expression, and Nanog mediated embryonic differentiation under varied culture conditions. The NanogR cells had clear “cutoff” of Nanog expression and Nanog mediated differentiation at Dox concentration of 500ng/ml. Therefore, in flow experiments, we used bi-laminar flows of medium containing C_{Dox}=500ng/ml and C_{Dox}=0ng/ml to pattern embryonic differentiation within the same cell population.

4.4.2 Characterization of the fluidic chamber

Using COMSOL Multiphysics®, the velocity profiles and concentration profiles in the flow chamber were analyzed in detail. The flow rates of 2 x 4µl/min corresponded to the Reynolds number Re=0.022 and the hydrodynamic development length of 48 µm in the fluidic chamber. Thus, the flow in each system may be considered as fully developed, with negligible variation in the direction transverse to the flow. The wall shear stress in the cell culture zone was 2.8mPa for fluidic chamber, well under the values of shear stress of cells exposed to normal interstitial (Wang and Tarbell, 1995) or blood flow (Serls et al., 2005). Simplified fluidic models were developed to study the simulated fluidic profiles and concentration profiles at steady state (**Figure 4.1**). Different concentration profiles of Dox, LIF, and RA were simulated, to show that the bi-laminar-fluidic system permits the alignment of flows with different concentration profiles, creating a concentration interface.

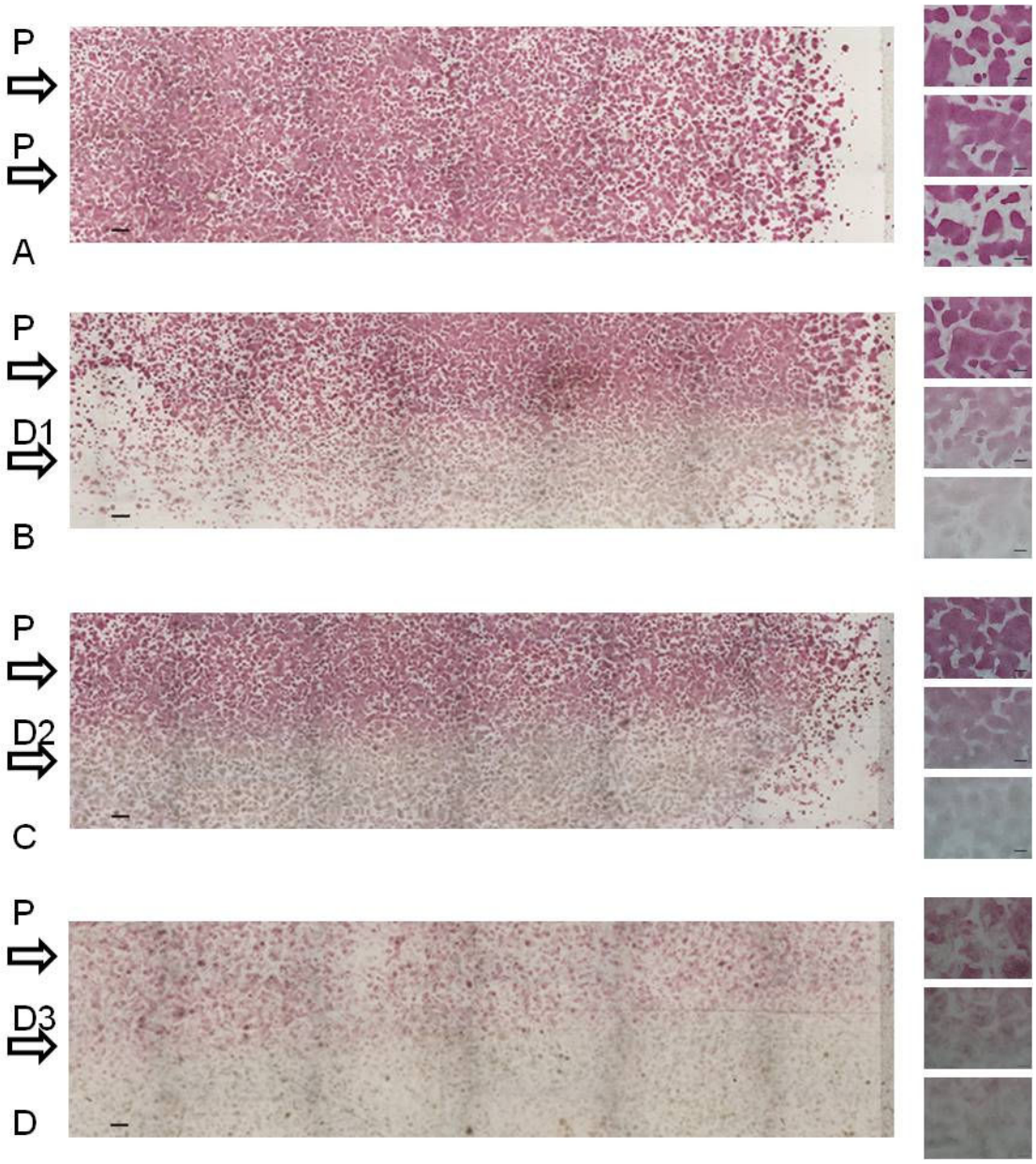

Figure 4.3 AP staining of flow chamber at Day3 (A) Perfusion media: top, P (Dox: 500μg/ml; LIF: 10^3units/ml); bottom, P. **(B)** Perfusion media: top, P; bottom, D1 (LIF: 10^3units/ml). **(C)** Perfusion media: top, P; bottom, D2 (LIF free). **(D)** Perfusion media: top, P; bottom, D3 (LIF free, RA: 5μM). Flow direction: from left to right. Scale bar: 1mm (Left), 100μm (Right). All the staining images were taken after 7 minutes incubation of alkaline dye mixture.

4.4.3 Patterning of embryonic pluripotency

In flow experiments, we generated patterned pluripotency (P) and differentiation (D) zones within a single flow chamber, by patterning the flow streams the cells

were exposed to. In the control experiment (P: P), we aligned two pluripotency streams (P) containing Dox and LIF supplemented mESC media together (**Figure 4.3A, Figure 4.4**). Consistent with the characterization result of static culture, we observed uniform staining of AP, Nanog and Oct4 across the flow chambers. The flow did not significantly affect the expression Nanog and Oct4.

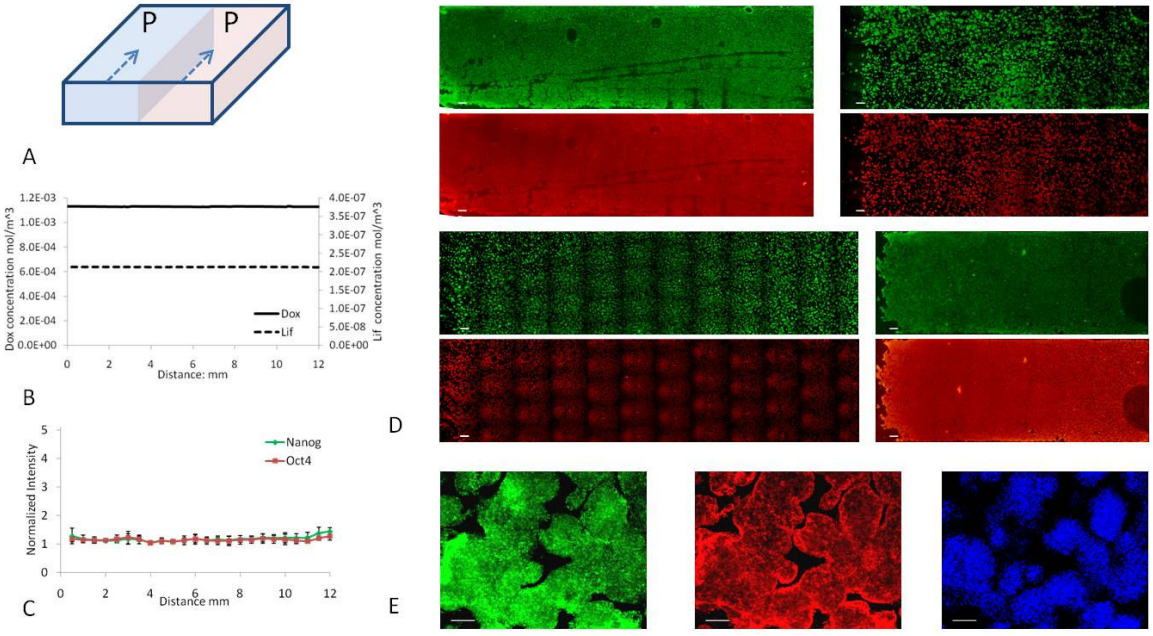

Figure 4.4 Immunofluorescent staining of flow experiment (P: P) (A) Experiment model: cultured NanogR cells were exposed to laminar fluidic flows with two [P] streams. **(B)** Simulated Dox and LIF concentration profiles at the beginning of the flow chamber in steady status. **(C)** Normalized immunofluorescent Nanog / Oct4 staining intensity across the flow chamber in y direction, n=4. **(D)** Immunofluorescent staining of the flow chambers. Scale bar: 1mm. **(E)** Immunofluorescent staining of selected colonies in flow chamber. Scale bar: 100μm. (Green: Nanog; Red: Oct4, Blue: DAPI)

We then aligned the pluripotency stream (P) containing Dox and LIF supplemented mESC media with differentiation stream1 (D1) containing only LIF supplemented mESC media, or differentiation stream 2 (D2) containing no Dox and no LIF supplemented mESC media within flow chamber. Therefore, by

patterning Dox and LIF distribution across the flow chamber, we successfully developed patterned Nanog expression from the same population of cells cultured in the flow chamber. By AP staining and immune-fluorescent staining we did not see significant impact by modulation of LIF concentration across the flow chamber. Both experiments exhibited patterned AP staining according to Dox concentration profiles within a short period of incubation (**Figure 4.3B, 4.3C**), suggesting different AP activities modulated by Dox concentration dependent Nanog expression. In both experiments, we observed patterned Nanog staining across the flow chambers (**Figure 4.5, 4.6**).

By pooling different individual staining result, and quantifying the normalized intensity of Nanog / Oct4 staining in direction perpendicular to flow direction, we observed a gradual decrease in the Nanog staining across the pluripotency and differentiation interface, matching the simulated concentration profiles of Dox in each experiment (**Figure 4.5B, 4.5C, 4.6B, 4.6C**). We also observed relatively uniform expression of Oct4 across the pluripotency (P) and differentiation zones (D1, D2) in the flow chamber, suggesting that the suppression of Nanog expression, and removal of LIF were not sufficient to induce celldiff erentiation. Fluorescent images in higher magnitudes demonstrated the patterned Nanog expression (**Figure 4.5E, Figure 4.6E**).

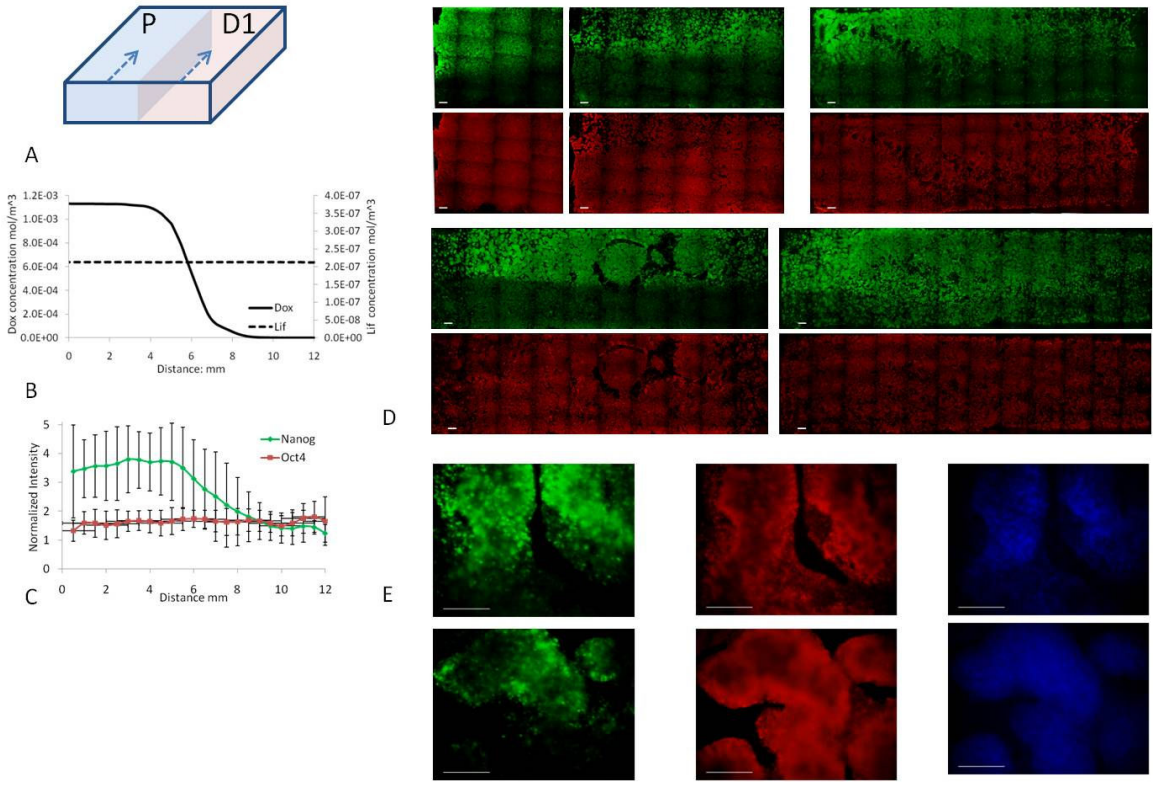

Figure 4.5 Immunofluorescent staining of flow experiment (P: D1) (A) Experiment model: cultured NanogR cells were exposed to laminar fluidic flows with one stream of [P] in align with another stream of [D1]. **(B)** Simulated Dox and LIF concentration profiles at the beginning of the flow chamber in steady status. **(C)** Normalized immunofluorescent Nanog / Oct4 staining intensity across the flow chamber in y direction, n=5. **(D)** Immunofluorescent staining of the flow chambers. Scale bar: 1mm. **(E)** Immunofluorescent staining of selected colonies in flow chamber. Scale bar: 100μm. (Green: Nanog; Red: Oct4, Blue: DAPI)

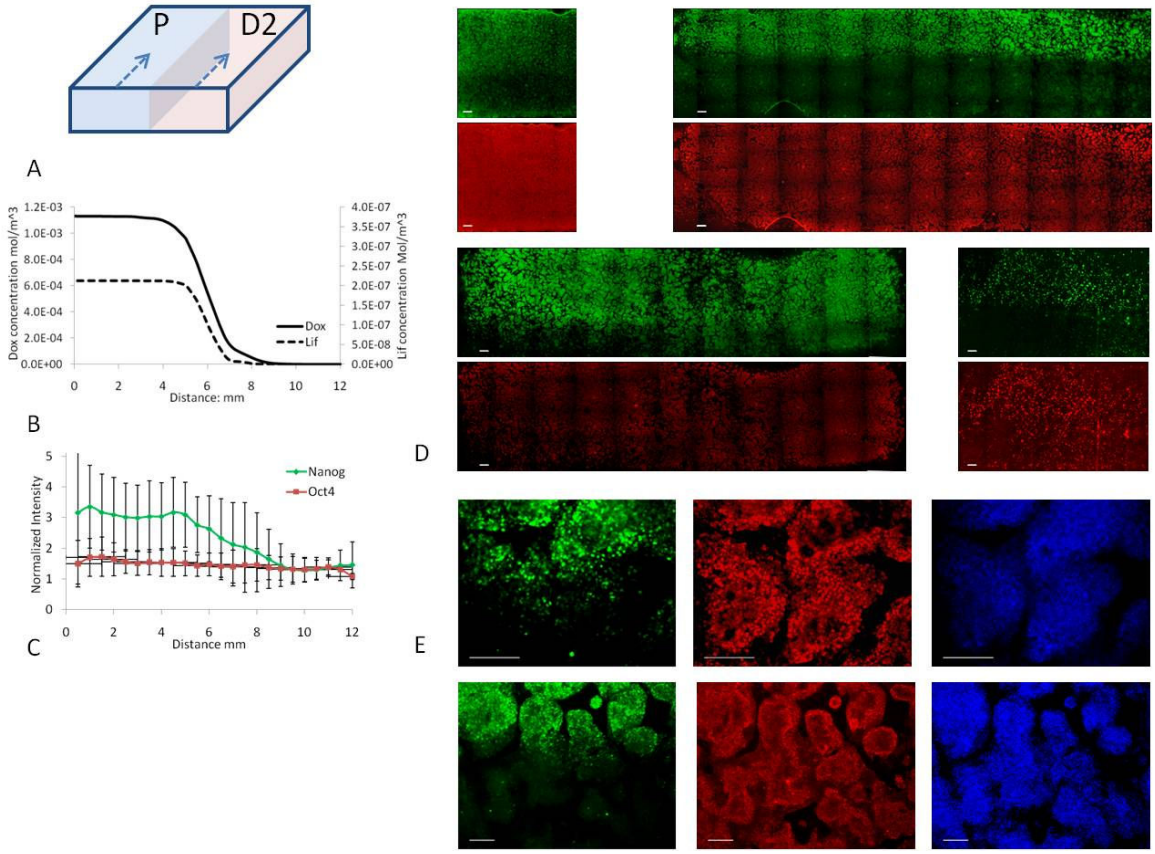

Figure 4.6 Immunofluorescent staining of flow experiment (P: D2) (A) Experiment model: cultured NanogR cells were exposed to laminar fluidic flows with one stream of [P] in align with another stream of [D2]. **(B)** Simulated Dox and LIF concentration profiles at the beginning of the flow chamber in steady status. **(C)** Normalized immunofluorescent Nanog / Oct4 staining intensity across the flow chamber in y direction, n=4. **(D)** Immunofluorescent staining of the flow chambers. Scale bar: 1mm. **(E)** Immunofluorescent staining of selected colonies in flow chamber. Scale bar: 100μm. (Green: Nanog; Red: Oct4, Blue: DAPI)

In the last experimental group (P: D3), we aligned the pluirpotency stream (P) containing Dox and LIF supplemented mESC media with differentiation stream3 (D3) containing no Dox and no LIF but RA supplemented mESC media within flow chamber. The AP staining exhibited patterned staining intensity according the patterned P stream and D3 stream. However, we also observed a significant decrease of AP staining intensity in the area exposed to pluripotent culture

medium supplemented with Dox and LIF. This was probably caused by either diffusion of RA, or interaction with cell differentiation zone (**Figure 4.3D**).

The immune-fluorescent staining and quantified staining intensity from individual experiment showed clear patterned Nanog staining as well as Oct4 staining across the pluripotency and differentiation interface, consistent with simulated concentration profiles of Dox, LIF and RA (**Figure 4.7**). The parallel DAPI staining showed that the differences in staining intensity of Nanog and Oct4 were not caused by uneven distribution of cell population. Fluorescent images in higher magnitudes demonstrated the generation of patterned Nanog and Oct4 expression within a single colony (**Figure 4.7E**, top), along with the gradual change of morphology from aggregated cell population with clear edge to a flatter and more diffusive cell population. Similar patterns of Nanog and Oct4 expression and morphology was also observed at inter colonies level (**Figure 4.7E, bottom**). In summary, by using bi-laminar flow system, we successfully patterned zonal organization of Es cell pluripotency and differentiation by patterning Dox mediated Nanog expression, and concurrent application of LIF and RA.

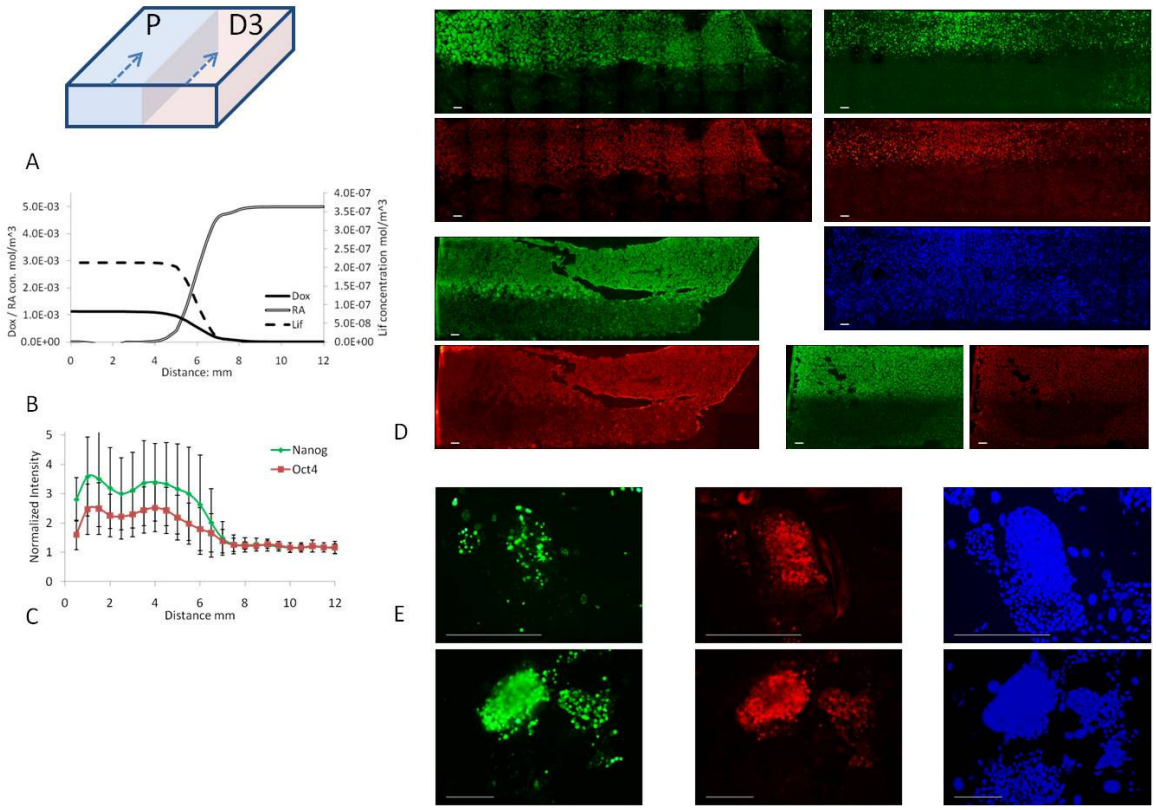

Figure 4.7 Immunofluorescent staining of flow experiment (P: D3) (A) Experiment model: cultured NanogR cells were exposed to laminar fluidic flows with one stream of [P] in align with another stream of [D3]. **(B)** Simulated Dox, LIF and RA concentration profiles at the beginning of the flow chamber in steady status. **(C)** Normalized immunofluorescent Nanog / Oct4 staining intensity across the flow chamber in y direction, n=4. **(D)** Immunofluorescent staining of the flow chambers. Scale bar: 1mm. (**E**) Immunofluorescent staining of selected colonies in flow chamber. Scale bar: 100μm. (Green: Nanog; Red: Oct4, Blue: DAPI)

4.5 Discussion

We used a simple bi-laminar fluidic system to pattern stem cells pluripotency at transcriptional level, and to generate boundaries between different gene expression domains within the same cell population. The patterning of stem cells pluripotency was engineered by patterned distribution of the modulator of inducible Nanog expression vector, Dox, along with patterned delivery of LIF and RA factors in the laminar fluidic chamber. Using this strategy, we successfully

patterned the Nanog expressing pluripotent zone in alignment with varied Nanog-suppressed differentiation zones with increased strength of differentiation signals: D1, suppressed Nanog expression only; D2: suppressed Nanog expression and removal of pluripotency maintenance factor, LIF; D3: suppressed Nanog expression, removal of LIF and addition of differentiation factor, RA.

Consistent with previous studies, we found the down-regulation of Nanog predisposed cells towards differentiation but did not necessary mark definitive commitment (Chamber et al., 2007). Only when the suppression of intrinsic Nanog expression met proper exogenous differentiation signals, as for example the removal of LIF and addition of RA, the signals consolidated into stem cell differentiation commitment. Using this strategy, from a single colony, we can observe the generation of pluripotency – differentiation boundaries with zonal organization of Nanog and Oct4 expression, as well as the gradual change of colony morphology, in which cells gradually changed their tightly packed adherent morphology to a more spread-out morphology.

This strategy of patterning the expression of key master regulator genes within tissues mimics some mechanisms of the development that underlie patterned differentiation in which molecular signals and networks orchestrate the development. Cells instructed by these signals ultimately form the remarkable multicellular patterns and structures associated with development. In most cases, developmental signals, particularly the expression of a particular gene, have

been correlated to a specific cellular fate or behavior and thus serve as markers of cell response. A major challenge is to elucidate the mechanistic relation between these molecular developmental markers and cell response. This transcriptional patterning strategy may help develop future mechanistic models that predict not only the spatiotemporal evolution of developmental signals but also the cellular rearrangements and turnover as development progresses.

This study results in a useful platform to study the boundaries between gene expression domains, which is central to the understanding of development. Within this system, non-lineage boundaries could be established, maintained or reiterated to mimic the natural development process, where cell can move across gene expression boundaries and adapt their fate to that of their local neighbors. This non-lineage boundary is common in development process; examples include the boundary between the wing and the notum in Drosophila melangaster (Mann and Morata, 2000), and in vertebrate embryos the boundaries between the foregut and hindgut (Tremblay and Zaret, 2005) and between the somites (Kulesa and Fraser, 2002; Dahmann et al., 2011; Alexander et al., 2009). The system also allows short range cross talk between the boundaries, enabling the study of short range juxtacrine specification of cell fate, as well the study of long range induction by patterning specific gene expression or morphogen factors. In addition, the system could be used to analyze lineage boundaries, where the boundary is inherited and does not require higher order signaling inputs.

The fluidic chamber offers significant flexibility compared to other microfluidic systems. It allows the cells to be attached to various substrates and to be micro-patterned before the chamber assembly, which can provide better control of cell seeding and distribution, a feature suitable to a variety of cell culture applications. After the flow experiment, the substrates can be easily disassembled; samples at specific sites can be collected or fixed for variety of staining and molecular assays, providing more systematic analysis of the boundaries engineered.

4.6 Conclusion

In summary, we demonstrate that continuous, graded pluripotency-differentiation boundaries can be established by patterning the Nanog gene expression along with other exogenous signaling factors via a simple laminar-fluidic system. This approach provides an innovative model to pattern cellular function at transcriptional level, engineer boundaries of different gene expression domains, and study how a gradient of gene expression can modulate cell fate and function.

4.7 Supplemental Information

Gene	Accesion Number	5' Primer	3'Primer
Nanog exo	XM_132755,XP_132755	CTGCTCCGCTCCATAACTTC	GCTTCCAAATTCACCTCCAA
Nanog endo	XM_132755,XP_132755	CCTGGCCTTGAACTCAGAGA	GGTGCCCAGCATGTTCTAAG
Oct3/4	NM_013633	GCAGGAGCACGAGTGGAAAGCAAC	CAAGGCCTCGAAGCGACAGATG
Gata4	NM_008092	TTCCTGCTCGGACTTGGGAC	TTCCCAGGCAGGTGGAGAATAAG
Fgf5	NM_010203	CTGTATGGACCCACAGGGAGTAAC	ATTAAGCTCCTGGGTCGCAAG
Brachury	NM_009309	CTCTAATGTCCTCCCTTGTTGCC	TGCAGATTGTCTTTGGCTACTTTG
Goosecoid	NM_010351	CAGATGCTGCCCTACATGAAC	TCTGGGTACTTCGTCTCCTGG
Cdx2	NM_007673	CCTGCGACAAGGGCTTGTTTAG	TCCCGACTTCCCTTCACCATAC
Beta actin	NM_007393	ACCAACTGGGACGACATGGAGAAG	TACGACCAGAGGCATACAGGGACA
GAPDH	NM_001001303	TCCCACTCTTCCACCTTCGATGC	GGGTCTGGGATGGAAATTGTGAGG

Supplemental Table 4.1 Table of oligos used for quantitative qPCR analysis

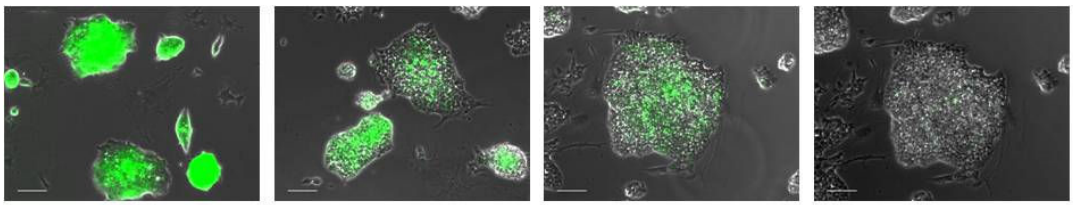

Supplemental Figure 4.1 Decrease in GFP intensity after fixation. Scale bar: 100μm.

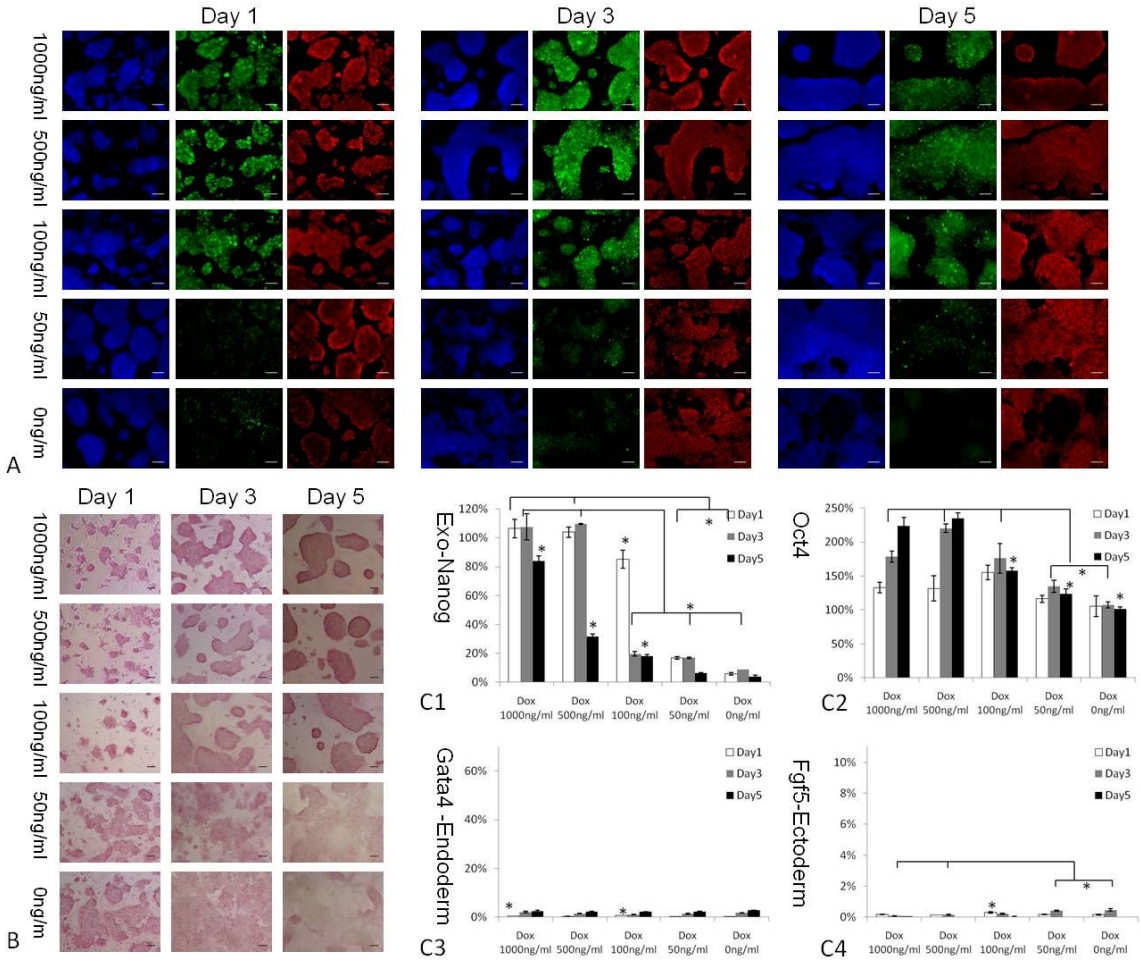

Supplemental Figure 4.2 Titration of Dox concentration in NanogR cells in ESC media containing LIF (A) Immunofluorescent staining of NanogR cells at Day 1,3,5 (blue: DAPI; green: Nanog; red: Oct4). **(B)** AP staining of the NanogR cells at Day 1,3,5. **(C1-C4)** RT-PCR measurement of exogenous Nanog, Oct4, Gata4 and Fgf5 at Day3. *p<0.05. Scale bar: 100μm.

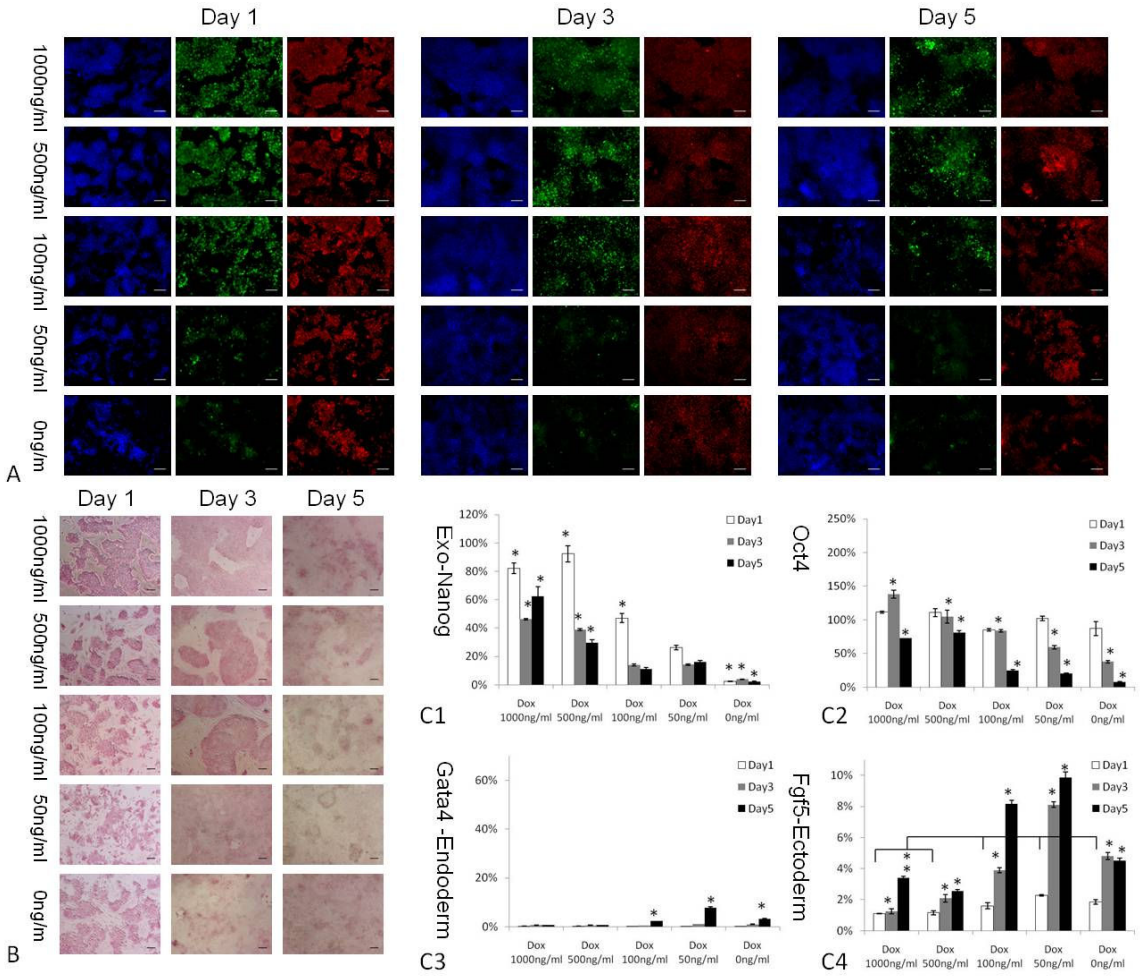

Supplemental Figure 4.3 Titration of Dox concentration in NanogR cells in ESC media containing no LIF (A) Immunofluorescent staining of NanogR cells at Day 1,3,5 (blue: DAPI; green: Nanog; red: Oct4). **(B)** AP staining of the NanogR cells at Day 1,3,5. **(C1-C4)** RT-PCR measurement of exogenous Nanog, Oct4, Gata4 and Fgf5 at Day3. *p<0.05. Scale bar: 100μm.

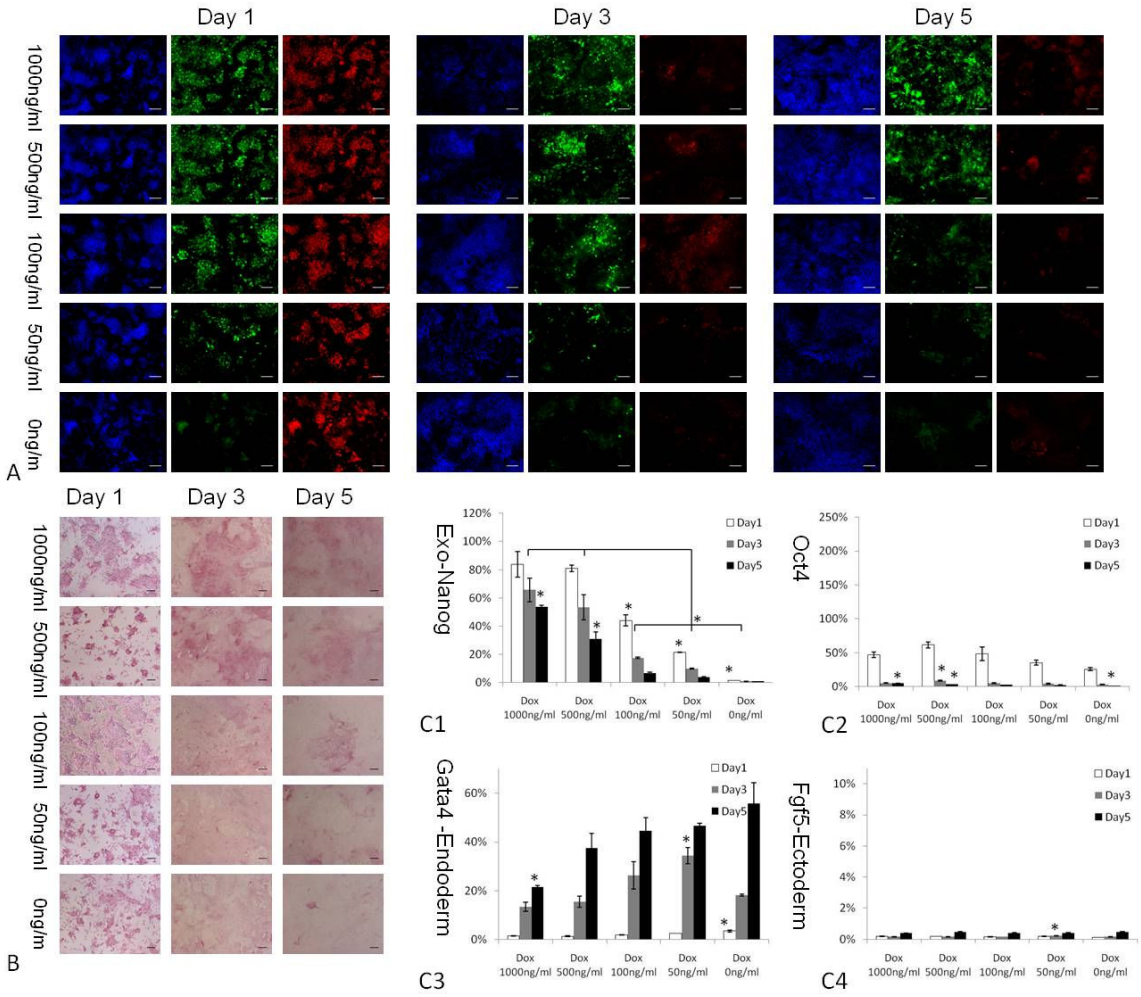

Supplemental Figure 4.4 Titration of Dox concentration in NanogR cells in ESC media containing no LIF but RA (A) Immunofluorescent staining of NanogR cells at Day 1,3,5 (blue: DAPI; green: Nanog; red: Oct4). **(B)** AP staining of the NanogR cells at Day 1,3,5. **(C1-C4)** RT-PCR measurement of exogenous Nanog, Oct4, Gata4 and Fgf5 at Day3. *p<0.05. Scale bar: 100μm.

4.8 References

1. Alexander T, Nolte C, Krumlauf R. Hox genes and segmentation of the hindbrain and axial skeleton. Annu. Rev. Cell Dev. Biol. 25, 431–456, 2009.
2. Atkinson B, Brocklebank MP, Card CCH, Smith, JM. Low Reynolds number developing flows. A.I.Ch.E. Journal, 15(4), 548-553, 1969
3. Burdon T, Stracey C, Chambers I, Nichols J, Smith A. Suppression of SHP-2 and ERK signalling promotes self-renewal of mouse embryonic stem cells. Dev Biol. 210(1):30-43, 1999
4. Chambers I, Colby D, Robertson M, Nichols J, Lee S, Tweedie S, Smith A. Functional expression cloning of Nanog, a pluripotency sustaining factor in embryonic stem cells. Cell 113(5):643-655, 2003
5. Chambers I, Silva J, Colby D, Nichols J, Nijmeijer B, Robertson M, Vrana J, Jones K, Grotewold L, Smith A. Nanog safeguards pluripotency and mediates germline development. Nature. 450(7173):1230-1234, 2007
6. Dahmann C, Oates AC, Brand M. Boundary formation and maintenance in tissue development. Nat Rev Genet. 12(1):43-55, 2011
7. Dormer NH, Berkland CJ, Detamore MS. Previous achievement of patterning at different levels but not at transcription level. Emerging techniques in stratified designs and continuous gradients for tissue engineering of interfaces. Ann Biomed Eng. 38(6):2121-2141, 2010
8. Ivanova N, Dobrin R, Lu R, Kotenko I, Levorse J, DeCoste C, Schafer X, Lun Y, Lemischka IR.Dissecting self-renewal in stem cells with RNA interference. Nature. 442(7102):533-538, 2006
9. Kulesa, PM, Fraser SE. Cell dynamics during somite boundary formation revealed by time-lapse analysis. Science 298, 991–995, 2002
10. Landsberg KP, Farhadifar R, Ranft J, Umetsu D, Widmann TJ, Bittig T, Said A, Jülicher F, Dahmann C. Increased cell bond tension governs cell sorting at the Drosophila anteroposterior compartment boundary. Curr Biol. 19(22):1950-1955, 2009
11. Lu R, Markowetz F, Unwin RD, Leek JT, Airoldi EM, MacArthur BD, Lachmann A, Rozov R, Ma'ayan A, Boyer LA, Troyanskaya OG, Whetton AD, Lemischka IR. Systems-level dynamic analyses of fate change in murine embryonic stem cells. Nature. 462(7271):358-362, 2009
12. Mann RS, Morata G. The developmental and molecular biology of genes that subdivide the body of Drosophila. Annu. Rev. Cell Dev. Biol. 16, 243–271, 2000
13. Meinhardt, H. Cell determination boundaries as organizing regions for secondary embryonic fields. Dev. Biol. 96, 375–385, 1983
14. Mitsui K, Tokuzawa Y, Itoh H, Segawa K, Murakami M, Takahashi K, Maruyama M, Maeda M, Yamanaka S. The homeoprotein Nanog is required for maintenance of pluripotency in mouse epiblast and ES cells. Cell 113(5):631-642, 2003

15. Monier B, Pelissier-Monier A, Brand AH, Sanson B. An actomyosin-based barrier inhibits cell mixing at compartmental boundaries in Drosophila embryos. Nature Cell Biol. 12, 60–65, 2010

16. Nichols J, Zevnik B, Anastassiadis K, Niwa H, Klewe-Nebenius D, Chambers I, Schöler H, Smith A. Formation of pluripotent stem cells in the mammalian embryo depends on the POU transcription factor Oct4. Cell 95(3):379-391, 1998

17. Niwa H, Burdon T, Chambers I, Smith A. Self-renewal of pluripotent embryonic stem cells is mediated via activation of STAT3. Genes Dev. 12(13):2048-2060, 1998

18. Niwa H, Miyazaki J, Smith AG. Quantitative expression of Oct-3/4 defines differentiation, dedifferentiation or self-renewal of ES cells. Nature Genet. 24, 372–376, 2000

19. Sato N, Meijer L, Skaltsounis L, Greengard P, Brivanlou AH. Maintenance of pluripotency in human and mouse embryonic stem cells through activation of Wnt signaling by a pharmacological GSK-3-specific inhibitor. Nature Med. 10, 55–63, 2004

20. Serls AE, Doherty S, Parvatiyar P, Wells JM, Deutsch GH. Different thresholds of fibroblast growth factors pattern the ventral foregut into liver and lung. Development 132(1):35-47, 2005

21. Singh M, Berkland C, Detamore MS. Strategies and applications for incorporating physical and chemical signal gradients in tissue engineering. Tissue Eng Part B Rev. 14(4):341-366, 2008

22. Tremblay KD, Zaret KS. Distinct populations of endoderm cells converge to generate the embryonic liver bud and ventral foregut tissues. Dev. Biol. 280, 87–99, 2005

23. Wang DM, Tarbell JM. Modeling interstitial flow in artery wall allows estimation of wall shear stress on smooth muscle cells, Journal of Biomechanical Engineering 117(3) 358-363, 1995.

24. Wolpert, L. Positional information and the spatial pattern of cellular differentiation. J. Theor. Biol. 25, 1–47, 1969

25. Ying QL, Nichols J, Chambers I, Smith A. BMP induction of Id proteins suppresses differentiation and sustains embryonic stem cell self-renewal in collaboration with STAT3. Cell 115(3):281-292, 2003

26. Zhang Y, Gazit Z, Pelled G, Gazit D, Vunjak-Novakovic G. Patterning osteogenesis by inducible gene expression in microfluidic culture systems. Integr Biol (Camb). 3(1):39-47, 2011

Chapter 5 Summary

In this thesis, we introduced advanced genetic techniques into the tissue engineering and regeneration therapy. *The central question we investigated is about the effect of regulation of gene expression in time and space on cell function.*

In the first project, in order to overcome the limited cell sources for cardiac tissue engineering and regeneration therapy, we developed a novel strategy for controlled expansion of non-proliferating primary neonatal rat cardiomyocytes by reversible immortalization. First, we were able to efficiently transfer immortalization genes: Tag / Bmi-1 / hTERT into cardiomyocytes by lentiviral vector mediated transduction.

Second, we compared two immortalization strategies, TAg / Bmi-1 and hTERT; the TAg gene was more efficient in cell immortalization than the Bmi-1/hTERT gene, able to generate stabilized clones and efficiently expand cells within three weeks of culture, from very limit number of primary cells. After expansion, we were able to completely remove the integrated immortalization gene by Cre-Loxp site recombinase reaction, and completely stop cell proliferation. Lastly, the reverted cell from reversible immortalization, exhibited partially rescued cardiac phenotypes and functions. For the first time, we demonstrated a reversible immortalization strategy that could be applied to primary cardiomyocytes. This

strategy for controlled expansion of primary cardiomyocytes could provide large amounts of the patient's own cardiomyocytes for cell therapy, and enable controlled *in vitro* study of cardiogenesis.

In the future, we expect the convergence of reversible immortalization strategy and induced pluripotent stem (iPS) cell research. The application of reversible gene expression techniques would enable controlled pluripotency induction and reversion by removing the inserted genes. Standard clone selection, expansion and differentiation protocol would be developed across different cell sources. Most importantly, comprehensive epigenetic studies are needed to study how to completely recover specific cell phenotype from this process of reversible genetic modification.

In the second project, we developed a novel strategy for patterning gene expression and thereby patterning the associated cell function, by using inducible gene expression systems and multi-laminar fluidic techniques. Using osteogenic differentiation of mouse mesenchymal stem cells as a model, we demonstrated spatial regulation of the expression of BMP-2 and BMP-2 mediated osteogenesis in a two-dimensional field of cultured cells, by flow patterning the modulator of inducible BMP-2 gene expression vector, Dox. Compared with conventional methods of cell patterning, this strategy combinines inducible gene expression with laminar flow technologies and provides an innovative way to develop multiple tissues / functions from same population of cells, a process that mimic

the developmental process *in vivo.* Therefore*,* the strategy could be used in engineering multi-phase tissue for regeneration therapy, or as a useful platform in studying interface / boundary formation *in vitro*.

Based on the previous project, we were able to explore more sophisticated gene patterning for analysisperturbation in a spatial manner, which can assist the systems biology study of embryonic stem cell fate. In the third project, using Nanog safeguarded embryonic pluripotency as a model; we patterned Nanog gene expression, as well as soluble factors in the laminar fluidic system, thereby successfully developed varied differentiation – pluripotency boundaries between Nanog expressing pluripotency zones and Nanog suppressed early differentiation zones from the same population of cells, up to single colony scale. Based on this platform, system biologists are able to pick specific cells across these Nanog + / Nanog – boundaries, studying the penetration of single genetic perturbation, Nanog, in a spatial manner, which would help us to decipher the potential gene regulation network in spatial control of embryonic development.

We believe that this unique gene patterning strategy can be further advanced in two major directions:

The scientific direction: The combination of the gene patterning strategy with advanced cell patterning technologies, for studying cell interaction at boundaries and the dynamics of signal penetration in a more controlled manner.

The engineering direction: In the thesis, as a 'proof of concept', patterned inducible gene expression was achieved in two-dimensional laminar fluidic systems. We expect patterned inducible gene expression could also be realized in more complicated geometry or even 3 dimensional systems, when combing with varied patterning strategies, such as surface immobilization, spatially controlled release, as well as tissue printing techniques. The application of inducible / reversible genetic engineering combined with those patterning techniques, enables us to unlock the full biological potential to exhibit engineered function in controlled time and space, which holds promise for building fully biological tissues with structural and functional specification.

In summary, we investigated cellular responses to temporal and spatial patterns of gene expression, by combining advanced genetic techniques with microfluidic platforms, towards better regulation of cell differentiation, formation of interfaces and patterning of cell differentiation.

Appendix

Micropatterned Mammalian Cells Exhibit Phenotype-Specific Left-Right Asymmetry

Leo Q. Wan, Kacey Ronaldson, Miri Park, Grace Taylor, Yue Zhang, Jeffrey M. Gimble, Gordana Vunjak-Novakovic

A.1 Abstract

Left-right (LR) asymmetry (handedness, chirality) is a well-conserved biological property of critical importance to normal development. Changes in orientation of the LR axis due to genetic or environmental factors can lead to malformations and disease. While the LR asymmetry of organs and whole organisms has been extensively studied, little is known about the LR asymmetry at a cellular level. Here we show that the cultivation of cell populations on micropatterns with defined boundaries reveals intrinsic cell chirality that can be readily determined by image analysis of cell alignment and directional motion. By patterning 11 different types of cells on several thousands of ring-shaped micropatterns of various sizes, we found that each cell type exhibited definite LR asymmetry (p value down to 10-185) that was different between normal and cancer cells of the same type, and not dependent on surface chemistry, protein coating, or the orientation of the gravitational field. Interestingly, drugs interfering with actin but not microtubule function reversed the LR asymmetry in some cell types. Our

results show that micropatterned cell populations exhibit phenotype-specific LR asymmetry that is dependent on the functionality of the actin cytoskeleton. We propose that micropatterning could potentially be used as an effective in vitro tool to study the initiation of LR asymmetry in cell populations, to diagnose disease and to study factors involved with birth defects in laterality.

A.2 Introduction

Left-right (LR) asymmetry is seen in the development of numerous living organisms, including climbing plants (1), helices of snail shells (2), and the human body (3, 4). Genetic diseases and prenatal exposure to teratogens can cause birth defects in laterality (5, 6). The LR asymmetry has been studied in animal embryos, which are difficult to control and are not necessarily representative of human condition (7, 8). Recent studies focused on directional nodal flow driven by primary cilia (9-11), pH gradients resulting from asymmetric expression of ion channels (12, 13), and asymmetric vesicular transport via myosin 1D along actin cable networks (14-16).

The initiation of LR asymmetry in development is often first observed in populations of cells of the same type, such as snail embryonic cells at 4-cell and 8-cell stages and mouse cells at embryonic nodes. The establishment of LR asymmetry or chirality within such cell clusters may rely on some intracellular structure, such as the hypothetical F-molecule or actin/microtubule cytoskeleton (17, 18) that can distinguish left from right by orienting the 3rd axis with respect

to predetermined dorsal-ventral and anterior-posterior axes. In addition, during development, the specification and self-organization of migrating cells are mediated by physical boundaries imposed by the extracellular matrix and the surrounding cells and tissues. We, therefore, hypothesized that the populations of cells of the same type, if cultured within patterns with well-defined boundaries, would express directional alignment and motion associated with the establishment of LR asymmetry.

We find that the cells form an invariant chiral alignment, depending on the cell phenotype and actin function. We infer that all cells are intrinsically chiral and that the function of actin may play a significant role in switching the intrinsic chirality of cells and their LR asymmetry in developmental biology. Due to its simplicity, our 2D microscale system provides an effective method to study the LR symmetry of tissue development in vitro and may provide a useful tool for identifying biological and environmental factors involved in bilateral birth defects.

A.3 Result and Discussion

Cells exhibit distinct left-right asymmetry on micropatterned geometries

We first cultured the C2C12 murine myoblasts on micropatterns with well-defined boundaries, such as circles, squares, linear strips, and rings (**Figure A.S1**) (19, 20). Biased cell alignment was observed on linear strips and rings but not on circles and squares (**Figure A.S2 a-f**), suggesting the importance of appositional boundaries for the expression of chirality. Because equivalent bias in cell

alignment was observed on linear strips and rings of different sizes (**Figure A.S2 g**), rings with an inner diameter of 250 μm and a distance of 200 μm between the inner and outer boundary were used in subsequent studies.

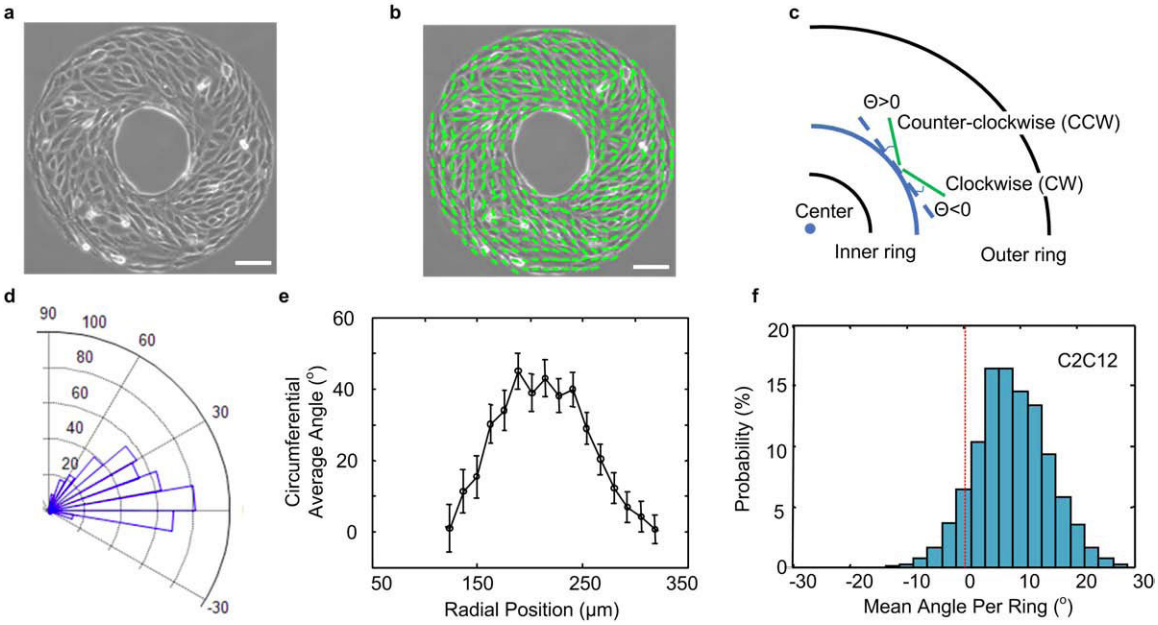

Figure A.1. Mouse myoblasts (C2C12) show distinct left-right asymmetry on micropatterned surfaces. Scale bars: 100 μm. **(a)** Asymmetric cell alignment on ring patterns (phase contrast image). (**b**) Cell alignment directions (green lines). (**c)** Thebiased angle of cell alignment (green lines) was defined as either CW or CCW, based on the deviation from the circumferential direction (blue dash line). (**d**) The circular histogram of biased angles shows CCW chirality. (**e**) Circumferential averages of the sub-regional biased angles at different radial positions on the ring (mean ± SEM). (**f**) The histogram of the mean biased angles of C2C12 cells (33 experiments, >1000 ring patterns).

Phase contrast images, in which cell contour appears brighter than the inner cell region, were used to measure cell alignment (21) (**Figure A.1a**), as indicated by green lines in Figure 1b. Each green line was assigned a biased angle between -90o and 90o, based on its deviation from the circumferential direction (blue dash line); a positive value represented a counter clockwise (CCW) alignment, while a

negative value represented a clockwise (CW) alignment (**Figure A.1c**). An angular histogram (Figure 1d) and the radial distribution (Figure 1e) of the measured angles revealed preference for positive angles, corresponding to the CCW bias. In >30 independent series of experiments using >1000 individual rings (**Table A.S2, Figure A.1f**), the C2C12 cells showed CCW alignment with a biased angle of 8.47o } 0.20o (mean ± SEM), with very strong statistical significance ($p = 9.3 \times 10^{-186}$).

Cell chirality on patterned surfaces depends on cell phenotype

We then tested a panel of mouse, rat, and human cells derived from skeletal muscle, bone, adipose tissue, skin, heart, and blood vessels (**Table A.S1**). Cell phenotypes included myoblasts, osteoblasts, endothelial cells, fibroblasts, and mesenchymal stromal/stem cells. Interestingly, mouse (C2C12) and human skeletal muscle cells (hSkMCs) showed a CCW alignment, while all other cell types exhibited a CW alignment (**Figure A.2**). Cancer skin cells also exhibited a CCW alignment, different from the CCW alignment of skin fibroblasts from the same individual. These data suggest that adherent mammalian cells exhibit an invariant chirality determined by the cell phenotype and disease condition.

Left-right asymmetry on micropatterns is established by mechanisms involving cellular directional migration on boundaries

a

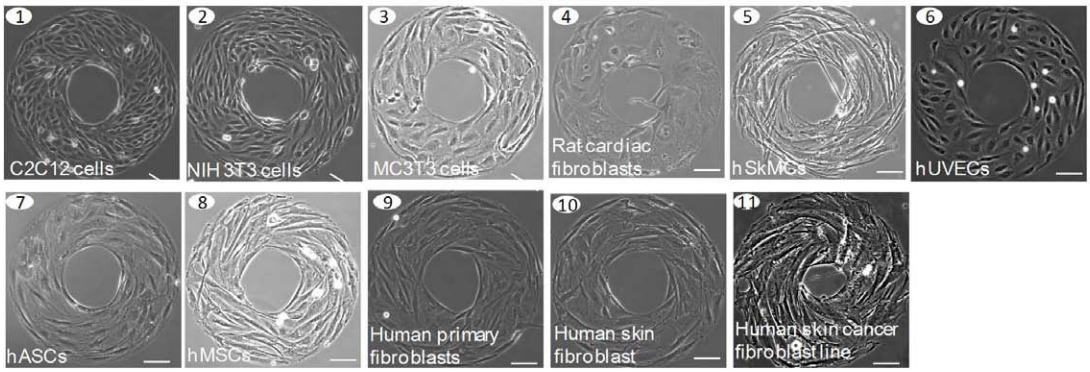

b

Cell Chiraltiy vs Cell Phenotype

No.	Cell Description	Num of Exps	CW	N/S	CCW	p Value	Catalog Number	Species	Tissue	Phenotype	Cell Culture
1	C2C12	33	34	172	850	$9.3X10^{-186}$	ATCC CRL-1772	mouse	skeletal muscle	myoblast	cell line
2	NIH/3T3	4	51	20	8	$4.5X10^{-9}$	ATCC CRL-1658	mouse	embryo	fibroblast	cell line
3	MC3T3-E1	3	65	70	19	$2.4X10^{-7}$	ATCC CRL-2593	mouse	calvaria	osteoblast	cell line
4	rat cardiac fibroblast	7	100	66	17	$8.6X10^{-16}$	—	rat	heart	cardiac fibroblast	primary cells
5	hSkMC	5	16	67	80	$1.0X10^{-11}$	Lonza CC-2661	human	skeletal muscle	myoblast	cell line
6	hUVEC	11	307	65	16	$5.0X10^{-61}$	—	human	umbilical vein	endothelial cells	primary cells
7	hASC	3	44	21	3	$1.2X10^{-10}$	—	human	adipose	stem cells	primary cells
8	hMSC	2	42	7	7	$1.5X10^{-7}$	—	human	bone marrow	stem cells	primary cells
9	human primary skin fibroblast	6	172	24	2	$6.1X10^{-42}$	ATCC PCS-201-012	human	skin	fibroblast	primary cells
10	human skin fibroblast line	4	49	31	19	$1.8X10^{-4}$	ATCC CRL-7761	human	skin	fibroblast	cell line
11	human skin cancer fibroblast line	3	32	49	58	0.004	ATCC CRL-7762	human	skin	fibroblast	cell line

Figure A.2. Cell chirality on patterned substrates depends on cell phenotype and disease condition. (a) Phase contrast images of various cell types. (b) Cell source andtheir chirality on micropatterned surfaces. Here, "-" indicates that cells were isolated in the lab; CW: clockwise alignment; CCW: counter-clockwise alignment; N/S: not significantly biased to CW or CCW. The C2C12 cells and human skeletal muscle cells exhibit a counter-clockwise alignment while other cells that were studied show aclockwise alignment. The human skin cancer fibroblast cell line show a counterclockwise alignment, opposite from healthy human skin fibroblasts. Scale bars: 100 μm.

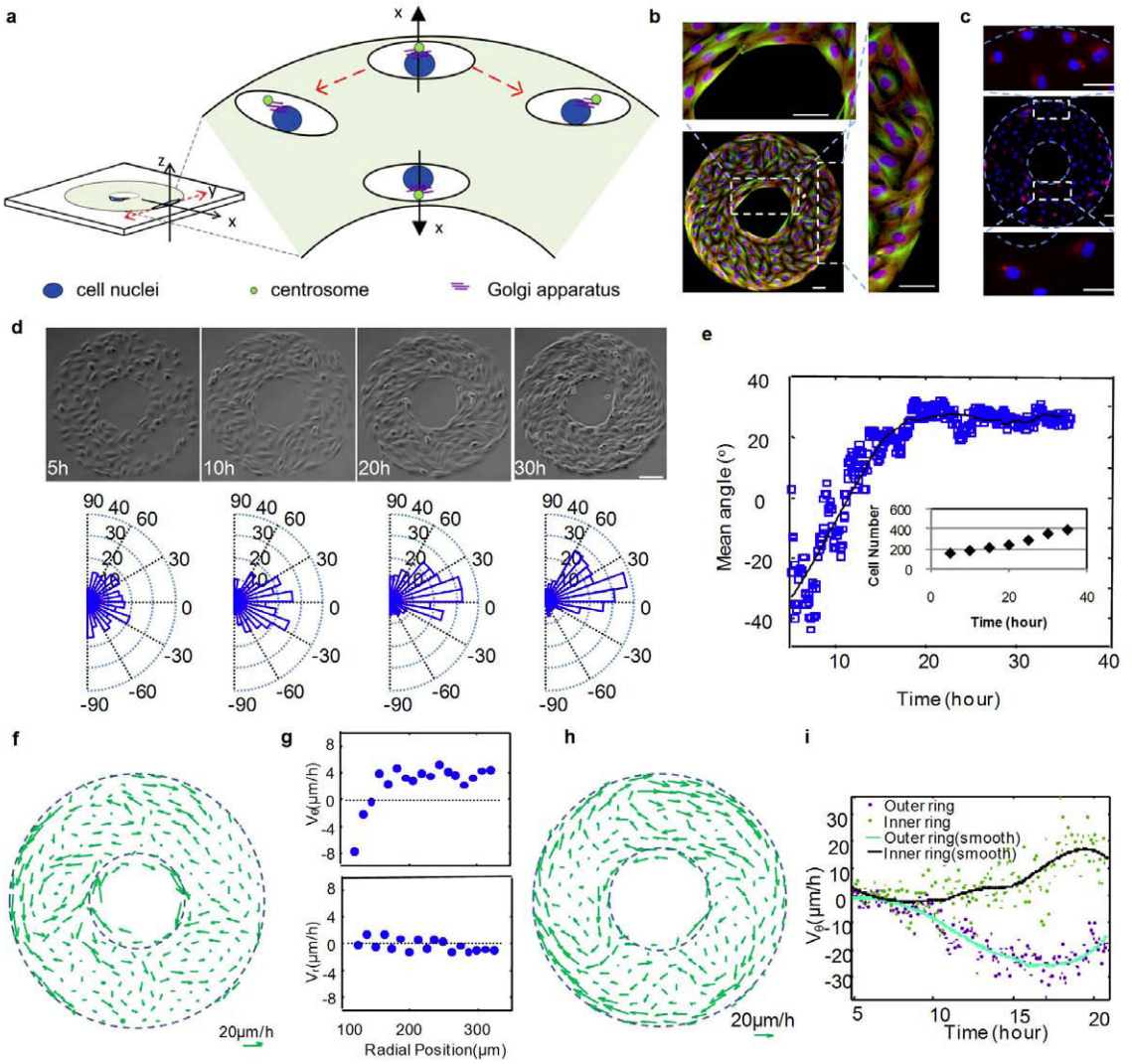

Figure A.3. **Cellular Left-right asymmetry on micropatterned rings is established by mechanisms involving boundary effects**. (**a**) Cells on a ring "sense" the z-axis throughattachment to the substrate and the x axis through the ring boundaries. The cell alignment bias of the y-axis (dash red lines) creates the observed cellular chiral behavior or LR asymmetry. (**b**) Centrosomes (bright green) are positioned closer to each boundary than nuclei (blue) in C2C12 cells (actin: red, tubulin: green). Scale bars: 50 μm. (**c**) Golgi apparatus (red) is positioned closer to ring boundaries than nuclei (blue) in hUVEC cells. Scale bars: 50 μm. (**d**) Phase contrast images of the cells (top) at 5, 10, 20, and 30 hours after cell seeding and the corresponding histograms (bottom) of biased angles from the sub-regions for each image. Scale bars: 100 μm. (**e**) The time history of the mean biased angle of C2C12 cells on a ring, with the insert for cell number increasing exponentially with time. (**f**) Average velocity and direction of C2C12 cells are indicated by arrowdirection and length, respectively. (**g)** Average velocity of C2C12 cell migration in the circumferential (Vθ) and the radial direction (Vr) as a function of radial position. (**h**) Average velocity and (**i**) the circumferential migration velocity of hUVEC cells at the inner and outer ring boundary as a function of time.

For cells on a patterned geometry to display their chirality and to distinguish between left and right (y-axis), the polarity of the z-axis (up-down) and x-axis (front-back) must be established (**Figure A.3a**). Notably, the z-axis was established independent of gravity direction, as observed experimentally in vertically inverted cell cultures (**Table A.S4**). The geometric boundaries determined organelle positioning (i.e., x-axis), with centrosomes (bright green, **Figure A.3b**) and Golgi apparatus (red, **Figure A.3c**) being positioned closer to the boundaries than the cell nucleus (blue) (22), independent of the gravitational direction. In addition, cell chirality was maintained on patterns with different surface chemistry (23), and after the disruption of cadherin function (**Figure A.S1, Table A.S5-6**).

For further insight into the biased cell alignment, we analyzed C2C12 cell motion (Video S1-2, not shown here). Cell alignment did not show a clear bias before confluency (**Figure A.3d-e**), suggesting that the inhibition of random walk through physical contact was necessary for the cells to exhibit chirality. The cells were labeled and tracked along the inner and outer ring pattern (Video S3, not shown here), and the cell migration velocity was estimated by digital image correlation (24). The speed of migration was higher at the inner and outer ring boundaries (~ 25 μm/hr in average) than within the interior region (~10 μm/hr). The average velocity (**Figure A.3f**) and the velocity changes in radial and circumferential directions (**Figure A.3g**) demonstrated that the cells migrated in

the CW direction at the inner ring boundary (at 8μm/hr), and in the CCW direction at the outer ring boundary (at 4 μm/hr).

At the level of an individual cell, this seemingly opposite circular motion of cells on the inner and outer boundary is in fact consistent with biased migration. Based on cell polarization at boundaries, the x-axis can be defined as the direction from the nucleus to centrosome (25), as shown in **Figure A.3a**. Cell migration can thus be considered as 'leftward bias' along both the inner and outer ring boundary. Also, cell alignment on micropatterns is related to the cell migration at the boundaries, as seen for a C2C12 cell migrating towards a boundary and adopting the leftward biased migration. Because cell polarization and biased migration occur at the boundaries of micropatterns, cell proximity to a boundary is necessary for the expression of chirality. This finding was further supported by the biased cell alignment being most clearly seen in the regions close to the boundaries, especially for less elongated cells such as cardiac fibroblasts (**Figure A.2a**).

The mean biased angle of human umbilical cord endothelial cells (hUVEC) on rings was similar in magnitude to that of C2C12 cells, but was negative (-8.47o } 0.33o, n=388), indicating a CW alignment (**Table A.S3**). By the time the cell chirality was established (15-20 hours after seeding, Video S4-6), cells along the boundaries had a significantly higher migration speed (35 μm/hr) than those in the interior regions (20 μm/hr). In contrast to C2C12 cells, hUVEC migration was

in the CCW direction at the inner ring boundary (15μm/hr) and in the CW direction at the outer ring boundary (20 μm/hr) (**Figure A.2h-i**). Based on the x-axis directed from the nucleus to the centrosome/Golgi apparatus, the migration of hUVECs exhibited a 'rightward' bias.

Chirality of muscle cells requires functional actin but not tubulin

To investigate the roles of actin and tubulin, cyoskeletal proteins putatively linked to cell chirality (1, 2, 14, 16, 25), we inhibited the dynamics of their polymerization and depolymerization (**Figure A.4a-b**). For C2C12 and hUVEC cells, cell alignment on micropatterned rings followed a dose-dependent response (**Table A.S7**). Low concentrations of the actin treadmilling inhibitors (Latrunculin A, cytochalsin D, Jasplakinolide) reversed the chirality of C2C12 cells from CCW into CW. In contrast, inhibitors of tubulin dynamics (Nocodazole, Taxol) at concentrations below those resulting in cell apoptosis did not change cell chirality. Similar results were obtained for human skeletal muscle cells. The CCW bias of the cells depended on the function of actin but not non-muscle myosin II (**Figure A.S3**). In contrast to C2C12 cells, the drugs tested could not reverse the chirality of hUVEC cells or rat cardiac fibroblasts. Collectively, these data suggest that functional actin is required for cells exhibiting the CCW but not CW bias.

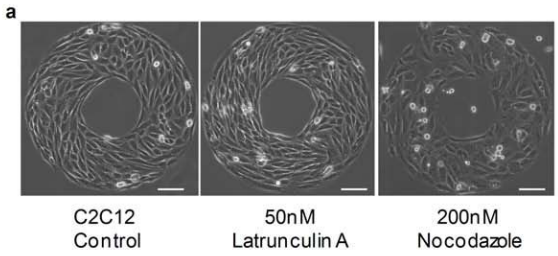

b

C2C12 Drug	Num of Exps	CW	N/S	CCW	p Value
Control	2	0	0	73	$1.1X10^{-22}$
Lat A	2	61	15	2	$2.2X10^{-16}$
Cyto D	3	15	34	1	$2.6X10^{-4}$
Jasp	2	25	13	0	$3.0X10^{-8}$
Noc	2	0	18	57	$6.9X10^{-18}$
Taxol	2	4	17	48	$6.0X10^{-11}$

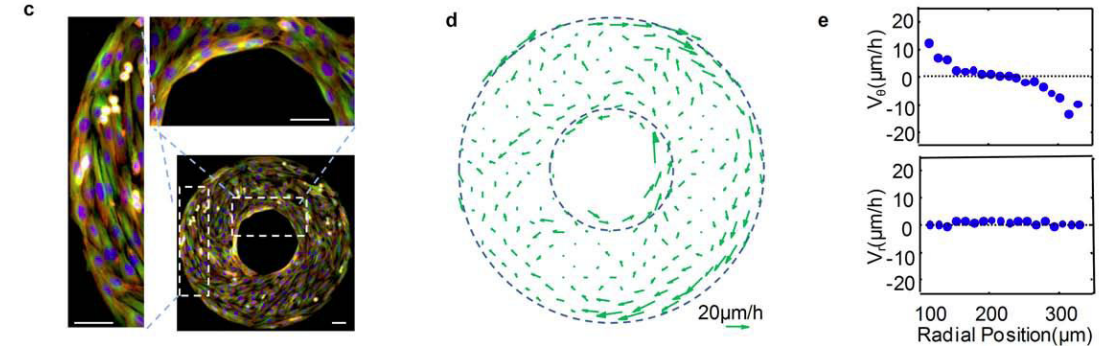

Figure A.4. **Chirality of muscle cells requires functional actin but not tubulin**. (**a**) Phase contrast images and (**b**) chirality of C2C12 cells on micro-patterned rings in the presence of Latrunculin A, Cytochalasin D, Jasplakinolide, Nocodazole, and Taxol. Scalebars: 100 μm. (**c**) Latrunculin A does not change the polarity of C2C12 cells, as the cells positioned their centrosome (bright green), rather than the nucleus (blue), closer to ring boundaries. Scale bars: 50 μm. (**d**) Migration of C2C12 cells in the presence of Latrunculin A, with the direction and magnitude of velocity indicated by arrow direction and length, respectively. (**e**) Average velocity of the cells along the circumferential direction (Vθ) and the radial direction (Vr) as a function of radial position.

Interestingly, C2C12 cells treated with Latrunculin A polarized in the same fashion as the untreated cells (**Figure A.4c**), as evidenced by organelle positioning relative to boundaries, suggesting that the drug did not alter cell polarization. Analysis of cell migration (Video S7-8, not shown here) showed reversal at the boundaries (**Figure A.4d-e**), with the cells migrating CW along the outer ring and CCW along the inner ring at 15 μm/hr. Thus, inhibition of actin function reversed the CCW chirality and the biased migration of C2C12 cells.

It is possible that two competing mechanisms co-exist within cells to determine their LR decisions or chirality. One mechanism would require actin function and

lead to the intrinsic ‘leftward’ bias at the boundaries and subsequent CCW alignment in chiral morphogenesis. The second mechanism would induce intrinsic ‘rightward’ bias at the boundaries and a CW alignment in chiral morphogenesis. The differences in chirality may be due to the higher expression of actin in muscle cells than other cells (26, 27), necessitating identification of cell-type-related determinants of chirality in tissue development. Interestingly, actin bundles were reported to account for cardiac looping, the first visible sign of LR asymmetry in vertebrate embryos (28, 29). While the exact mechanism detailing how actin affects cell chirality is still unknown, our drug treatment data show that the mammalian muscle cells share similarities in their chirality with invertebrate cells such as those in snail embryos (2). Further studies are necessary to evaluate the role of actin expression levels in the establishment and reversal of cell chirality, possibly mediated through the non-canonical Wnt signaling pathway which plays a critical role in pattern determination during embryonic development (30).

In summary, cells cultured on micropatterns with well-defined appositional boundaries exhibit chiral morphogenesis that can be readily determined by analysis of cell alignment and directional motion. In studies of 11 different cell types that were countered on several thousand patterns, we observed that the cell chirality was defined by the cell phenotype, and that the loss of actin but not microtubule function could reverse the CCW cell chirality. The simple and highly accurate in vitro platform developed in these studies could potentially be used to

study the initiation of chiral morphogenesis and identify genetic, biochemical and environmental factors leading to malformations.

A.4 Methods

Microcontact Printing

Cell patterning was done by using olydimethylsiloxane (PDMS) elastomeric stamps and self-assembly monolayers (SAMs) (19, 20, 23). A master mold was first fabricated with SU-8 2050 photoresist (MicroChem Corp, Newton, MA) and chromium masks with desired geometric features. The mixture (10:1) of PDMS pre-polymer and curing agent (Dow Corning, Midland, MI) was poured into the mold and cured at 70°C for 4 hours.

In most studies (and unless indicated otherwise), an adhesive SAM octadecanethiol (Sigma) was transferred onto the gold-coated (150 Å in thickness) glass slide with the PDMS stamp (**Figure A.S1**) (19). The slide was then immersed in a non-adhesive ethylene glycol-terminated SAM (HS-(CH2)11-EG3, Prochimia, Poland) for 3 hours. Finally, patterned surfaces were washed with ethanol and coated with 10 µg/ml fibronectin (Sigma) for 30 minutes.

Alternatively (**Figure A. S1**), the PDMS stamp was coated with 50 µg/ml fibronectin for 30 minutes, aspirated, and dried in the air for 1 minute (23). The stamp was then gently placed onto tissue culture-treated dishes for 2 minutes, and incubated in a non-adhesion SAM, 100 µg/ml poly-L-lysine-polyethylene

glycol (PLL-g-PEG; Susos AG, Dübendorf, Switzerland), for 1 hour. Finally the surface was washed with phosphate buffered saline (PBS).

Cell Culture

Cells were maintained in tissue flasks with culture media specified in **Table A.S1**. After reaching 70% confluency, cells were trypsinized and seeded onto protein-coated patterned surfaces. Once the cells attached, extra cells were washed off with fresh medium. At this time drugs were added into the culture medium if necessary. Phase contrast images were taken after overnight incubation at 37oC and 5% CO2 when cells reached confluency on the ring patterns.

Drug Treatment

To examine the role of actin in left-right (LR) asymmetry, cells were tested with 20 - 500 nM Latrunculin A, 0.05 - 1.0 µg/ml Cytochalasin D, and 1 - 100 nM Jasplakinolide. Latrunculin A inhibits actin polymerization by forming a 1:1 molar complex with G-actin, thereby inhibiting its ability to polymerize into F-actin (31). Cytochalasin D inhibits actin polymerization by binding to the growing ends of F-actin chains and thus preventing the attachment and addition of G-actin monomers (32). Jasplakinolide is known to bind to and stabilize actin filaments in vitro (33).

To examine the role of microtubules in LR asymmetry, 0.2- 2 µM Nocodazole, and 0.3 -30 nM Taxol were used. Nocodazole suppresses microtubule dynamics

by destabilizing and disassembling microtubules (32). Taxol inhibits the microtubule depolymerization and stabilizes microtubules (34).

To examine the role of the actomyosin motor, cells were tested with 0.2 - 10 mM Y-27632, 1 - 20 mM ML-7, and 0.5 - 10 mM Blebbistatin. Y-27632 works as a selective inhibitor to prevent the phosphorylation of the myosin regulatory light chain (35). ML-7 acts as a selective inhibitor of the myosin light chain kinase (36). Blebbistatin forms a low actin affinity complex through binding to myosin heads, causing the inhibition of nonmuscle myosin II ATPase activity (37).

Immunofluorescence Staining

After imaging, cells were fixed with 4% formaldehyde in cytoskeletal buffer (10 mM MES, 138 mM KCl, 3 mM MgCl2, 2 mM EGTA, and 0.32 M sucrose) for 25 minutes. For actin / tubulin double staining, the cells were incubated with phalloidin-TRITC (1:400; Invitrogen) and anti-Tubulin-FITC (1:50; Sigma) for 1 hour. For the Golgi apparatus positioning inside patterned rings, the cells were incubated in 1μg/ml anti-human golgin-97 (Invitrogen) for 1 hour. After secondary antibodies, cell nuclei were stained with 200 ng/ml 40, 6-diamidino-2-phenylindole (DAPI; Sigma) for 10 minutes. Finally, the cells were mounted with Fluoromount-G medium (SouthernBiotech, Birmingham, AL).

Analysis of Cell Alignment

High-resolution phase contrast images of live patterned cells were taken at a resolution of ~0.645 μm /pixel, and analyzed using a custom-written code in MatLab (MathWorks, Natick, MA), based on the automated detection of intensity gradient and circular statistics (21). In this algorithm, the intensity gradient was determined pixel by pixel with a Gaussian differential filter. In each sub-region of the image, the dominant local direction was determined using an accumulator scheme, in which the orientation of each pixel follows a von Mises distribution, a circular analogue of the linear normal distribution. Subsequently, the orientation in each sub-region was converted into an angle bias based on its deviation from the circumferential direction (see **Figure A.1c**). Mean angle and standard deviation of LR asymmetry were calculated for all sub-regions, using circular statistics (38). We verified that the variation of sub-region size from 10 by 10 pixels to 60 by 60 pixels would not significantly alter the judgment of cell chirality on rings. The sub-region size was therefore set to 20 by 20 pixels (*i.e.*, 13 by 13 μm).

Analysis of Cell Migration

For time-lapse videos, cells were patterned on a gold-coated glass-bottom Petri dish (ibid, München, Germany). After cells attached, the dish was transferred into an environmental chamber (37oC and 5% CO2) and image time series were recorded every 5 minutes at a resolution of 1.56 μm/pixel for a total time of 20-40 hours. As the image capture rate is much higher than the characteristic time for cell migration, digital image correlation, together with sub-pixel displacement

estimation, were used to determine the displacements of cell migration. A FFT (fast Fourier transform)- based method was first utilized to match regions of two sequential phase contrast images. The calculated displacement values were then used as inputs for a more accurate estimation of displacement fields at a sub-pixel level, using a second-order image correlation algorithm described previously (24). To evaluate the bias of cell migration, the obtained velocity field was further projected in the circumferential (Vθ) and radial (Vr) direction.

Statistical Analysis.

Cell chirality on ring patterns (*i.e.*, clockwise or counterclockwise alignment) was determined from calculated biased angles in local regions with one sample test for the mean angle, analogous to the one sample t-test in linear statistics (38). The overall biased behavior of the cells was tested based on the number of rings exhibiting either clockwise or counter clockwise alignment in the rank test, with confidence level set to 0.05.

A.5 Supplemental Information

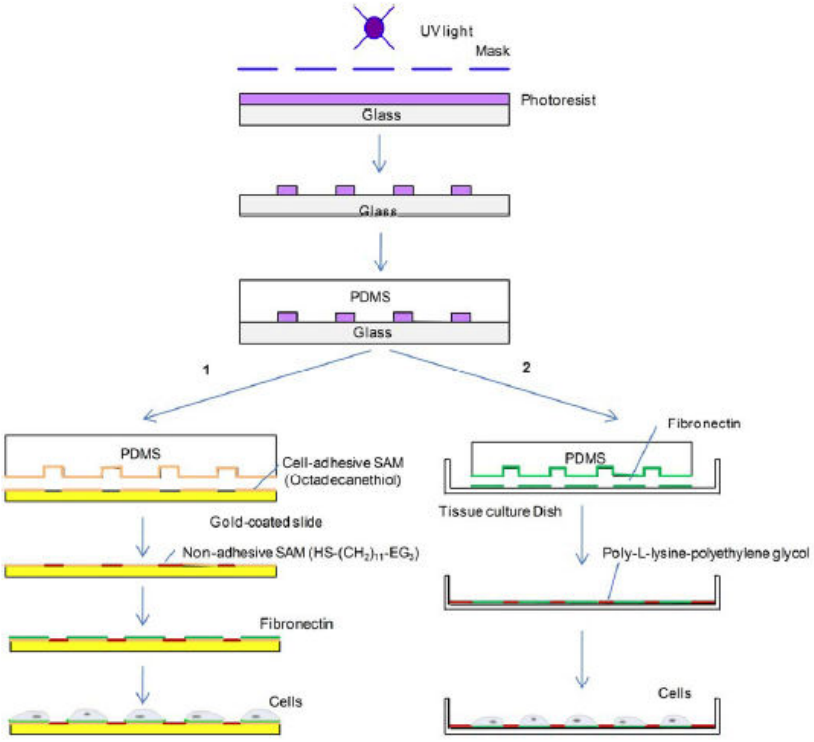

Figure A.S1. Micro-fabrication and micro-contact printing for cell patterning. A negative photoresist mold was made first by UV (ultraviolet) crosslinking through a mask containing desired micropatterning features. PDMS (polydimethylsiloxane) elastomeric stamps were then casted with prepolymers onto the mold. In most experiments (**path 1**), octadecanethiol, an adhesive self-assembly monolayer (SAM), was transferred via the PDMS stamp onto goldcoated glass slides, which were then sequentially subjected to a non-adhesive ethylene glycolterminated SAM HS-(CH2)11-EG3 and fibronectin. Alternatively (path 2), fibronectin was stamped onto tissue culture treated plastic, which was subsequently backfilled with poly-Llysine-polyethylene glycol and washed with PBS for cell seeding.

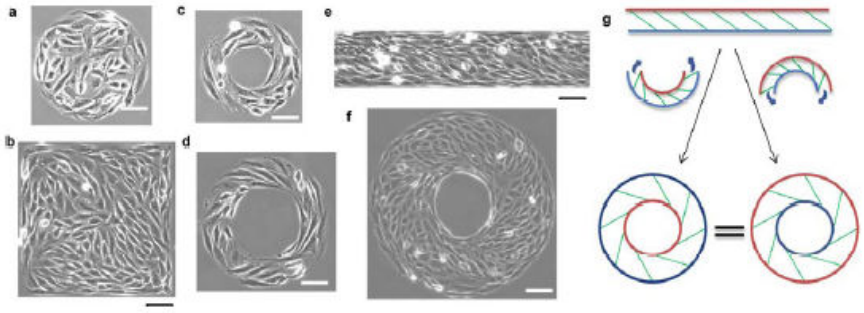

Figure A. S2. C2C12 cells grown on micro-patterned surfaces. (**a-f**) Cells on strip and ring geometries clearly demonstrate asymmetric alignment, while those residing on the circular and square patterns do not. (**g**) A schematic of the conformity in the biased cell alignment between cells on strips and cells on rings. Green lines indicate the direction of cell alignment, while blue and red lines represent the opposite boundaries of strips or rings. Ring geometry shows a consistent biased alignment regardless of whether the linear strip was bent upward or downward to create ring geometry, suggesting that the left-right asymmetry is independent of the ring curvature. Scale bars: 100 μm.

a

b

C2C12 Drug	Num of Exps	CW	N/S	CCW	p Value
Control	2	0	0	73	$1.1X10^{-22}$
Blebb	2	0	11	17	$7.6X10^{-6}$
ML-7	2	0	4	19	$1.9X10^{-6}$
Y-27632	3	0	7	22	$2.4X10^{-7}$

Figure A. S3. Effects of drugs blocking the actomyosin motor. Phase contrast images (a) and chirality data (b) of C2C12 cells under the treatment of drugs that affect the function of actomyosin motor. These drugs (Blebbistatin, ML-7, and Y-27632) did not affect left-right asymmetry. Scale bars: 100 μm.

Cell Type	Base Medium Source	Composition
C2C12	Invitrogen Cat# 21068	DMEM with 10% FBS, 1% P/S, 1mM sodium pyruvate
hUVEC	Lonza Cat# CC-3156 Cat# CC-4176	Endothelial Basal Medium-2 (EBM-2) supplemented with EGM-2 SingleQuot Kit supplement & growth factors
NIH/3T3	Invitrogen Cat# 21068	DMEM with 10% FBS, 1% P/S, 1mM sodium pyruvate
hASC	Invitrogen Cat# 21068	DMEM with 10% FBS, 1% P/S, 1mM sodium pyruvate
hMSC	Invitrogen Cat# 21068	DMEM with 10% FBS, 1% P/S, 1mM sodium pyruvate
hSkMC	Lonza Cat# CC-3161 Cat# CC-3160	SkMC Basal Media supplemented with SkMC SingleQuot Kit supplement & growth factors
MC-3T3	Invitrogen Cat# 12561	Minimum essential α Medium with 10% fetal bovine serum, 1% penicillin/streptomycin
Human primary skin fibroblast	Invitrogen Cat# 21068	DMEM with 10% FBS, 1% P/S, 1mM sodium pyruvate
Human skin fibroblast line	Invitrogen Cat# 21068	DMEM with 10% FBS, 1% P/S, 1mM sodium pyruvate
Rat cardiac fibroblast	Invitrogen Cat# 21068	DMEM with 10% FBS, 1% P/S, 1mM sodium pyruvate penicillin/streptomycin, 1mM sodium pyruvate

Table A. S1 Compositions of cell culture media. DMEM: Dulbecco's Modified Eagle Medium; P/S: penicillin/streptomycin; and FBS: fetal bovine serum; C2C12: mouse skeletal muscle C2C12 cell line; hUVEC: human umbilical vein endothelial cells; NIH/3T3: mouse embryonic fibroblast cell line; hASC: human adipose-derived stem cells; hMSC: human bone marrow-derived mesenchymal stem cells; hSkMC: human skeletal muscle cell line; MC-3T3: mouse osteoblast cell line.

C2C12	CW	N/S	CCW	Biased?	p Value
1	0	1	21	Y	$4.8X10^{-7}$
2	0	2	37	Y	$7.3X10^{-12}$
3	2	7	29	Y	$2.3X10^{-7}$
4	0	4	18	Y	$3.8X10^{-6}$
5	0	1	25	Y	$3.0X10^{-8}$
6	0	1	28	Y	$3.7X10^{-9}$
7	0	3	19	Y	$1.9X10^{-6}$
8	0	2	25	Y	$3.0X10^{-8}$
9	0	0	28	Y	$3.7X10^{-9}$
10	0	0	45	Y	$2.8X10^{-14}$
11	0	2	27	Y	$7.5X10^{-9}$
12	0	4	31	Y	$4.7X10^{-10}$
13	6	29	29	Y	$5.8X10^{-5}$
14	4	27	8	N	0.19
15	3	7	21	Y	$1.4X10^{-4}$
16	0	2	10	Y	$9.8X10^{-4}$
17	0	0	21	Y	$4.8X10^{-7}$
18	0	6	29	Y	$1.9X10^{-9}$
19	3	4	19	Y	$4.3X10^{-4}$
20	0	7	7	Y	$7.8X10^{-3}$
21	2	7	37	Y	$1.4X10^{-9}$
22	4	8	11	Y	0.04
23	1	4	27	Y	$1.0X10^{-7}$
24	1	6	35	Y	$5.2X10^{-10}$
25	0	3	28	Y	$3.7X10^{-9}$
26	1	3	28	Y	$5.4X10^{-8}$
27	0	4	36	Y	$1.5X10^{-11}$
28	1	5	42	Y	$4.9X10^{-12}$
29	2	7	21	Y	$3.0X10^{-5}$
30	1	6	27	Y	$1.0X10^{-7}$
31	3	8	36	Y	$1.7X10^{-8}$
32	0	1	21	Y	$4.7X10^{-7}$
33	0	1	24	Y	$6.0X10^{-8}$
Sum	34	172	850	Y	$1.6X10^{-254}$

Tables A.S2 The chirality of mouse myoblast cell line C2C12 on ring patterns. CW: clockwise alignment, CCW: counter-clockwise alignment, and N/S: not significantly biased to CW or CCW.

hUVEC	CW	N/S	CCW	Biased?	p Value
1	17	0	0	Y	$7.6X10^{-6}$
3	13	7	4	Y	0.018
4	22	2	1	Y	$2.7X10^{-6}$
5	31	6	1	Y	$7.5X10^{-9}$
6	10	1	0	Y	$9.8X10^{-4}$
7	25	14	2	Y	$2.6X10^{-6}$
8	15	4	1	Y	$2.4X10^{-4}$
9	35	8	2	Y	$4.8X10^{-9}$
10	26	6	1	Y	$2.0X10^{-7}$
11	26	4	0	Y	$1.5X10^{-8}$
12	24	4	1	Y	$7.5X10^{-7}$
13	34	7	1	Y	$1.0X10^{-9}$
14	29	2	2	Y	$2.2X10^{-7}$
Sum	307	65	16	Y	$2.7X10^{-71}$

Table A.S3 The chirality of human umbilical vein endothelial cells, hUVECs on ring patterns. CW: clockwise alignment, CCW: counter-clockwise alignment, and N/S: not significantly biased to CW or CCW.

Culture	CW	N/S	CCW	p Value
Normal	2	7	21	$3.3X10^{-5}$
Inverted	1	7	26	$2.1X10^{-7}$

Substrate Protein	CW	N/S	CCW	p Value
Fibronectin	1	4	32	$2.0X10^{-9}$
Collagen I	0	0	23	$1.2X10^{-7}$
Laminin	2	2	34	$9.2X10^{-9}$
Matrigel	0	5	35	$2.9X10^{-11}$

Culture	CW	N/S	CCW	p Value
Control	1	3	28	$5.6X10^{-8}$
0.5mM EGTA	0	2	24	$3.0X10^{-8}$
2mM EGTA	1	3	12	$1.7X10^{-3}$
Ca^{2+} free medium	1	3	26	$2.1X10^{-7}$

Table A.S4-6. Effects of culture conditions on cell chirality. S4 (top): The cells retained their chirality under inverted culture (upside down) as compared to that at normal condition, suggesting that there is no effect of gravity. **S5** (middle)**:** Cell chirality did not alter with protein coating with fibronectin, Type I collagen, laminin and Matrigel. **S6** (bottom)**:** Cell chirality was also conserved at reduced cell-cell interactions under low calcium conditions (either following the addition of a calcium chelator, EGTA, or in calcium-free culture medium).

Cell type	Drug	Concentration	CW	N/S	CCW	p Value
C2C12	Latrunculin A	0 nM	0	0	73	$1.1X10^{-22}$
		50 nM	61	15	2	$2.1X10^{-16}$
		200 nM	57	7	0	$6.9X10^{-18}$
		500 nM	1	10	0	0.5
	Cytochalasin D	0 µg/mL	1	6	35	$5.2X10^{-10}$
		0.05 µg/mL	9	6	8	0.19
		0.1 µg/mL	7	10	3	0.12
		0.2 µg/mL	21	23	5	$9.8X10^{-4}$
		0.5 µg/mL	10	14	0	$9.8X10^{-4}$
		1 µg/mL	8	20	1	0.018
	Jasplakinolide	0 nM	1	6	27	$1.0X10^{-7}$
		1 nM	2	10	34	$9.2X10^{-9}$
		3 nM	3	4	18	$6.3X10^{-4}$
		10 nM	7	5	14	0.055
		30 nM	18	4	0	$3.8X10^{-6}$
		100 nM	7	9	0	$7.8X10^{-3}$
	Nocodazole	0 nM	0	0	73	$1.1X10^{-22}$
		200 nM	0	18	57	$6.9X10^{-18}$
		500 nM	0	58	35	$2.9X10^{-11}$
		1 µM	0	21	18	$3.8X10^{-6}$
		2 µM	0	6	1	0.5
	Taxol	0 nM	3	8	36	$1.7X10^{-8}$
		0.3 nM	1	3	24	$7.5X10^{-7}$
		1 nM	1	6	20	$1.0X10^{-5}$
		3 nM	2	9	31	$6.1X10^{-8}$
		10 nM	2	8	17	$3.3X10^{-4}$
		30 nM	2	13	16	$5.8X10^{-4}$
hUVEC	Latrunculin A	0 nM	38	21	6	$4.0X10^{-7}$
		20 nM	36	8	0	$1.4X10^{-11}$
		50 nM	2	19	0	0.25
		200 nM	2	56	5	0.16
		500 nM	2	42	1	0.38
	Cytochalasin D	0	26	6	1	$2.0X10^{-7}$
		0.1 µg/mL	8	12	0	$3.9X10^{-3}$
		0.2 µg/mL	10	22	0	$9.8X10^{-4}$
		0.5 µg/mL	0	6	1	0.5
	Jasplakinolide	0 nM	34	7	1	$1.0X10^{-9}$
		1 nM	32	1	1	$3.8X10^{-9}$
		3 nM	22	5	2	$1.6X10^{-5}$
		10 nM	22	10	5	$6.0X10^{-4}$
		30 nM	5	4	0	0.031
		100 nM	1	5	0	0.5
	Nocodazole	0 nM	38	21	6	$4.0X10^{-7}$
		200 nM	25	76	3	$1.2X10^{-5}$
		500 nM	14	27	2	$1.8X10^{-3}$
		1 µm	3	4	0	0.125
		2 µm	1	7	0	0.5
	Taxol	0 nM	29	2	2	$2.2X10^{-7}$
		0.3 nM	8	0	0	$3.9X10^{-3}$
		1 nM	34	4	1	$1.0X10^{-9}$
		3 nM	7	9	2	0.07
		10 nM	10	11	5	0.09
		30 nM	4	7	2	0.23

Table A.S7. Effects of actin and tubulin blockers. Dose-dependent changes in the left-right asymmetry of cells on patterned surfaces to various drugs that interfere with the actin and microtubule function.

A.6 References

1. Edwards W, Moles AT, & Franks P. The global trend in plant twining direction. *Global Ecol Biogeogr* 16(6):795-800, 2007
2. Shibazaki Y, Shimizu M, & Kuroda R. Body handedness is directed by genetically determined cytoskeletal dynamics in the early embryo. *Curr Biol* 14(16):1462-1467, 2004
3. Afzelius BA. A human syndrome caused by immotile cilia. *Science* 193(4250):317-319, 1976
4. Li R & Bowerman B. Symmetry breaking in biology. *Cold Spring HarbPerspect Biol* 2(3):a003475, 2010
5. Mercola M & Levin M. Left-right asymmetry determination in vertebrates. *Annu Rev Cell Dev Biol* 17:779-805, 2001
6. Aylsworth AS. Clinical aspects of defects in the determination of laterality. *Am J Med Genet* 101(4):345-355, 2001
7. Levin M. Left-right asymmetry in embryonic development: a comprehensive review. *Mech Dev* 122(1):3-25, 2005
8. Speder P, Petzoldt A, Suzanne M, & Noselli S. Strategies to establish left/right asymmetry in vertebrates and invertebrates. *Curr Opin Genet Dev* 17(4):351-358, 2007
9. Okada Y, Takeda S, Tanaka Y, Belmonte JC, & Hirokawa N. Mechanism of nodal flow: a conserved symmetry breaking event in left-right axis determination. *Cell* 121(4):633-644, 2005
10. Hirokawa N, Tanaka Y, Okada Y, & Takeda S. Nodal flow and the generation of left-right asymmetry. *Cell* 125(1):33-45, 2006
11. Tabin CJ. The key to left-right asymmetry. *Cell* 127(1):27-32, 2006
12. Levin M, Thorlin T, Robinson KR, Nogi T, & Mercola M. Asymmetries in H+/K+-ATPase and cell membrane potentials comprise a very early step in leftright patterning. *Cell* 111(1):77-89, 2002
13. Adams DS*, et al.* Early, H+-V-ATPase-dependent proton flux is necessary for consistent left-right patterning of non-mammalian vertebrates. *Development 1*33(9):1657-1671, 2005
14. Spéder P, Adám G, & Noselli S. Type ID unconventional myosin controls left-right asymmetry in Drosophila. *Nature* 440(7085):803-807, 2006
15. Spéder P & Noselli S. Left-right asymmetry: class I myosins show the direction. *Curr Opin Cell Biol* 19(1):82-87, 2007
16. Hozumi S*, et al.* An unconventional myosin in Drosophila reverses the default handedness in visceral organs. *Nature* 440(7085):798-802, 2006
17. Brown NA & Wolpert L. The development of handedness in left/right asymmetry. *Development* 109(1):1-9, 1990
18. Levin M & Mercola M. The compulsion of chirality: toward an understanding of left-right asymmetry. *Genes Dev* 12(6):763-769, 1998

19. Wan LQ*, et al.* Geometric control of human stem cell morphology and differentiation. *Integr Biol (Camb)* 2(7-8):346-353, 2010

20. Chen CS, Mrksich M, Huang S, Whitesides GM, & Ingber DE. Geometric control of cell life and death. *Science* 276(5317):1425-1428, 1997

21. Karlon WJ*, et al.* Measurement of orientation and distribution of cellular alignment and cytoskeletal organization. *Ann Biomed Eng* 27(6):712-720, 1999

22. Desai RA, Gao L, Raghavan S, Liu WF, & Chen CS. Cell polarity triggered by cell-cell adhesion via E-cadherin. *J Cell Sci* 122(Pt 7):905-911, 2009

23. Thery M & Piel M. Adhesive micropatterns for cells: a microcontact printing protocol. *Cold Spring Harb Protoc* 2009(7):pdb prot5255, 2009

24. Zhou P & Goodson KE. Subpixel displacement and deformation gradient measurement using digital image/speckle correlation (DISC). *Opt Eng*40(8):1613-1620, 2001

25. Xu J*, et al.* Polarity reveals intrinsic cell chirality. *Proc Natl Acad Sci USA* 104(22):9296-9300, 2007

26. Shimizu N & Obinata T. Actin concentration and monomer-polymer ratio in developing chicken skeletal muscle. *J Biochem* 99(3):751-759, 1986

27. Herman IM. Actin isoforms. *Curr Opin Cell Biol* 5(1):48-55, 1993

28. Taber LA. Biophysical mechanisms of cardiac looping. *Int J Dev Biol* 50(2-3):323-332, 2006

29. Itasaki N, Nakamura H, Sumida H, & Yasuda M. Actin bundles on the right side in the caudal part of the heart tube play a role in dextro-looping in the embryonic chick heart. *Anat Embryol (Berl)* 183(1):29-39, 1991

30. Pohl C & Bao Z. Chiral forces organize left-right patterning in C. elegans by uncoupling midline and anteroposterior axis. *Dev Cell* 19(3):402-412, 2010

31. Coue M, Brenner SL, Spector I, & Korn ED. Inhibition of actin polymerization by latrunculin A. *FEBS Lett* 213(2):316-318, 1987

32. Cooper JA. Effects of cytochalasin and phalloidin on actin. *J Cell Biol* 105(4):1473-1478, 1987

33. Bubb MR, Spector I, Beyer BB, & Fosen KM. Effects of jasplakinolide on the kinetics of actin polymerization. An explanation for certain in vivo observations. *J Biol Chem* 275(7):5163-5170, 2000

34. Derry WB, Wilson L, & Jordan MA. Substoichiometric binding of taxol suppresses microtubule dynamics. *Biochemistry* 34(7):2203-2211, 1995

35. Ishizaki T*, et al.* Pharmacological properties of Y-27632, a specific inhibitor of rho-associated kinases. *Mol Pharmacol* 57(5):976-983, 2000

36. Isemura M, Mita T, Satoh K, Narumi K, & Motomiya M. Myosin light chain kinase inhibitors ML-7 and ML-9 inhibit mouse lung carcinoma cell attachment to the fibronectin substratum. *Cell Biol Int Rep* 15(10):965-972, 1991

37. Kovacs M, Toth J, Hetenyi C, Malnasi-Csizmadia A, & Sellers JR. Mechanism of blebbistatin inhibition of myosin II. *J Biol Chem* 279(34):35557-35563, 2004

38. Fish NI. *Statistical Analysis of Circular Data* (Cambridge University Press, Cambridge, UK), 1993